Max-Planck-Institut für Intelligente Systeme
(ehemals Max-Planck-Institut für Metallforschung)
Stuttgart

Mechanisms of intrinsic stress formation in thin film systems

David Flötotto

Dissertation
an der
Universität Stuttgart

Bericht Nr. 246
Dezember 2013

Mechanisms of intrinsic stress formation in thin film systems

Von der Fakultät Chemie der Universität Stuttgart
zur Erlangung der Würde eines Doktors der Naturwissenschaften (Dr. rer. nat.)
genehmigte Abhandlung

vorgelegt von
David Flötotto
aus Münster

Hauptberichter:	Prof. Dr. Ir. E. J. Mittemeijer
Mitberichter:	Prof. Dr. S. Schmauder
Prüfungsvorsitzender:	Prof. Dr. T. Schleid

Tag der Einreichung:	11.10. 2013
Tag der Mündlichen Prüfung:	16.12. 2013

MAX-PLANCK-INSTITUT FÜR INTELLIGENTE SYSTEME
(ehemals MAX-PLANCK-INSTITUT FÜR METALLFORSCHUNG)
INSTITUT FÜR MATERIALWISSENSCHAFT DER UNIVERSITÄT STUTTGART

Stuttgart 2013

Contents

Chapter 1

General introduction

1.1 Thin film systems

Thin film systems are nowadays widely applied in advanced technologies such as microelectronics, optoelectronics, catalysis and functional surface coatings for enhanced corrosion and wear resistance. For example, thin films are essential components of data storage units in computers, lasers for ultrafast communication and micro-mechanical systems in sensors and actuators. The enormous spectrum of applications of thin films has largely relied on substantial progress in the preparation of thin films with atomic precision and the fundamental understanding of the fascinating properties of thin film, which largely differ from those of bulk materials. For instance, the capability of growing ultrathin metal heterostructures with layer thicknesses < 3 nm lead to the discovery of the giant magnetic resistance effect which is now utilized in high-density hard drivers [1-3].

During fabrication and processing of thin film systems, both *intrinsic* (i.e. arising during film growth) and *extrinsic* (i.e. induced after film growth; e.g. due to differences in thermal shrinkage/expansion of the various system components upon cooling/heating) residual stresses may arise. The thus induced residual stresses can strongly influence the mechanical reliability and the functional properties of thin-film systems. On the one hand, the residual film stresses can deteriorate the system's mechanical stability during operation, by causing excessive deformation, leading to fracture and/or spallation. Furthermore, electrons and phonons are often scattered at stress-induced defects, thereby reducing the performance of electronic and optical devices (e.g. solar cells and lasers). On the other hand, the mechanical, optical, electronic and magnetic properties of thin film systems may also benefit from the controlled adjustment of the film stresses [2,4,5].

To date the technological potential to optimize and control the properties of thin film systems by tailoring their microstructure *and* their stress state is still limited owing to the lack of fundamental and comprehensive understanding of the stress generating mechanisms and their complex correlation with the microstructure development during thin film growth.

1.2 Focus of the thesis

This thesis addresses the underlying mechanisms of intrinsic stress generation during thin film growth and in particular their correlation with the developing microstructure and atomic scale processes during thin film growth, such as adsorption, diffusion and reactions. To this end, the intrinsic stress evolutions and microstructural developments during the growth of metal, semiconductor and oxide thin films have been studied by a combinatorial experimental approach using real-time in-situ substrate curvature measurements, a broad range of surface analytical techniques, high-resolution transmission electron microscopy and X-ray diffraction. The studies reveal the decisive role of the surface and grain-boundary diffusivity of adatoms on microstructure formation and intrinsic stress evolution during polycrystalline film growth (Chapter 2), as well as the effect of the surface structure on absorption induced surface stress changes (Chapter 4). Furthermore, during heteroepitaxial growth of an ultrathin metal film on a semiconductor substrate, a hitherto unrecognised stress generating mechanism resulting from the quantum confinement of free electrons in the ultrathin metal films has been discovered (Chapter 3). Finally, for the first time, it is demonstrated that the growth of ultrathin oxide films on their metal surfaces by thermal oxidation at low temperatures can give rise to the generation of significant growth stresses, even if the formed oxide films exhibit amorphous microstructures (Chapter 5).

1.3 Thin-film growth

1.3.1 Thermodynamic and kinetic aspects of microstructural development

The microstructural evolution during thin film growth (comprising the development of the morphology, thickness, chemical constitution, grain size, grain shape, texture and the defect structure) is governed by atomic scale processes, such as adsorption, surface diffusion, nucleation and growth. Some general trends for various material classes and fabrication techniques can be identified by application of simplified (but fundamental) thermodynamic and kinetic criteria (while disregarding more complex and material specific phenomena). Clearly, such thermodynamic and kinetic criteria for thin film growth processes, as discussed in the following, will evidently largely depend on the growth conditions, such as the substrate temperature, the deposition rate, the partial gas pressures, impurity concentrations and the state of the parent substrate surface (e.g. roughness and surface orientation) [6-8].

During thin film growth generally three different types of growth modes can be thermodynamically distinguished by considering the various energy contributions to the total Gibbs energy of the thin film/substrate system, i.e. the surface energies of the film, γ_f, and the bare substrate, γ_s, as well as the interface energy, γ_i, of the interface between the substrate and the film. If $\gamma_s < \gamma_f + \gamma_i$, Volmer-Weber type of growth occurs, as characterized by the nucleation of individual islands on the substrate, which grow laterally until they impinge and coalesce. If $\gamma_s \geq \gamma_f + \gamma_i$, Frank-Van der Merwe type of growth occurs, as characterized by a maintained, two dimensional progression of the film surface during thickening of the film. If $\gamma_f + \gamma_i < \gamma_s < \gamma_f + \gamma_i + \gamma_{elastic}$, Stranski-Krastanov type of growth occurs, i.e. initial layer by layer growth proceeds until the elastic deformation energy, $\gamma_{elastic}$, arising from the lattice mismatch accommodation exceeds at a certain thickness a critical value and subsequent island growth becomes favoured instead [9,10]. Furthermore, the attempt of a thin film to minimize its surface and interface energies can lead to the development of textures (i.e. preferred crystallographic orientations of the constituting grains in the polycrystalline film) or, in extreme cases, to epitaxial film growth where a certain crystallographic relationship exist between the film and its substrate. Noteworthy, the formation of amorphous instead of crystalline films can also be thermodynamically preferred [10,11].

Obviously, thin film growth is a highly non-equilibrium process and the establishment of equilibrium is always limited by the atomic mobility of the involved species. As a result, coarsening of islands, grain growth and the development of textures can be hindered by a low atomic mobility, whereas kinetic roughening and the formation of defects like twins, stacking faults and pores may occur. As a result, various structure-zone models have been established (see Fig. 1.1) to describe the microstructural evolution as function of growth parameters (in particular, of the substrate temperature) which control the atomic mobility.

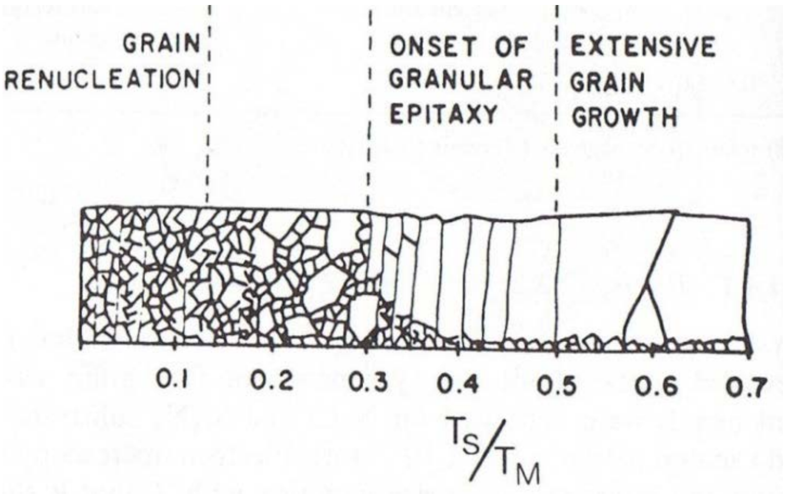

Fig. 1.1. Schematic grain structure evolution during polycrystalline film growth during thermal evaporation as function of the homologous temperature [12].

1.3.2 Physical vapor deposition

Physical vapor deposition (PVD) is one of the most common techniques for the fabrication of thin films. In the PVD process, a target solid gets evaporated from a crucible or sputtered by ion bombardment onto a substrate to form a thin film at its surface. In particular, thermal evaporation of material from an effusion cell under ultra-high vacuum conditions (base pressure < 10^{-7} Pa) has attracted enormous interest, since it enables the routine production of high-purity amorphous, polycrystalline and (epitaxial) single-crystalline metal and semiconductor thin films with a very precise control of the deposition rate. The deposition rate (typically several nm's per minute) is determined by the vapor pressure of the deposited material, the distance between the effusion cell and the substrate as well as the sticking coefficients of the atoms on the substrate and the developing film surfaces. Compared to other deposition techniques, such as magnetron sputtering, only modest deposition rates can be achieved by thermal evaporation and the kinetic energy of the evaporated atoms arriving at the substrate is relatively low (50-100 meV) [10,13].

1.3.3 Oxidation

Apart from thin film growth by deposition of material on a substrate, thin films can also be formed by chemical reactions and phase transformations at surfaces. One example is the growth of ultrathin oxide films on metal surfaces by the reaction with oxygen gas, designated as thermal oxidation.

The formation of a closed oxide film on bare metal surface upon thermal oxidation involves a series of concurrent and overlapping steps such as physisorption of oxygen molecules, (dissociative) chemisorption, oxide nucleation and growth. When the thus formed oxide layer covers the entire metal surface, further oxide growth (thickening) can only proceed, if the charged reactive species are transported through the developing oxide layer [14-17]. At relatively low temperatures (<450°C), where thermal activated diffusion is absent, oxide film growth proceeds by the migration of the reactants under the influence of an electric surface charge field [15,18], and the formation of amorphous instead of crystalline oxide films can be thermodynamically preferred [19]. The oxidation of Al surfaces at room temperature can be considered as a model system for such oxide film formation at low temperatures. The initial interaction of oxygen with the bare Al surface [20-24], as well as the subsequent stages of oxide nucleation and film growth [25-27], have been extensively investigated both experimentally and theoretically. It was revealed that the growth kinetics strongly depend on the temperature, the oxygen partial pressure and the substrate orientation. The resulting Al_2O_3 oxide films are initially amorphous [19], although local short range ordering exists due to the formation of a network of neighboring building blocks of edge- and corner sharing [AlO_4] and [AlO_6] polyhedra (i.e. Al cations in tetrahedral or octahedral interstices of the distorted, densely packed oxygen sublattice) [28].

1.4 Intrinsic stress generation in thin films

Up to date, the intrinsic stress evolution during thin film growth has been extensively studied for a huge diversity of materials, deposition techniques and deposition conditions. In particular, real-time in-situ stress measurements in combination with microstructural characterazing and surface-analytical techniques were applied to deduce the operating intrinsic stress generating mechanisms. It was found that the stress evolution upon film growth are intrinsically governed by (*i*) the developing film (micro)structure, (*ii*) the surface morphology of the developing film, (*iii*) surface stress and interface stress effects, as well as (*iv*) dynamic processes during growth, such as the diffusion of adatoms and reacting species.

1.4.1 Atomic Structure

It is well accepted that during epitaxial film growth a considerable strain/stress can build up in the thickening film due to the lattice mismatch between the substrate and the film. The magnitude of the associated growth stress is determined by the difference in the equilibrium lattice spacings of the film and the rigid substrate [29]. Since for a given mismatch the strain energy in the film increases with increasing thickness, injection of misfit dislocations into the growing film becomes energetically favorable beyond a critical thickness and hence, the stress relaxes [30-33].

Reduction of free volume during thin film growth i.e. densification, due to grain growth or phase transformations is associated with the development of tensile stress [34].

1.4.2 Surface and interface stress

The occurrence of surface stress and interface stress is a direct consequence of the different chemical and structural environments of the atoms at the surface or the interface as compared to the bulk and the resulting modification of the bonding configurations at the surface or interface region (with respect to the bulk). The surface/interface stress can be defined as the reversible work per unit area associated with straining a surface or an interface elastically [35]. Evidently surface stress plays a dominant role in many surface-related phenomena, such as surface reconstructions [36], surface diffusion and morphological transitions [37]. Adsorption of foreign species on a solid surface and the generation of surface defects modify the local chemical environment at the surface, which typically results in a change of the surface stress [36,38-41].

Surface and interface stresses have a large impact on the development of intrinsic stresses during thin films growth. The instantaneous action of surface stress results in the generation of compressive stresses during the deposition of amorphous films [42,43], as well as for the initial stages of island nucleation and film growth (see Sec. 1.4.3) [44]. Noticeably, at the very onset of film growth, surface and interface stresses can even reverse the sign of the equilibrium coherency stress as expected from the misfit between the lattice constants of the film and the substrate [45,46].

1.4.3 Morphological evolution

It has long been recognized that specific film morphology evolutions during thin film growth (see Sec. 1.3.1) can be assigned to certain stress generating mechanism. For instance, the formation and growth of islands at a substrate surface at the initial stage of Volmer-Weber type of growth is associated with the development of a compressive stress component due to the action of the Laplace pressure in combination with the strength of adhesion of the islands to the substrate [44,47]. Subsequent formation of grain boundaries upon coalescence of adjacent islands then results in the generation of tensile stress components due to interatomic forces acting across the developing grain boundaries. The magnitude of this tensile stress component depends on the grain-boundary energy and the density of formed grain boundaries [48-52]. Furthermore, morphology transitions such as island formation on a wetting layer (i.e. Stransiki-Krastanov type of growth) or roughening of a initially smooth film provide the possibility for significant relaxation of stress [53,54].

1.4.4 Dynamic, non-equilibrium processes

By definition thin film growth is a non-equilibrium process and consequently a high density of excess surface defects (i.e. vacancies, adatoms, and ledges) exists during thin film growth, which can not only result in a change of surface stress of the growing film, but can also induce stress components in the bulk of the film [55-57]. For example, the supersaturation of the surface by the steady flux of deposited adatom species and the therewith associated increased chemical potential at the film surface can drive the transport of adatoms from the surface into grain boundaries, and thus results in the buildup of a compressive stress component [58-62]. Similarly, also chemical reactions or phase transitions can promote the transport of (ad)atoms during thin film growth, which can result in complex intrinsic stress gradients due to changes in the local film density (e.g. reaction-induced changes in molar volumes, generation/annihilation of vacancies and/or molar volume differences of interdiffusing species) [63-65].

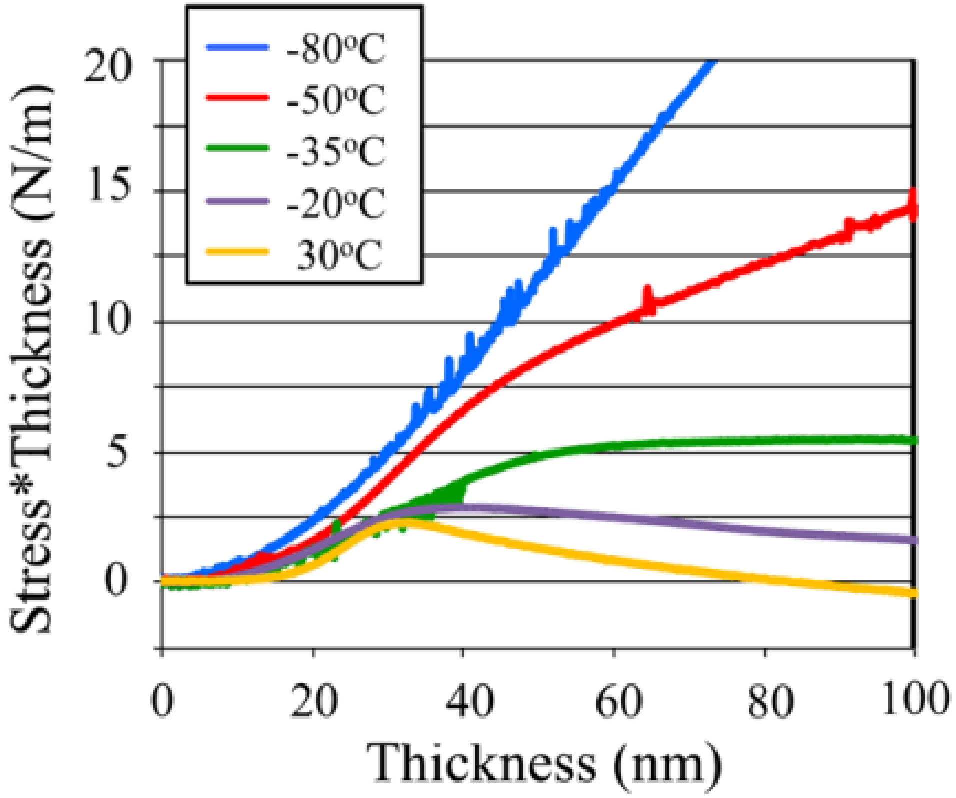

Fig. 1.2. Representative stress evolutions during growth of polycrystalline Ag film as function of film thickness at substrate temperatures between -80°C and 30°C. With increasing substrate temperature the compressive stress generating mechanism(s), due to adatom incorporation into grain boundaries, superpose the tensile stress component due to the coalescence of adjacent grains [59].

Generally, during thin film growth several of the aforementioned stress generating mechanisms may operate at the same time and the extent of the particular mechanisms depend on the growth conditions and material parameters, such as the growth rate [55,59,66], substrate temperature [67,68], (residual) gas pressure [69,70], surface/interface energy [71], surface and interface stress [43], atomic diffusivity [67], state of stress [72], bonding character/topology and developing microstructure [73]. Therefore, experimentally observed stress evolutions are often the result of a superposition of different mechanisms, although a single mechanism might be dominant at a certain stage of film growth. For example, during polycrystalline Ag film growth impinging islands or grains result in the continuous generation of a tensile stress component, but at the same time the diffusion of adatoms into the just formed grain boundaries lead to the generation of a compressive stress component. The effective film stress is then given by the growth-condition dependent extend of the particular mechanisms (see Fig. 1.2).

1.5 Methods of investigation

An experimental setup for thin film preparation under controlled conditions in combination with in-situ non-destructive analytical techniques is a prerequisite to investigate the stress evolution during thin film formation and to disclose the operating stress generating mechanisms. In the present thesis, a combined experimental approach by real-time in-situ multi optical stress sensor (MOSS), in-situ scanning tunnelling microscopy (STM), real-time in-situ spectroscopic ellipsometry (RISE), in situ angle-resolved X-ray photoelectron spectroscopy (AR-XPS), ex-situ X-ray diffraction (XRD) and ex-situ high resolution transmission electron microscopy (HR-TEM) has been applied to study the stress evolution and microstructure development during thin film growth.

1.5.1 Multi optical stress sensor (MOSS)

The multi optical stress sensor is a substrate curvature-based technique, which allows real time in-situ stress measurement during thin film growth. The working principle of such technique is based on the optical measurement of the curvature change of a thin substrate resulting from a non-zero bending moment distribution as induced by the development of an in-plane force per unit width in the growing film [2].

The experimental setup used in the present thesis is shown in Figure 1.3. A laser beam is split by two etalons into a two dimensional (3x3) grid of parallel beams which is leveled to the specimen. The laser beams are reflected by the substrate and captured by a CCD camera. Since any bending of the specimen results in a change of spacing between the laser beams, ΔD, at the CCD camera, such measurement thus provides a direct measure of the change of substrate curvature $\Delta\kappa$ as function of time. According to the Stoney equation [74], the measured change in substrate curvature is proportional to the change in the film force (or force per unit width), $\Delta\tau$, which is given by the product of thickness average in-plane stress, $\langle\sigma\rangle$, and the film thickness, h_f, plus the change in surface stress, f, and interface stress, g:

$$\Delta\kappa = \frac{6}{M_s {h_s}^2}\Delta\tau = \frac{6}{M_s {h_s}^2}\Delta(\langle\sigma\rangle h_f + f + g) \tag{1.1}$$

where the thickness averaged film stress is given by $1/h_f \int_0^{h_f} \sigma(z)dz$ and M_s and h_s denote the biaxial modulus and thickness of the substrate, respectively [2,75,76].

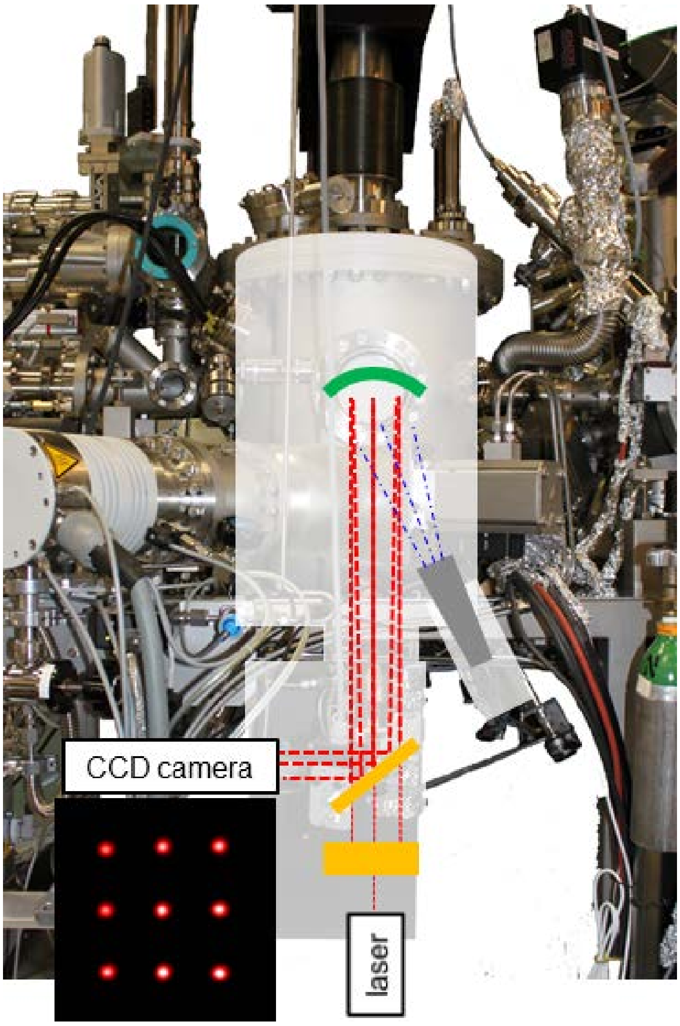

Fig. 1.3. Schematic sketch of the multi optical stress sensor as used in the present thesis. A 3x3 grid of laser beams is leveled on to a thin substrate which reflects the laser beams into a CCD camera. Any change of substrate curvature results in a change of spacing between the laser beams at the CCD camera.

The above equation is exactly applicable only if: (*i*) the film is much thinner than the substrate, (*ii*) the film is an equibiaxial state of stress in the plane of the film (*iii*) both the film and the substrate materials are homogeneous and isotropic, (*iv*) specimen edge effects are negligible and (*v*) strains and rotations are infinitesimal.

However, various models and extended formula exist which relax these assumptions (see [2,77-79] and references therein).

The great advantage of the curvature-based stress measurement method as compared to other techniques e.g. XRD is that it not only allows in-situ stress measurements in real time, but it is also applicable to both crystalline and amorphous films. Furthermore, since vibrations of the specimen only lead to common translations of all reflected laser spots in the same direction, the relative distance between the beams does not change and hence, the method is extremely robust to any external noise and changes in substrate curvature (i.e. curvatures as small as 0.2 km^{-1} can typically be resolved).

1.5.2 Scanning tunneling microscopy (STM)

The development of STM by Binning, Rohrer and coworkers in 1981 has revolutionized surface science, since STM not only provides three dimensional real-space images of surfaces at high spatial resolution, but also allows to map the local electronic structure of material surfaces at the atomic scale [80-82].

The working principle of STM relies on the quantum mechanical tunneling of electrons through the energy barrier separating the sharp metal tip and the sample surface. If the tip and the sample surface are close enough that their electron wave functions overlap and if a bias voltage eV_t is applied between the tip and the sample, electrons from occupied states within eV_t above the Fermi level on the negative side can tunnel into empty states within eV_t below the Fermi level on the positive side. The resulting tunnel current I_t depends exponentially on the tip-to-sample distance d (e.g. a 1 Å decrease of d will increase I_t by one order of magnitude) and therefore enables a precise control over the vertical tip position, resulting in the unique subatomic height resolution of STM [80,81].

In order to produce topographic images of the specimen surface, the tip is scanned in the lateral dimension over the specimen by piezoelectric devices, while the tip-to-specimen distance is continuously regulated by a piezoelectric tube through a feedback circuit to keep the tunnel current constant. In this so-called “constant current” mode the generated image is given by the voltage signal of the piezoelectric tube and represents contours of constant charge density near the Fermi level of the specimen surface [81]. Therefore, STM images recorded over large areas can be safely interpreted as representing the surface topography. However, care must be taken when probing the surface on the atomic scale because the image also contains information of the local electron density distribution. Therefore, the atomic structure (e.g. of reconstructions) can only be determined from scanned STM images by combining experimental and theoretical approaches [82].

The spatial resolution of the STM is determined by the geometry and electronic structure of the tip and the mechanical stability of the instrument.

In this thesis, in-situ STM investigations of the morphology of Si surfaces (Chapter 4) and the growth morphology of ultrathin Al films on a Si(111)-$\sqrt{3} \times \sqrt{3}$-Al surface as function of film thickness (Chapter 3) have been carried out in an Aarhus STM 150 instrument.

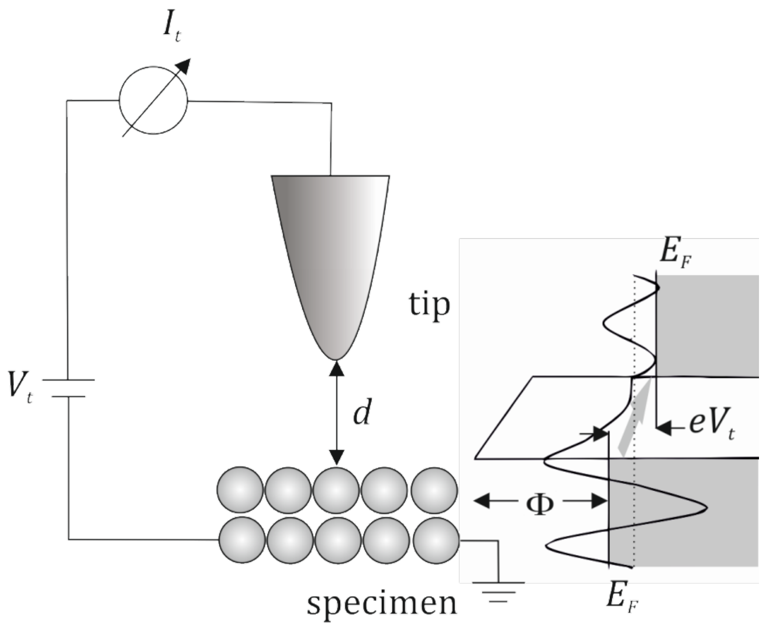

Fig. 1.4. Illustration of the working principle of STM. A metal tip is brought close to the specimen surface such that electrons from occupied states within eV_t above the Fermi level E_F on the negative side (here specimen) can tunnel into empty states within eV_t blow the Fermi level on the positive side (here tip). The resulting tunnel current I_t is measured. Adopted from [81].

1.5.3 *Angle-resolved X-Ray photoelectron spectroscopy (AR-XPS)*

The first commercial monochromatic XPS instrument became available in 1969 and ever since XPS has become one of the most commonly used analytical techniques in surface science, since it is sensible to almost all elements (except hydrogen and helium) as well as to their local chemical states in the (near)surface region [83,84].

The working principle of XPS is based on the analysis of the kinetic energy of photoelectrons, E_{kin}, that are emitted from the specimen upon irradiation with X-ray photons of characteristic energy $h\nu$. The surface sensitivity of XPS origins from the fact that, only those photoelectrons exited from the near surface regions can escape from the solid into the vacuum, whereas photoelectrons from deeper sample regions are inelastically scattered in the solid. Therefore, the investigated depth below the surface depends on the effective attenuation length of the photo electrons in the parent solid λ_{eff} (taking into account inelastic and elastic scattering) and the angle of detection with respect to the sample-surface normal α. The information depth is typically given by $3\lambda_{\mathrm{eff}} \cdot \cos\alpha$. The measured kinetic energy of photoelectrons is usually converted into a corresponding binding energy, E_{b}, by the following equation

$$E_{\mathrm{b}} = E_{\mathrm{kin}} - h\nu - \Phi \qquad (1.2)$$

where Φ denotes the work function of the specimen surface, which equals the known work function of the XPS spectrometer for the investigation of (grounded) conducting specimens [84,85].

The composition of the surface region of the solid can be determined from the ratio of the total primary zero loss (PZL) intensities of the detected core-level XPS spectra of the element constituents, as illustrated in this thesis for the investigation of continuous surface segregation of Ge during the growth of polycrystalline Ag films (Chapter 2), and for the quantification of adsorbed oxygen on Si surfaces (Chapter 4). Furthermore, the intensity ratios also provide information on the thickness and the composition of thin surface films, such as the oxide films formed upon thermal oxidation of Al surfaces (Chapter 5). For the present investigations, a Thermo VG Thetaprobe system with monochromatic Al-$K\alpha$ radiation was used, while simultaneously collecting all photoelectrons over an angle-detection range from α = 23° to 83°.

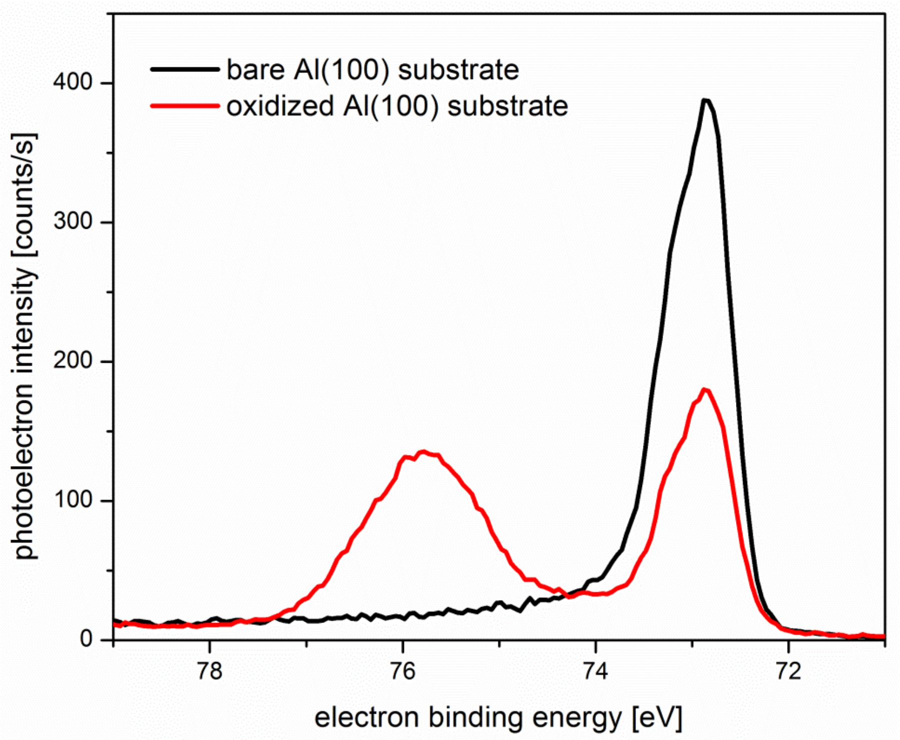

Fig. 1.5. Measured Al2p core level spectra of a clean Al(100) film surface and after exposure to pure oxygen at partial pressures up to 1 Pa at room temperature as recorded by XPS at a detection angle of 41.75° with respect to the sample surface normal.

1.5.4 High resolution transmission electron microscopy (HRTEM)

Transmission electron microscopy is an extremely powerful technique for the characterization of the microstructure of thin films on an atomic level. The working principle is based on the transmission and diffraction of high-energy electrons through a thin electron transparent specimen foil. Electrons are generated by field emitter or by thermal emission from a cathode, accelerated in an electric field and focused by a system of electromagnetic lenses and apertures onto the specimen foil. The transmitted, diffracted, and scattered electron wave functions are amplified and directed onto a screen [86,87].

The contrast in conventional TEM image usually results from the variation of intensity of diffraction across the sample (diffraction contrast), but also density variation (mass thickness contrast), leading to elastic and inelastic scattering of the electrons during their passage through the specimen, contribute to the image contrast. Contrary, in HRTEM the phase of the diffracted electrons is preserved and the image is formed by interference of diffracted beams and the direct beam (phase

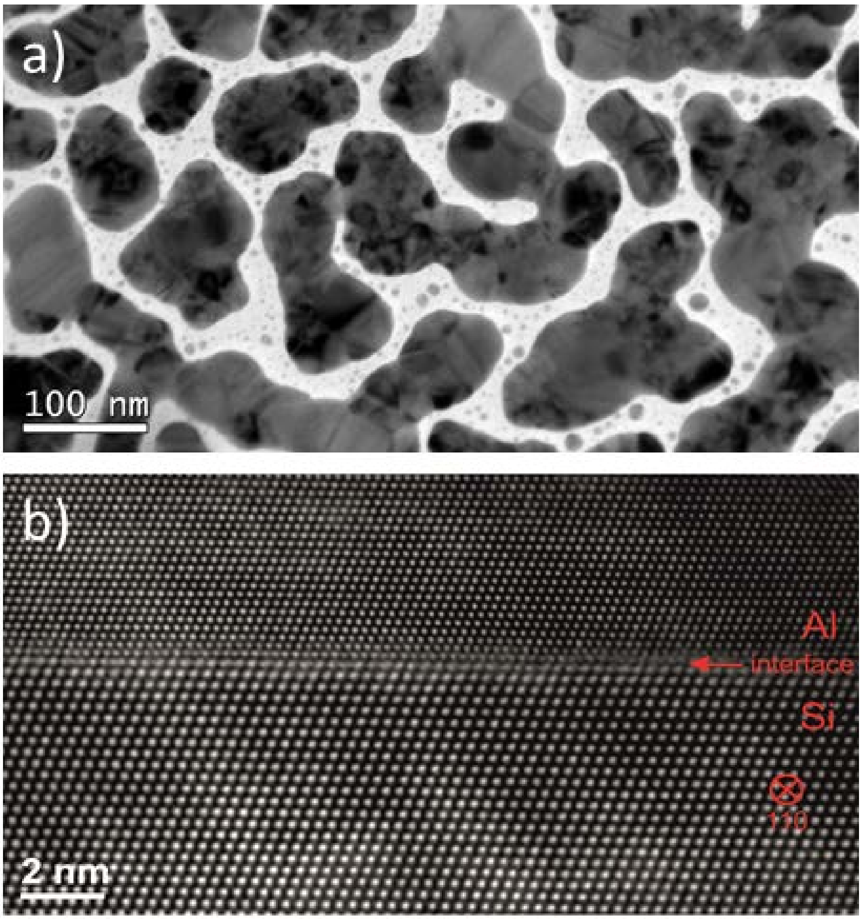

Fig. 1.6. (a) Bright field plane-view TEM image of coalescing islands during Ag film growth with a deposition rate of 3.9 nm/min on an amorphous SiO_2 surface at 50°C. Several crystal defects such as grain boundaries, stacking-faults and twins are visible. **(b)** HRTEM cross-section view along the [110] direction reveals that the interface between a epitaxialy grown Al(111) film on a Si(111)-$\sqrt{3} \times \sqrt{3}$-Al surface is atomically sharp.

contrast). Therefore, accurate control of illumination coherence and defect of focus are crucial factors for the image quality [86,88].

Preparation of electron transparent foils (thicknesses < 150 nm) from the bulk specimen is a precondition for TEM investigations, in order to avoid large contrast loss due to inelastic scattering of the electrons in the specimen. Maximum care has been taken in the current (HR)-TEM studies to avoid any preparation induced artifacts to the specimen microstructure [87]: The TEM specimens were either prepared by directly depositing the thin films on electron transparent membranes (Chapter 2) i.e., no further preparation steps had to be employed for microstructural analysis in plan-view, or, by firstly mechanically pre-thinning the specimen by a tripod polisher and secondly by ion milling (accelerating voltage of 2 keV) under liquid-nitrogen cooling for the cross-section TEM foils (Chapter 3 and 5). Subsequently, the specimens were investigated using a Philips CM 200, a JEOL 4000FX or a JEOL ARM electron microscopes operating at acceleration voltages of 200 kV, 400 kV and 1250 kV, respectively.

1.5.5 Real-time in-situ spectroscopic ellipsometry (RISE)

Ellipsometry is a non-destructive optical technique providing the possibility to characterize and observe tiny changes occurring at an interface or in a film between two media, such as the absorption of adlayers in the (sub)momolayer thickness regime and the growth of oxide films upon oxygen exposure of metal surfaces. According to the classic theory of Drude, the optical constants and film thickness can be determined from the change in the state of polarization that occurs when a beam of linearly polarized light interacts with the specimen [89,90].

The basic experimental setup is schematically sketched in Fig. 1.7. Light is emitted from a Xe lamp, linearly polarized by the polarizer with orthogonal s and p polarizations (in the plane of incident and perpendicular to it) and irradiated onto the specimen. Upon interaction of the linearly polarized light with the specimen, the polarization state of the reflected light is modified, i.e. it becomes elliptically polarized. The ellipsometric parameters Ψ and Δ are then given by the arctangent of the amplitude attenuation ratio upon reflection for the p and s polarizations and the relative phase difference between s and p polarizations, respectively [89].

In the present work, the ellipsometric investigation were performed with a J.A. Woollam M-2000L spectroscopic ellipsometer equipped with a Xe light source recording $\Delta(\lambda)$ and $\Psi(\lambda)$ in the wavelength range between 350 nm and 800 nm as function of time at a fixed incident and reflection angle of $\theta = 69.8°$ with respect to the specimen surface normal. In order to determine the oxide film growth curves upon oxygen exposure of Al surfaces (Chapter 5), the experimental data were fitted to a realistic optical model with a non-stoichiometric thin interface layer and a stoichiometric oxide film on top, as evidenced by AR-XPS analysis.

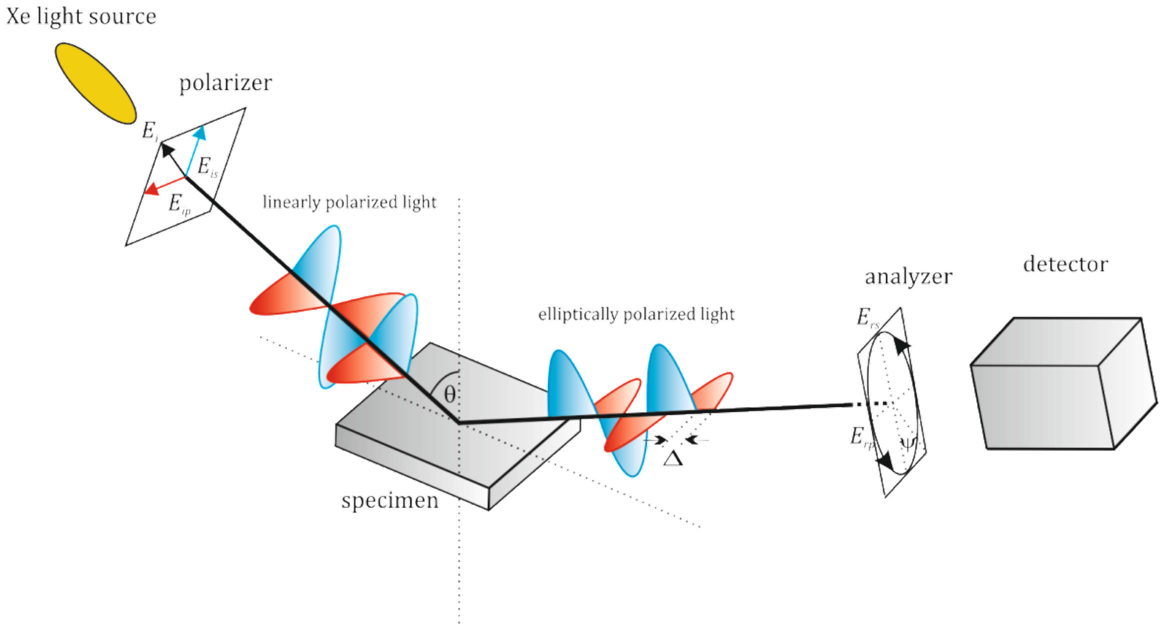

Fig. 1.7. Schematic sketch of the measurement principle of ellipsometry. Upon interaction of linearly polarized light with the specimen the polarization state of the reflected light is modified. Adopted from Ref. [90].

1.5.6 X-Ray diffraction (XRD)

X-Ray diffraction is one of the most important microstructure characterization technique used in materials science. It is based on Bragg´s law, $n\lambda = 2d_{\text{hkl}} \cdot \sin\Theta$, which defines the condition of diffraction for a X-ray beam with a wavelength λ inclining at an angle Θ on crystallographic planes with spacing d_{hkl} (h, k, l are the Miller indices). In the sample coordinate system the orientation of the diffraction vector $\vec{m}$, which is parallel to the angle bisector of the incident and the diffracted wave, is defined by the angles φ and ψ (see Fig. 1.8). Since only planes perpendicular to $\vec{m}$ contribute to the signal intensity, the distribution of crystallographic orientation in a specimen can be determined by varying the angles φ and ψ. Furthermore, the diffraction line profiles also provide information on the crystallite size and shape, the micro-strain, and the distribution of defects such as twins. According to the single-line analysis, the crystallite size and micro-strain can be determined from the broadening of the diffraction line profile by its deconvolution into Cauchy and Gaussian function components after the subtraction of the instrumental broadening [91,92].

In this project ex-situ XRD has been applied to investigate the effect of surface diffusivity on texture, crystallite size and shape of polycrystalline Ag films (Chapter

2). Furthermore, XRD has also been applied to verify the single-crystalline nature of the prepared Al films, which has been essential for the interpretation of measured data on the stress evolutions and the oxide film growth kinetics (Chapter 3 and Chapter 5).

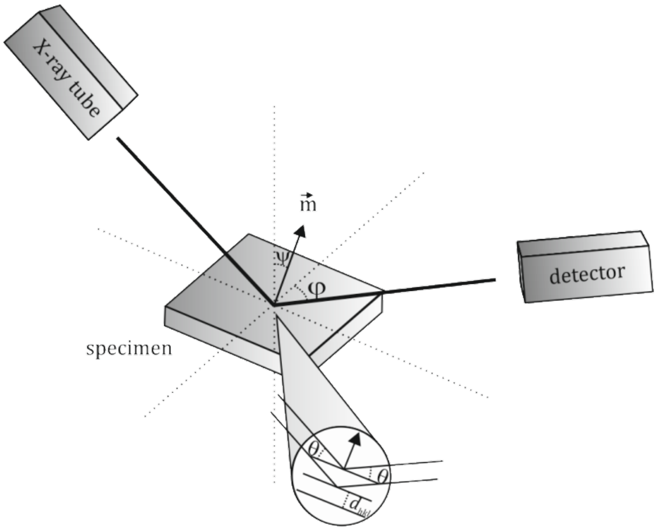

Fig. 1.8. Scheme showing the principle of XRD: only those lattice planes which fulfill the Bragg condition of diffraction contribute to the measured intensity.

References

[1] Z. I. Alferov, Rev. Mod. Phys. **73,** 767 (2001).

[2] L.B. Freund, S. Suresh, *Thin Film Materials* (Cambridge University Press, Cambridge, England, 2003).

[3] H. Kroemer, Rev. Mod. Phys. **73,** 783 (2001).

[4] D. Sander, J. Phys.: Condens. Matter **16,** R603 (2004).

[5] A. M. Smith, A. M. Mohs, and S. Nie, Nat. Nanotechnol. **4,** 56 (2009).

[6] C. V. Thompson, Annu. Rev. Mater. Sci. **30,** 159 (2000).

[7] J. A. Venables, G. D. T. Spiller, and M Hanbucken, Rep. Prog. Phys. **47,** 399 (1984).

[8] K. R. Lawless, Rep. Prog. Phys. **37,** 231 (1974).

[9] E. Bauer, Z. Kristallogr. **110,** 395 (1958).

[10] M. Ohring, *Materials science of thin films* (Academic Press, San Diego, 2002).

[11] Z. M. Wang, E. J. Mittemeijer, and L.P.H. Jeurgens, Int. J. Mater. Res. **100,** 1281 (2009).

[12] C.R.M. Grovenor, H. T. G. Henzell, and D.A. Smith, Acta metall. **32,** 733 (1984).

[13] D. L. Smith, *Thin-film deposition* (McGraw-Hill, New York, 1995).

[14] L. P. H. Jeurgens, A. Lyapin, and E. J. Mittemeijer, Acta Mater. **53,** 4871 (2005).

[15] N. Cabrera and N. F. Mott, Rep. Prog. Phys. **12,** 163 (1949).

[16] A. T. Fromhold, *Theory of Metal Oxidation* (North-Holland, Amsterdam, 1976).

[17] N. Birks *Introduction to the high-temperature oxidation of metals* (Cambridge University Press, Cambridge, UK 2006).

[18] A. T. Fromhold, Jr. and E. L. Cook, Phys. Rev. **158,** 600 (1967).

[19] F. Reichel, L. P. H. Jeurgens, and E. J. Mittemeijer, Acta Mater. **56,** 659 (2008).

[20] I. P. Batra and L. Kleinman, J. Electron Spectrosc. Rel. Phenom. **33,** 175 (1984).

[21] T. Kravchuk, R. Akhvlediani, V. V. Gridin, and A. Hoffman, Surf. Sci. **562,** 83 (2004).

[22] J.-X. Guo, L. Guan, F. Bian, Q.-X. Zhao, Y.-L. Wang, and B.-T. Liu, Surf. Interface Anal. **43,** 940 (2011).

[23] S. A. Larson and L. L. Lauderback, Surf. Sci. **284,** 1 (1993).

[24] H. Brune, J. Wintterlin, J. Trost, G. Ertl, J. Wiechers, and R. J. Behm, J. Chem. Phys. **99,** 2128 (1993).

[25] N. Cai, G. Zhou, K. Müller, and D. E. Starr, Phys. Rev. Lett. **107,** 035502 (2011).

[26] F. Reichel, L. P. H. Jeurgens, and E. J. Mittemeijer, Acta Mater. **56,** 2897 (2008).

[27] A. Hasnaoui, O. Politano, J. M. Salazar, and G. Aral, Phys. Rev. B **73,** 035427 (2006).

[28] G. Gutiérrez and B. Johansson, Phys. Rev. B **65,** 104202 (2002).

[29] R. C. Cammarata, Prog. Surf. Sci. **46,** 1 (1994).

[30] R. Abermann, R. Kramer, and J. Mäser, Thin Solid Films **52,** 215 (1978).

[31] W. D. Nix and B. M. Clemens, J. Mater. Res. **14,** 3467 (1999).

[32] L. B. Freund and E. Chason, J Appl. Phys. **89,** 4866 (2001).

[33] S. C. Seel, C. V. Thompson, S. J. Hearne, and J. A. Floro, J. Appl. Phys. **88,** 7079 (2000).

[34] R. Abermann, Vacuum **41,** 1279 (1990).

[35] R. W. Hoffman, Thin Solid Films **34,** 185 (1976).

[36] P. Zahl, P. Kury. and M. Horn von Hoegen, Appl. Phys. A **69,** 481 (1999).

[37] G. Wedler, J. Walz, T. Hesjedal, E. Chilla, and R. Koch, Surf. Sci. **402–404,** 290 (1998).

[38] F. C. Frank and J. H. van der Merwe, Proc. R. Soc. A **198,** 216 (1949).

[39] J. W. Matthews, J.Vac. Sci. Technol. **12,** 126 (1975).

[40] J. W. Matthews, *Dislocation in Solids* (Amsterdam, 1979), p. 461.

[41] J. H. van der Merwe and W. A. Jesser, J. Appl. Phys. **64,** 4968 (1988).

[42] E. A. Fitzgerald, Mater. Sci. Rep. **7,** 87 (1991).

[43] P. Chaudhari, J. Vac. Sci. Technol. **9,** 520 (1972).

[44] R. Shuttleworth, Proc. Phys. Soc. A **63,** 444 (1950).

[45] H. Ibach, Surf. Sci. Rep. **29,** 195 (1997).

[46] A. J. Schell-Sorokin and R. M. Tromp, Phys. Rev. Lett. **64,** 1039 (1990).

[47] H. Ibach, Surf. Sci. Rep. **35,** 71 (1999).

[48] D. Sander and H. Ibach, Phys. Rev. B **43,** 4263 (1991).

[49] W. Haiss, Rep. Prog. Phys. **64,** 591 (2001).

[50] C.-W. Pao, D. J. Srolovitz, and C. V. Thompson, Phys. Rev. B **74,** 155437 (2006).

[51] J. A. Floro, P. G. Kotula, S. C. Seel, and D. J. Srolovitz, Phys. Rev. Lett. **91,** 096101 (2003).

[52] S. G. Mayr and K. Samwer, Phys. Rev. Lett. **87,** 036105 (2001).

[53] R. C. Cammarata, K. Sieradzki, and F. Spaepen, J. Appl. Phys. **87,** 1227 (2000).

[54] C.-W. Pao and D. J. Srolovitz, Appl. Phys. Lett. **93,** 011903 (2008).

[55] A. L. Del Vecchio and F. Spaepen, J. Appl. Phys. **101,** 063518 (2007).

[56] F. Spaepen, Acta Mater. **48,** 31 (2000).

[57] C. Friesen and C. V. Thompson, Phys. Rev. Lett. **93,** 056104 (2004).

[58] T. K. Bhandakkar, E. Chason, and H. Gao, Phil. Mag. **90,** 3037 (2010).

[59] E. Chason, J. W. Shin, S. J. Hearne, and L. B. Freund, J. Appl. Phys. **111,** 083520 (2012).

[60] P. R. Guduru, E. Chason, and L. B. Freund, J. Mech. Phys. Solids **51,** 2127.

[61] E. Chason, B. W. Sheldon, L. B. Freund, J. A. Floro, and S. J. Hearne, Phys. Rev. Lett. **88,** 156103 (2002).

[62] C.-W. Pao, S. M. Foiles, E. B. Webb, III, D. J. Srolovitz, and J. A. Floro, Phys. Rev. B **79,** 224113 (2009).

[63] R. Krishnamurthy and D. J. Srolovitz, Acta Mater. **51,** 2171 (2003).

[64] B. Panicaud, J. L. Grosseau-Poussard, and J. F. Dinhut, Appl. Surf. Sci. **252,** 5700 (2006).

[65] Y. Kuru, M. Wohlschlögel, U. Welzel, and E. J. Mittemeijer, Thin Solid Films **516,** 7615 (2008).

[66] C. Friesen, S. C. Seel, and C. V. Thompson, J. Appl. Phys. **95,** 1011 (2004).

[67] R. Koch, Surf. Coat. Technol. **204,** 1973 (2010).

[68] J. Leib and C. V. Thompson, Phys. Rev. B **82,** 121402 (2010).

[69] H. P. Martinz and R. Abermann, Thin Solid Films **89,** 133 (1982).

[70] N. Cai, G. Zhou, K. Müller, and D. E. Starr, Phys. Rev. B **84,** 125445 (2011).

[71] B. Fu, W. An, C. H. Turner, and G. B. Thompson, Phys. Rev. Lett. **105,** 096101 (2010).

[72] J. W. Shin and E. Chason, Phys. Rev. Lett. **103,** 056102 (2009).

[73] J. Leib, R. Mönig, and C. V. Thompson, Phys. Rev. Lett. **102,** 256101 (2009).

[74] G. G. Stoney, Proc. R. Soc. A **82,** 172 (1909).

[75] E. Chason and B. W. Sheldon, Surf. Eng. **19,** 387 (2003).

[76] G. C. A. M. Janssen, M. M. Abdalla, F. van Keulen, B. R. Pujada, and B. van Venrooy, Thin Solid Films **517,** 1858 (2009).

[77] Y. Zhang, J. Appl. Mech. **75,** 011008 (2008).

[78] C. A. Klein, J. Appl. Phys. **88,** 5487 (2000).

[79] L. B. Freund, J. A. Floro, and E. Chason, Appl. Phys. Lett. **74,** 1987 (1999).

[80] D. A. Bonnell, *Scanning probe microscopy and spectroscopy* (Wiley-VCH, New York, 2001).

[81] C. J. Chen, *Introduction to scanning tunneling microscopy* (Oxford University Press, Oxford, 2008).

[82] J. A. Stroscio, *Scanning tunneling microscopy* (Academic Pr., Boston, 1993).

[83] D. Briggs, *Surface analysis by Auger and X-ray photoelectron spectroscopy* (SurfaceSpectra, Manchester, 2003).

[84] S. Hofmann, *Auger- and X-Ray Photoelectron Spectroscopy in Materials Science* (Springer, Berlin, Heidelberg, 2013).

[85] S. Hüfner, *Photoelectron spectroscopy* (Springer, Berlin, 2003).

[86] B. Fultz, *Transmission electron microscopy and diffractometry of materials* (Springer, Berlin 2002).

[87] D. B. Williams, *Transmission electron microscopy* (Springer, New York, 2009).

[88] J. C. H. Spence, *High-resolution electron microscopy* (Oxford University Press, Oxford, 2004).

[89] R. M. Azzam, *Ellipsometry and polarized light* (Amsterdam, North-Holland, 1979).

[90] E. Passaglia, *Ellipsometry in the measurement of surfaces and thin films* (U.S. National Bureau of Standards, Washington, DC, 1964).

[91] A. D. Krawitz, *Introduction to diffraction in materials science and engineering* (Wiley, New York, 2001).

[92] Modern Diffraction Methods by E.J. Mittemeijer and U. Welzel (Wiley-VCH, 2012)

Chapter 2

Effect of adatom surface diffusivity on microstructure and intrinsic stress evolutions during Ag film growth

D. Flötotto, Z. M. Wang, L. P. H. Jeurgens, E. Bischoff, and E. J. Mittemeijer

Abstract

The effect of the adatom surface diffusivity on the evolution of the microstructure and the intrinsic stress of thin metal films was investigated for the case of growth of polycrystalline Ag films on amorphous SiO_2 (a-SiO_2) and amorphous Ge (a-Ge) substrates, with high and low Ag adatom surface diffusivity, respectively. The surface diffusivity of the deposited Ag adatoms on the a-Ge substrate is suppressed also *after* coalescence of Ag islands due to the continuous (re)segregation of Ge at the surface of the growing film as evidenced by in-situ XPS. An assessment could be made of the role of adatom surface diffusivity on the microstructural development and the intrinsic stress evolution during film growth. As demonstrated by ex-situ TEM and ex-situ XRD, the Ag films grown on the a-SiO_2 and a-Ge substrates possess strikingly different microstructures in terms of grain shape, grain size and crystallographic texture. Nevertheless, the real-time in-situ stress measurements revealed a compressive→tensile→compressive stress evolution for the developing Ag films on both types of substrates, however on different time scales and with stress-component values of largely different magnitudes. It was concluded that (i) the microstructural development of metallic thin films is predominated by the *surface* diffusivity of the adatoms and (ii) the intrinsic stress evolution is largely controlled by the developing microstructure and the grain-boundary diffusivity.

2.1 Introduction

Thin films find numerous applications in modern engineering systems, such as surface coatings and micro-electro-mechanical systems. During fabrication and processing of these thin film systems, both *intrinsic* (i.e. arising during film growth) and *extrinsic* (i.e. induced after film growth; e.g. upon cooling/heating due to differences in thermal shrinkage/expansion of the various system components) residual stresses can arise. On the one hand, these residual film stresses can deteriorate the system's mechanical performance during operation, by causing excessive deformation, leading to fracture and/or spallation. On the other hand, the mechanical, electrical and magnetic properties of the film system may benefit from the controlled adjustment of the film stresses (cf. Refs. [1,2]). Thus, a fundamental, comprehensive understanding of the operating mechanisms of residual stress formation during thin film growth and operation is of great technological importance.

In recent years, the stress evolution during growth of a polycrystalline metal film, e.g. Ag, Cu and Au films on amorphous substrates (typically SiO_2), has been studied, in particular by real-time stress measurements.[3-12] As a result, two archetypes of the intrinsic stress evolution for the Volmer-Weber type of growth[1] of polycrystalline metal films were identified, depending on the homologous temperature, $T_h = T_s/T_m$, of the deposited metal (where T_s and T_m denote the substrate temperature during film growth and the melting temperature of the metal, respectively).[10] For the deposition of metals at *high* homologous temperatures (and thus for a relatively high atomic diffusivity in the evolving substrate/film system), as holds for e.g. Ag film growth at room temperature, the average film stress during continued film growth is initially compressive, then becomes tensile and subsequently becomes compressive again.[5,9,10] Metal film growth at *low* homologous temperatures (with a correspondingly *low* atomic diffusivity in the evolving substrate/film system), as holds for e.g. Fe film growth at room temperature, only results in the development of average film stresses of tensile nature.[10,13] Each of the above described intrinsic stress evolutions is characterized by the development of specific film microstructures: Films grown at high homologous temperatures develop columnar grain morphologies, whereas

---

[1] Volmer-Weber type of growth involves that, film growth proceeds by the initial nucleation of isolated islands on the parent substrate, which coalesce during continued deposition, thus forming a laterally-closed (continuous) film. Volmer-Weber type of growth involves that, film growth proceeds by the initial nucleation of isolated islands on the parent substrate, which coalesce during continued deposition, thus forming a laterally-closed (continuous) film [M. Volmer, and A. Weber, Z. Phys. Chem. **119**, 277 (1926)].

films grown at low homologous temperature form fine, equiaxed grain morphologies (cf. the so-called Structure Zone Model of thermally evaporated films [14]).

However, as demonstrated in the present paper, a general classification of stress and microstructure evolutions during metal film growth on the basis of solely the homologous temperature is very misleading, because the atomic diffusivity in the evolving film/substrate system comprises a number of also concurrent transport processes of the deposited metal (ad)atoms: i.e. diffusion along the parent substrate and developing film surfaces, along the grain boundaries and within the bulk of the growing film. As shown in this paper, it is essential to disclose the contribution of each of the different atomic transport processes to both the microstructural development and the generated stress.

In this study, the intrinsic stress evolution and the microstructural development during growth of polycrystalline Ag films on amorphous SiO_2 and amorphous Ge (a-Ge) substrates, by thermal evaporation under identical growth conditions, were investigated in a comparative manner. Ag/SiO_2 and Ag/a-Ge are important thin film systems for next-generation photovoltaic devices using plasmonic light trapping.[15],[16] Recognizing that Ag atoms have very different surface mobilities on a-Ge and on a-SiO_2 substrates (at the same substrate temperature)[17,18], this study aims at an assessment of the particular role of the surface diffusivity for the development of the intrinsic stress and the microstructure during film growth.

2.2 Experimental

2.2.1 Thin film growth

The experiments were carried out in a customized, multi-chamber UHV system (base pressure $< 3\times10^{-8}$ Pa) for *in-vacuo* specimen processing (e.g. cleaning and annealing), thin-film deposition by molecular beam epitaxy (MBE) and *in-situ* analysis by XPS.

Square-shaped (13.9×13.9 mm^2) Si (001) wafers (thickness: 100 μm) covered with a native amorphous oxide layer were ultrasonically cleaned successively in acetone and isopropanol. Next, the Si(001) wafers were loosely mounted in an especially-developed specimen holder for the in-situ stress measurements (see below), such that the wafer could bend freely in all directions during film deposition: this implies that the specimen holder is put in upside-down position during film deposition, so that the wafer is only held by gravity (i.e. resting on a three point-contact at the outer edges of the wafer). After introduction into the UHV system, the wafers were firstly preliminary degassed at 200 °C for 1 h in the fast-entry lock (base pressure < 10^{-6} Pa) and, subsequently, thoroughly degassed at 400 ºC for 1 h in the MBE chamber under UHV conditions (base pressure < 3×10^{-8} Pa). In-situ XPS analysis (see below) evidenced that adventitious carbon is the only contaminant on the degassed wafer surfaces. After cooling down to room temperature, Ag thin films were grown on the freshly degassed Si(001) wafer surfaces at about 50°C (with the native amorphous SiO_2 film preserved) by thermal evaporation of pure Ag (> 99.995 %) from a Al_2O_3 crucible using a high-temperature effusion cell (type HTC-40-10-1700-WK-SHP by Createc GmbH, Germany). The Ag deposition rate used in the present study were 3.9 nm/min and 2.1 nm/min and were determined in separate runs by (ex-situ) measurements of the film thickness after different deposition times with a Veeco DekTak profilometer.

In another series of experiments a 30 nm thick a-Ge film was deposited in-situ onto the degassed Si (001) wafer, prior to the deposition of the Ag film (by the same procedures as described above), by thermal evaporation of pure Ge (> 99.999 %) from a pyrolitic graphite (PGR) crucible using a high-temperature effusion cell (type HTC-40-2-250-WK-SH by Createc GmbH, Germany).

The two different types of substrate surfaces (SiO_2 and a-Ge), as employed for the subsequent (identical) Ag films deposition steps, will be further designated as *'Ox/Si'* substrate and *'Ge/Ox/Si'* substrate, respectively.

To investigate the microstructures of the Ag films at various stages of deposition by ex-situ TEM (see Sec. 2.3), Ag films were also deposited by evaporation for different deposition times (following the above procedures) on degassed 9 nm-thick amorphous Si membranes covered with native SiO_2 (SiMPore Inc.), as well as on degassed 9 nm-thick amorphous Si membranes covered with a 30 nm thick a-Ge layer.

2.2.2 In-situ stress analysis

To monitor in real time the stress-induced change in substrate curvature during film deposition, the multi-source MBE side-chamber is equipped with a multi-optical stress sensor (MOS) system[19] (k-space Associates) using a 3 x 3 array of parallel laser beams, which is aligned at normal incidence to the sample surface (i.e. single-port configuration). According to the Stoney equation,[20] the measured change in substrate curvature is proportional with the film force per unit of lateral width, i.e. the product of the thickness-averaged film stress and the mean film thickness. From a plot of the film force vs. the film thickness the following two quantities can be obtained: (i) The thickness-averaged film stress at deposition time t is given by the measured film force at time t divided by the mean film thickness at time t; (ii) The slope of the film-force curve at time t will be further designated as the incremental stress; its value is determined by the combined effects of instantaneous stress in the newly deposited part of the film and the (possible) stress change in the underlying (already deposited) film.

2.2.3 Microstructural analysis

TEM

The deposited Ag films (of thicknesses in the range of 3 nm - 100 nm) on the prepared Ox/Si and Ge/Ox/Si TEM membranes (see Sec. 2.1) were removed from the UHV system directly after growth and then immediately put into a Philips CM 200 transmission electron microscope (operating at an acceleration voltage of 200 kV) for microstructural analysis in planar view.

XRD

The crystallographic texture and grain/crystalite size of the Ag films on the Ox/Si and Ge/Ox/Si substrates were determined by recording (ex-situ) XRD ψ-scans (pole-figure sections) and θ-2θ-scans employing a Pro Philips X`Pert MRD diffractometer operating with Cu-$K\alpha$ radiation. The average grain sizes parallel and perpendicular to the film surface (further designated as lateral grain size and perpendicular grain size, respectively) were deduced by single-line analysis (after correction for instrumental broadening) [21,22] from the measured Ag [23] and Ag [24] reflections, both recorded at specimen tilt angles of 0° and 70.53°. The Bragg peaks were fitted with a pseudo-Voigt function (i.e. a convolution of a Cauchy and a

Gaussian profile) using the Profile Fit software from the manufacturer, employing linear background subtraction and a $K\alpha_2/K\alpha_1$ intensity ratio of 0.5.[25] Within the single-line analysis, the Cauchy component of the diffraction line profile is only due to finite crystallite size, whereas the Gaussian component results from microstrain. Within the experimental accuracy, the Gaussian contribution (i.e. the microstrain) in the Ag films grown on the Ox/Si and Ge/Ox/Si substrates was negligibly small.

XPS

The occurrence of surface segregation of Ge during growth of the Ag films on the Ge/Ox/Si substrates (as discussed in Sec. 3.4) was investigated by in-situ XPS measurement of the Ge 3d and 2p core-level spectra before Ag deposition, as well as after cumulative Ag film deposition steps (corresponding to Ag film thicknesses of 20, 50, 90, 140, 210 and 310 nm). The XPS analysis was performed using a Thermo VG Thetaprobe system employing monochromatic Al-$K\alpha$ radiation ($h\nu$=1486.68 eV; beam spot size of 400 μm), while operating the radian lens (i.e. a 180°-spherical-sector-analyzer with an exceptionally large angular acceptance range of 60°) in the so-called 'standard' lens mode by simultaneously collecting all photoelectrons over the detection angle range between 23° and 83° (with respect to the specimen surface normal; i.e. the central detection angle equals 53°).{Vinodh, 2004 #28} An angle-resolved-XPS (AR-XPS) measurement was performed also at an Ag film thickness of 50 nm in the so-called 'parallel' data acquisition mode, by detecting the photoelectrons simultaneously over the angular detection range from α=23° to α=83° in eight ranges of 7.5° each (α is the center of the corresponding angular detection range with respect to the sample-surface normal).{Vinodh, 2004 #28}

The total Ge 3d and Ge 2p primary zero loss (PZL; see Ref. [26]) intensities ($I_{\text{Ge 3d}}$ and $I_{\text{Ge 3p}}$) were obtained from the integrated area of the background-corrected Ge 3d and 2p spectra (applying a Shirley-type background), as recorded from the Ge/Ox/Si/ substrate before and after various Ag deposition steps. The surface coverage by Ge in monolayers (MLs; one atomic layer in Ge(111) taken as 0.327 nm) after each Ag deposition step was calculated from the PZL intensity ratios $I^{\infty}_{\text{Ge 3d}}/I_{\text{Ge 3d}}$ and $I^{\infty}_{\text{Ge 3p}}/I_{\text{Ge 3p}}$, as resolved from the measured Ge 3d and Ge 2p spectra of the bare substrate (i.e. $I^{\infty}_{\text{Ge 3d}}$ and $I^{\infty}_{\text{Ge 3p}}$) and the Ag-covered Ge/Ox/Si/ substrate (i.e. $I_{\text{Ge 3d}}$ and $I_{\text{Ge 3p}}$), respectively, according to the procedures described in Ref. [26]. The values for the effective attenuation lengths (EALs) of the detected Ge 3d and Ge 2p photoelectrons, as required in the thickness calculations, equal 2.992 nm and 0.899 nm, respectively (see Ref. {Vinodh, 2004 #28} and references therein). Note that the average information depth of the XPS analysis (as given by $3\lambda \cdot \cos \alpha$) is in the range of 8 - 1 nm and 2.5 - 0.3 nm with increasing angular detection range from α = 23º to α = 83º (see above) for the detected Ge 3d and Ge 2p photoelectrons, respectively.

2.3 Results

2.3.1 In-situ stress analysis

The measured film force and the calculated thickness-averaged stress (i.e. film force divided by mean film thickness) during Ag film growth on the Ox/Si and Ge/Ox/Si substrates (at a deposition rate of 3.9 nm/min) are shown as function of the mean film thickness in Figs. 2.1a and 2.1b, respectively. On both substrates the developing Ag films show a compressive → tensile → compressive stress evolution, which is typical for Volmer-Weber type of film growth of metals with a high atomic diffusivity at the deposition temperature (i.e. for deposition at high homologous temperatures), as holds for Ag deposition at room temperature (see Sec. 1) [9]. The durations (i.e. the thickness ranges) of the successive stress stages, as well as the corresponding magnitudes of the developed stresses, are distinctly different for both substrates (compare Figs. 2.1a and 2.1b): (i) For Ag film growth on Ox/Si, the initial compressive and subsequent tensile stress maxima are reached at thicknesses of 9 nm and 67 nm, respectively (Fig. 2.1a). For Ag film growth on Ge/Ox/Si, the initial compressive and subsequent tensile stress maxima are reached at much smaller thicknesses of 0.3 nm and 6 nm, respectively (Fig. 2.1b).

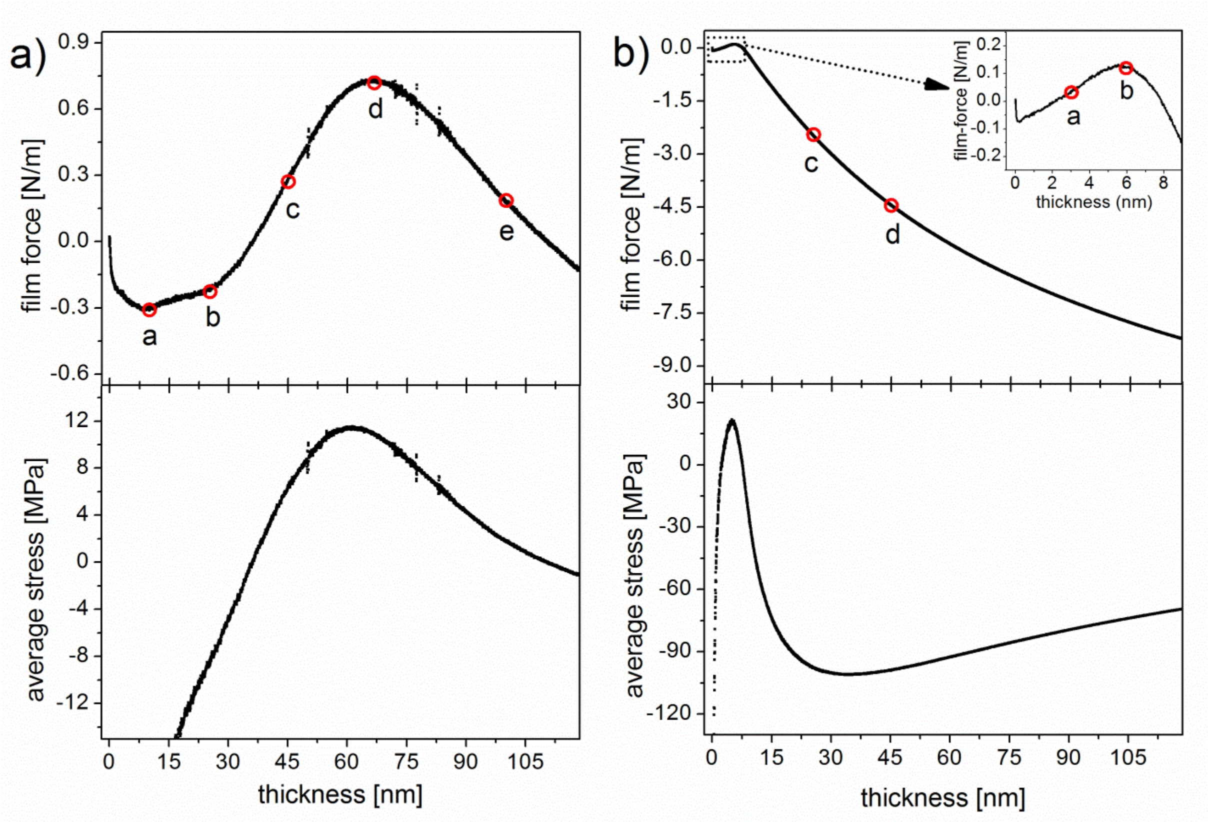

Fig. 2.1. Film force and thickness averaged stress of Ag films deposited at a deposition rate of 3.9 nm/min on **(a)** Ox/Si and **(b)** Ge/Ox/Si substrates. The stages corresponding to the thicknesses where TEM analyses were made (see Figs. 2.3 and 2.4) have been marked with red circles.

(ii) The average stress attained at the tensile maximum is more than two times smaller for the Ag film growing on Ox/Si than for the Ag film growing on Ge/Ox/Si (i.e. 11 MPa versus 23 MPa). (iii) The subsequent incremental compressive stress (i.e. the slope of the film force curve) is much smaller for the Ag film growing on Ox/Si than for the Ag film growing on Ge/Ox/Si (i.e. -19 MPa versus -103 MPa at thickness ranges of 80 nm-115 nm and 15 nm-40 nm, respectively).

In addition, reversible stress relaxations are observed during Ag film growth interruptions on both the Ge/Ox/Si and the Ox/Si substrate (see Fig. 2.2). The amount of relaxed stress is much larger for the Ag film grown on the Ge/Ox/Si substrate than on the Ox/Si substrates (i.e. 50 MPa versus 13 MPa at a thickness of 130 and 140 nm and, respectively.

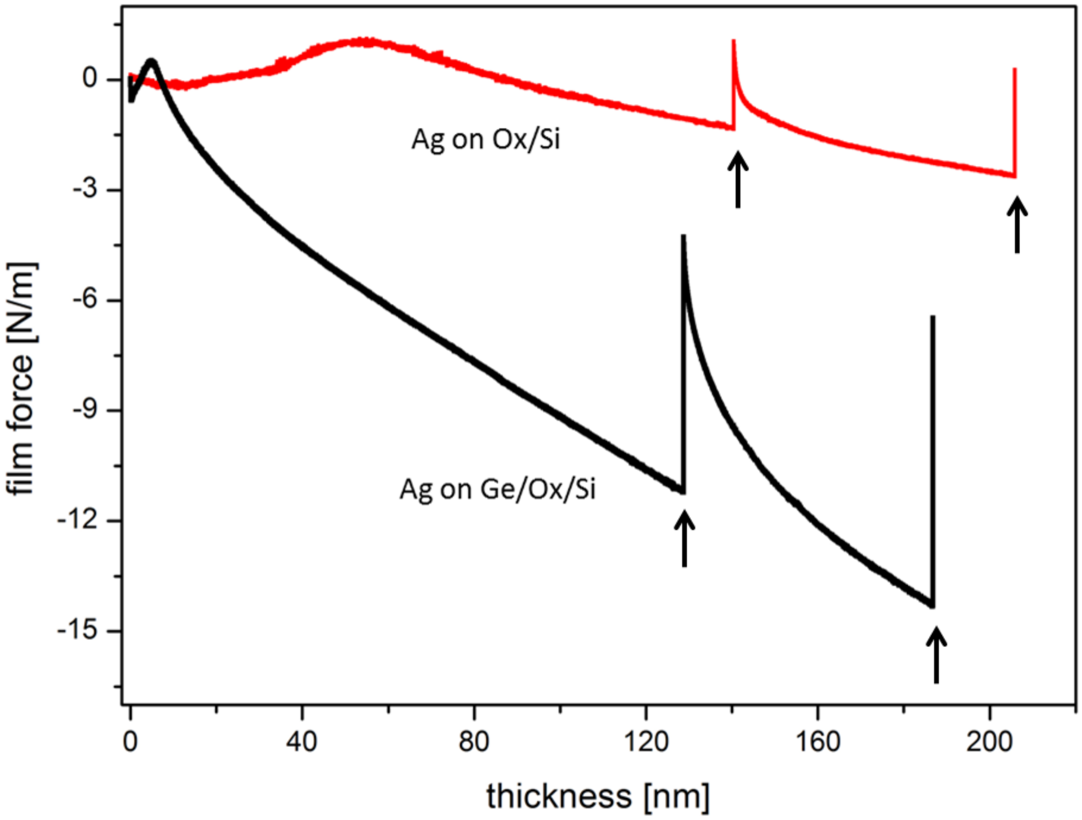

Fig. 2.2. Film force evolution of Ag films deposited at a deposition rate of 2.1 nm/min on the Ox/Si substrate (red) and the Ge/Ox/Si substrate (black). Upon interrupting the Ag film growth (see arrows in the figure), reversible stress relaxations are observed for both films.

2.3.2 Microstructural evolution

The development of the microstructure of the Ag films was investigated by plan-view TEM (cf. Sec. 2.2). TEM micrographs of the Ag films of various thicknesses on the Ox/Si and Ge/Ox/Si substrates are shown in Figs. 2.3 and 2.4, respectively (The stages of film growth pertaining to these micrographs have been indicated by circles an characters in Fig. 2.1 showing the film force vs. thickness behavior). Indeed (cf. Sec. 2.3.1), Ag film growth on both types of substrate proceeds by a Volmer-Weber-type growth mode, as characterized by successive (partially overlapping) stages of island nucleation, island growth and island impingement.

Well separated, predominantly single-crystalline Ag islands occur for the (nominally) 9-nm thick Ag film on Ox/Si (see Fig. 2.3a). The Ag islands start to impinge at a thickness of 25 nm, resulting in the formation of grain boundaries within the now much larger islands (Fig. 2.3b). Island coalescence progresses upon

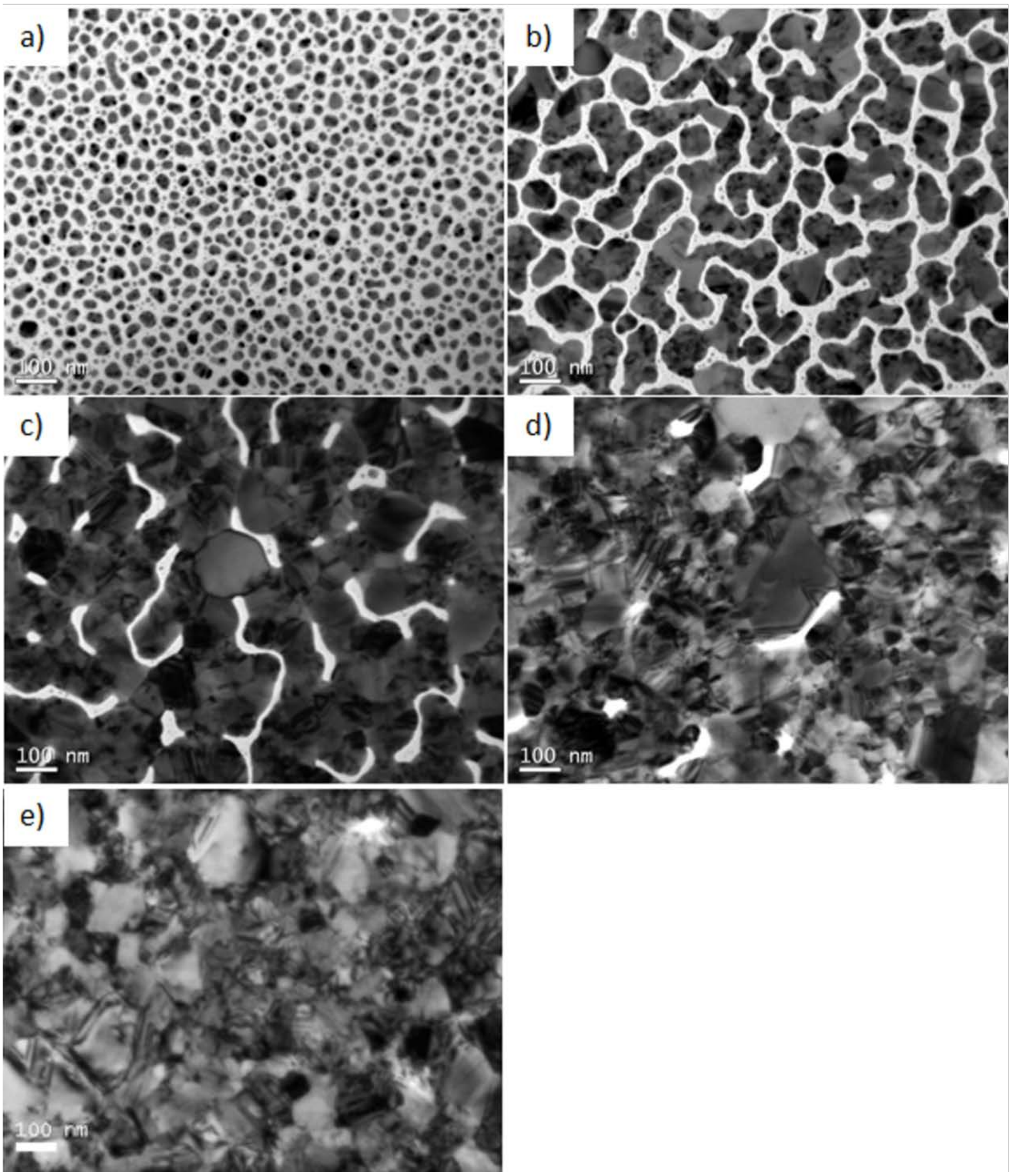

Fig. 2.3. Bright field plan-view TEM images taken at characteristic stages of Ag film growth (with a deposition rate of 3.9 nm/min) on Ox/Si substrate. The images correspond to mass equivalent Ag film thicknesses of **(a)** 9 nm **(b)** 25 nm **(c)** 45 nm **(d)** 67 nm **(e)** 100 nm. For a, b, c, d and e, see Fig. 2.1a.

continued Ag deposition and, consequently, the grain-boundary density increases with increasing thickness (see Fig. 2.3c pertaining to a thickness of 45 nm) until the Ag film becomes practically closed at a thickness of 67 nm (Fig. 2.3d). After formation of a closed Ag film (further referred to as the onset of the post-coalescence stage), the film microstructure does not change significantly upon

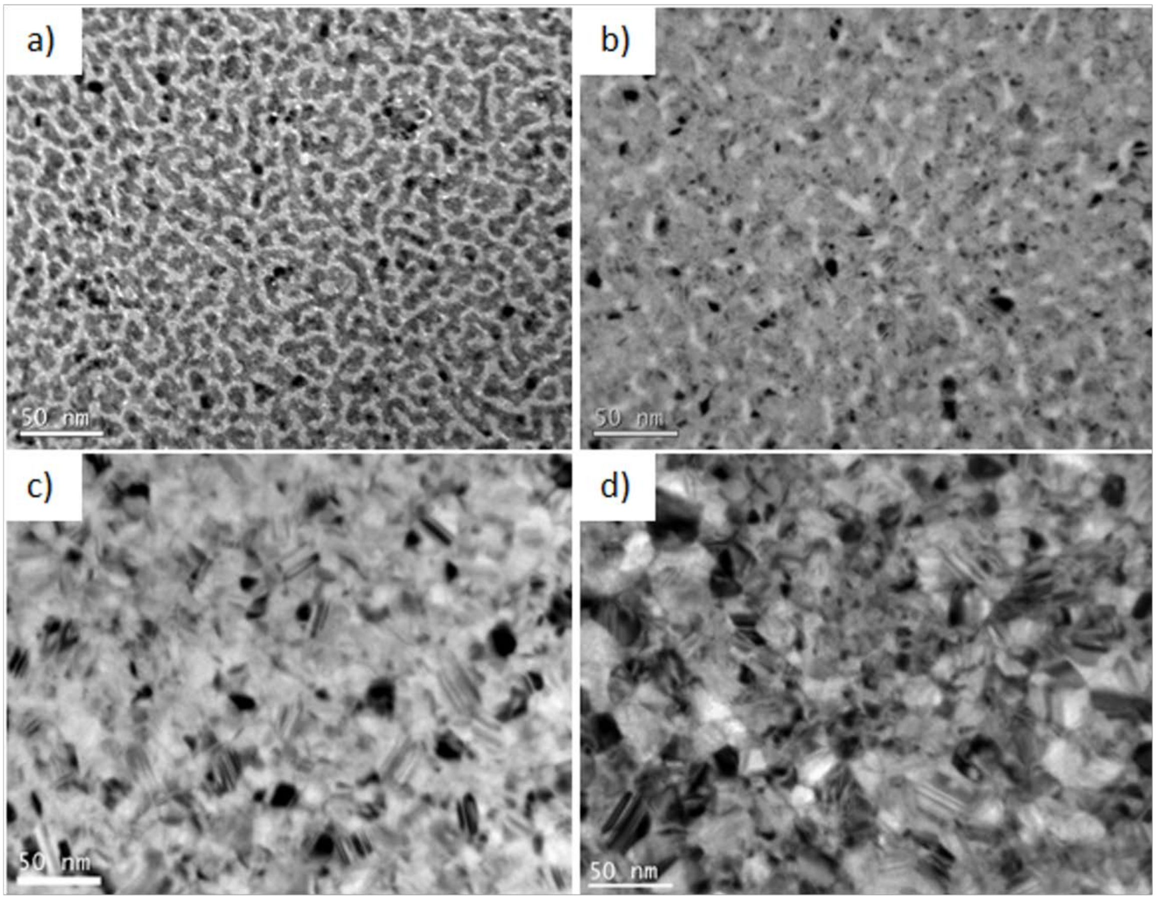

Fig. 2.4. Bright field plan-view TEM images taken at characteristic stages of Ag film growth (with a deposition rate of 3.9 nm/min) on Ge/Ox/Si substrate. The images correspond to mass equivalent Ag film thicknesses of **(a)** 3 nm **(b)** 6 nm **(c)** 25 nm **(d)** 45 nm. For a, b, c, and d, see Fig. 2.1(b).

further growth (Fig. 2.3e): Only a very slight increase of average grain size (i.e. by grain growth) is observed in the post-coalescence stage (cf. the TEM micrographs of the 67-nm and 100-nm thick Ag films shown in Figs. 2.3d and e, respectively).

The above described stages of growth occur at much smaller thicknesses during Ag film growth on the Ge/Ox/Si substrate. Island coalescence already takes place at a (nominal) Ag thickness of only 3 nm (see Fig. 2.4a and cf. Fig. 2.3b). At a film thickness of 6 nm, the Ge/Ox/Si substrate is largely covered by small Ag nano-grains with an average grain size of 10 nm (see Fig. 2.4b). Already at a film thickness of 25 nm (Fig. 2.4c), the Ag film is completely continuous, containing very fine Ag grains, with an average size of 21 nm, which increase slightly in size by grain growth during the post-coalescence stage to 25 nm for the 45 nm thick Ag film (Fig. 2.4d).

2.3.3 Texture and grain morphology

The texture (preferred orientation) of the Ag films on the Ox/Si and Ge/Ox/Si substrates was investigated by XRD: The Ag film on the Ox/Si substrate shows a strong and sharp {111} fiber texture (evidenced by the occurrence of dominant peaks at ψ =0° and 70.5° in the Ag {111} ψ-scan (pole-figure section; see Fig. 2.5) recorded at $2\theta = 38.2°$), which is expected for polycrystalline thin films of fcc metals (due to the relatively low surface energy of {111} orientated grains [27]). The small peak at ψ = 56° can be ascribed to twinning on (111) planes, inclined with respect to the surface, of the {111} fiber texture component, leading to a texture component with (511) planes parallel to the film surface.

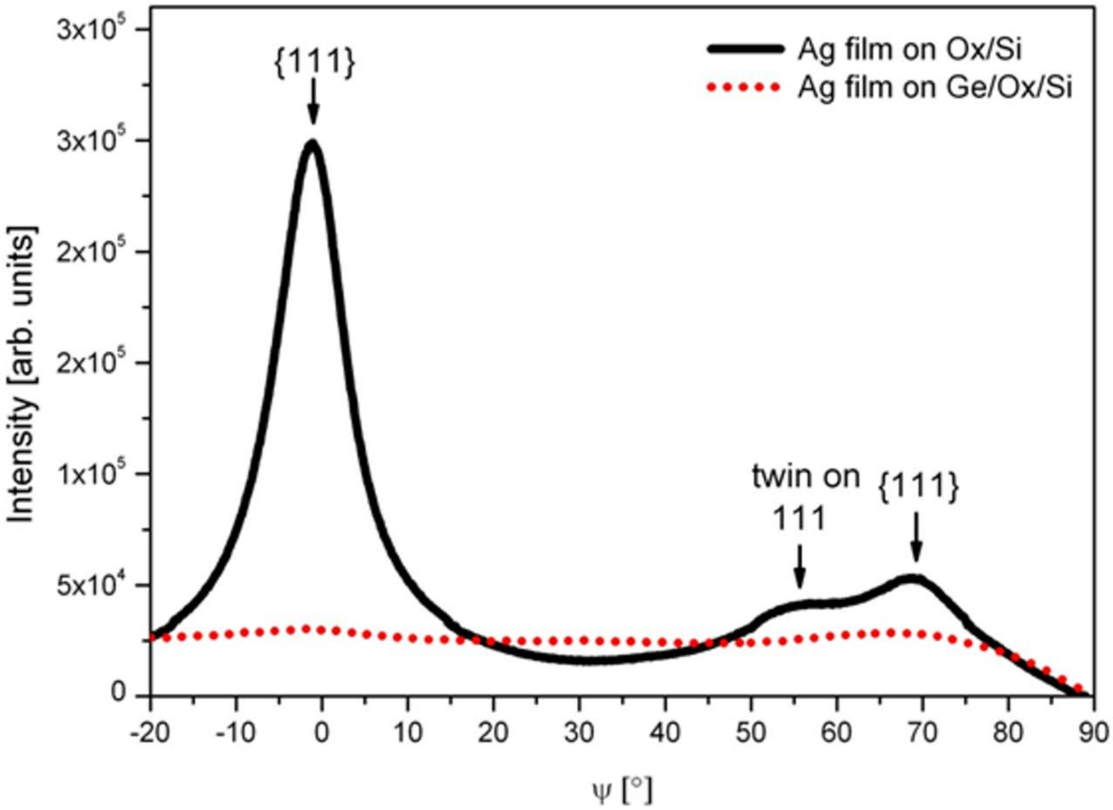

Fig. 2.5. XRD ψ-scans (pole-figure sections) recorded for the Ag 111 reflection (at $2\theta = 38.2°$) of Ag films deposited on Ox/Si and Ge/Ox/Si substrates. The {111} planes parallel to the surface, representing the fibre-texture component for the Ag film on the Ox/Si substrate, give rise to peaks at ψ =0° and 70.5°. The peak at ψ = 56° can be ascribed to twinning on {111} planes, inclined with respect to the surface, of the {111} fiber texture component leading to a texture component with {511} planes parallel to the film surface. The Ag film on the Ge/Ox/Si substrate is practically texture-less.

On the contrary the Ag film grown on the Ge/Ox/Si substrate is almost *texture-less*; i.e. the Ag grains are randomly oriented (see dotted line in Fig. 2.5).

The average grain/crystallite size and grain/crystallite morphology in the Ag films were determined by XRD line-profile analyses (see Sec. 2). It follows that the Ag film on the Ox/Si substrate possesses a columnar grain structure: for the 205 nm thick Ag film the average lateral (= parallel to the surface) grain size is 43 nm and the average perpendicular (to the surface) grain size is 89 nm [28]. The Ag film on the Ge/Ox/Si substrate exhibits an equiaxed nano-grain structure with equal average lateral and average perpendicular sizes: for the 280 nm thick Ag film the lateral and perpendicular grain sizes are 19 nm, in accordance with the TEM analysis (see Fig. 2.4).

2.3.4 Ge surface segregation during Ag deposition on the Ge/Ox/Si substrate

The Ge 3d and Ge 2p photoelectrons are detectable for the Ag films grown on the Ge/Ox/Si substrate at Ag thicknesses as large as 310 nm, i.e. very much larger than the information depths of the XPS analyses (see Sec. 2.2.3). This indicates that, during the Ag film growth, Ge segregation to the Ag film surface takes place (this process can be driven by lowering of the surface energy[2]).

In order to disclose whether the segregated Ge atoms are located homogeneously at the Ag film surface or rather agglomerated at the Ag grain boundaries or at the surface/grain-boundary junctions, an AR-XPS measurement was performed at an Ag film thickness of 50 nm. As revealed by the AR-XPS results shown in the inset of Fig. 2.6, the ratio of the asymmetry-factor-corrected (see Ref. [29]) photoelectron intensities of the Ge 3d and Ag 3d peaks increases with increasing detection angle α (relative to the sample-surface normal) from 26º to 72º. The increase of the photoelectron-intensity ratio is proportional to the inverse of cos(α) (see inset of Fig. 2.6). Such 1/cos(α) dependence, as predicted by theoretical models for submonolayer surface adsorption systems,[30] thus confirms that the segregated Ge is exclusively located at the growing Ag film surface rather than at the

---

[2] The surface energies of a-Ge and Ag at the growth (room) temperature are equal to 0.7 J/m^2 and 1.4 J/m^2, respectively [Z. M. Wang, J. Y. Wang, L. P.H. Jeurgens, and E. J. Mittemeijer, Phys. Rev. B **77**, 045424 (2008)]. The surface segregation of Ge atoms to the Ag film surface at these strikingly low temperatures (i.e. room temperature) can occur because the (relatively strong) covalent bonds in the a-Ge substrate are weakened at the interface with the Ag film on top, as also observed in various metal-semiconductor contacts [A. Hiraki, Surf. Sci. Rep., **3**, 357 (1983)].

Ag grain boundaries or at the surface/grain-boundary junctions. This observation is consistent with the thermodynamic recognition that Ag and Ge are fully *immiscible* at room temperature[31] (i.e. a large *positive* enthalpy of intermixing exists) and therefore, Ge atoms tend to stay at the low-coordination Ag surface sites rather than at high-coordination Ag grain-boundary sites.

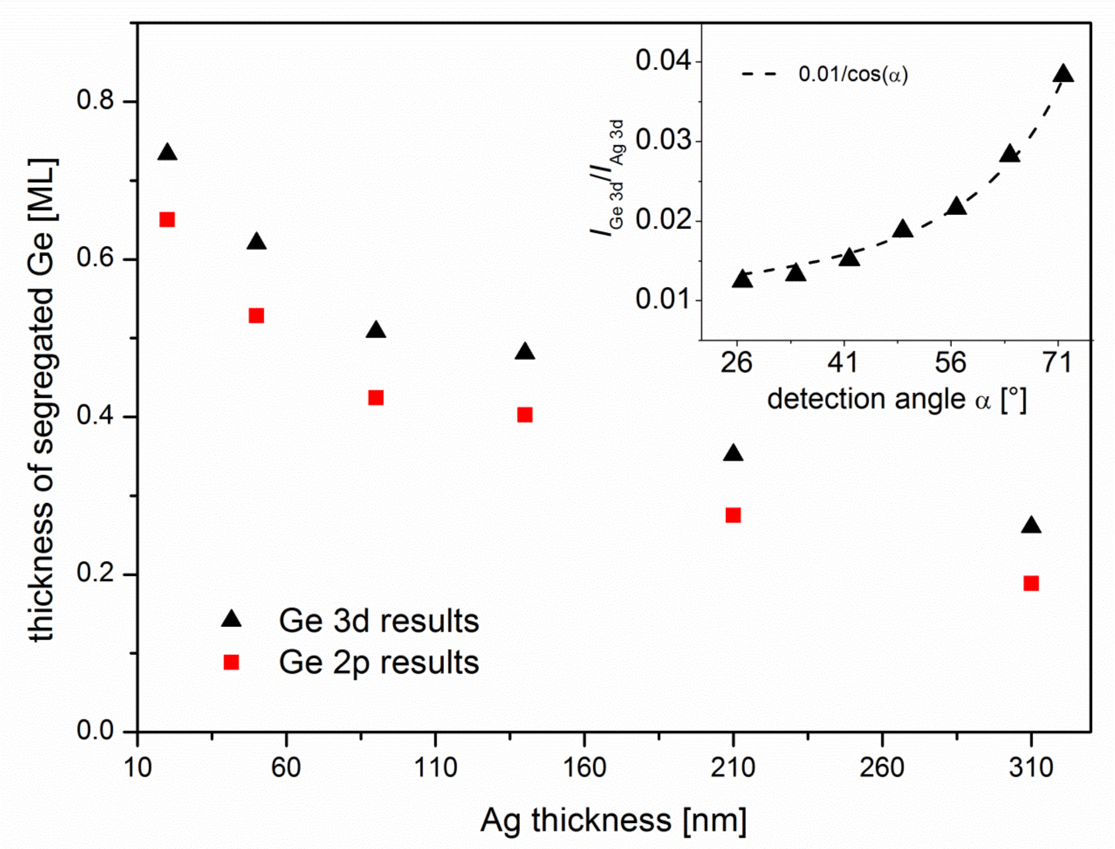

Fig. 2.6: Surface coverage by the segregated Ge (given in monolayers (MLs); one ML equals the thickness of one atomic (111) layer of Ge), as separately determined from the resolved Ge 2p and Ge 3d photoelectron intensities, as function of Ag film thickness. The inset shows the ratio of the asymmetry-factor-corrected intensities of the Ge 3d and Ag 3d peaks, $I_{\mathrm{Ge\ 3d}}/I_{\mathrm{Ag\ 3d}}$, as function of the detection angle α at a Ag film thickness of 50 nm. The ratio increases proportionally to 1/cos(α), indicating that the segregating Ge atoms are located at the top surface of the Ag film.

The surface coverage by the segregated Ge layer, expressed in monolayers (MLs) and as separately estimated from the measured Ge 3d and Ge 2p photoelectron intensities (see Sec. 2.2), has been plotted as function of the Ag film thickness in Fig. 2.5. Although the EALs (and thus the information depths; see Sec. 2) of the detected Ge 3d and Ge 2p photoelectrons are different (3 nm vs. 0.9 nm, see Sec. 2.2), the values determined for the thickness of the segregated Ge layer at the surface of the Ag film, on the basis of the separate resolved Ge 3d and Ge 2p photoelectron intensities, are similar. The results show that the Ge surface coverage during Ag deposition is well below one ML; it gradually decreases from about 0.7 ML to 0.2 ML for an increase in Ag film thickness from 20 nm to 310 nm. Evidently, Ge from the Ge/Ox/Si substrate (see Sec. 2.2) segregates to the Ag film surface at the onset of Ag deposition. This initially segregated Ge layer then continuously resegregates to the film surface during continued deposition. The observed decrease of the Ge surface coverage with increasing Ag film thickness (see Fig. 2.6) can be explained by a partial incorporation of the initially segregated Ge atoms underneath the surface during continued film growth due to a relatively low Ge segregation rate as compared to the Ag deposition rate.

2.4 Discussion

2.4.1 Effect of the adatom surface diffusivity on the microstructural evolution

At the onset of the deposition process, the nucleation of Ag islands on the parent a-SiO_2 and a-Ge surfaces competes with the further growth of already nucleated Ag islands (by trapping diffusing Ag adatoms in their vicinity). The activation energy for diffusion of Ag is significantly higher on the a-Ge surface than on the a-SiO_2 surface (0.45 eV vs. 0.32 eV [17], [18]); hence the average diffusion length of Ag adatoms is much smaller on the parent a-Ge surface than on the parent a-SiO_2 surface (for the same substrate temperature). Consequently, growth of already existing Ag islands by adding Ag adatoms by surface diffusion, as compared to the formation of new islands, is less pronounced on the a-Ge surface than on the a-SiO_2 surface. Hence, for the parent a-Ge surface, and as compared to the parent a-SiO_2 surface, the combination of a relatively low diffusivity of the Ag adatoms and the (correspondingly) higher initial density of islands promotes the formation of a closed Ag film with relatively small grain size, in accordance with the experimental observations (see Sec. 2.3). This smaller grain size upon film coalescence implies a much higher grain-boundary density of the Ag film on the Ge/Ox/Si substrate in the post-coalescence stage (as compared to the Ox/Si substrate): compare Figs. 2.3d and 2.4b.

The differences in the microstructural evolution of the Ag films on both substrates cannot only be ascribed to the *initial* difference in surface mobility of the Ag adatoms on the *parent* Ox/Si and Ge/Ox/Si substrates at the onset of the deposition (as discussed above), but also evolve by a maintained difference in surface diffusivity of the Ag adatoms on the *developing* Ag film surfaces upon continued film growth during the post-coalescence stage (see what follows).

The activation energy of 0.1 eV [17] for diffusion of Ag on Ag(111) surfaces is significantly lower than the aforementioned activation energies of 0.32 eV and 0.45 eV for Ag diffusion on the a-SiO_2 surface and the a-Ge surface, respectively. Consequently, the diffusion length of Ag adatoms on the Ag film surfaces on the Ox/Si substrate is large enough to allow the continuous incorporation of the Ag adatoms in existing grains, preferentially those with an energetically favored {111} plane parallel to the film surface. The Ag film grown on the Ox/Si substrate thus develops a columnar grain morphology with a strong and sharp {111} texture. This type of microstructure, developing at a homologous temperature of T_h = 0.3, is compatible with the Zone II-type of microstructure developing at homologous deposition temperatures in the range of T_h = 0.3 - 0.5, according to the Structure Zone Model.[14]

The absence of such a columnar microstructure for the Ag film grown on the Ge/Ox/Si substrate at the *same homologous temperature* of T_h = 0.3 can be understood as follows: The submonolayer of (re-)segregating Ge at the Ag film surface (see Fig. 2.6) significantly retards the surface diffusion of the Ag adatoms also during the post-coalesence stage, thereby promoting continued nucleation of new Ag grains during film growth. Furthermore, since grain growth in Ag thin films at temperatures of 0.2 T_m - 0.3 T_m is predominantly controlled by surface diffusion of Ag atoms,[14,32] the significantly reduced surface diffusion by segregating Ge further hinders the occurrence of growth of the already formed Ag grains. As a consequence the Ag film on the Ge/Ox/Si substrate develops a fine, equiaxed grain morphology without texture. In the absence of the continuous suppression of the Ag adatom surface diffusivity by the Ge (re-) segregation effect, such textureless films exhibiting an equiaxed grain morphology only develop at significant lower homologous temperatures, T_h < 0.2 (pertaining to the Zone I-type of microstructure of the Structure Zone Model [14]).

2.4.2 Effect of adatom surface diffusivity on the intrinsic stress evolution

As revealed by the measured stress evolutions and the corresponding TEM observations of the developing film microstructure during Ag film growth on the Ox/Si and Ge/Ox/Si substrates (compare Figs. 2.1a and 2.3, as well as Figs. 2.1b and 2.4), the generation of compressive stress during the initial stage of film deposition correlates with the nucleation and growth of isolated islands on the parent substrate surfaces (e.g. see Figs. 2.1a and 2.3a). The generation of compressive (intrinsic) stress during island growth can be attributed to the presence of a (positive) surface stress that acts on an individual island and the strength of the adhesion of the individual island with the substrate, as follows.[33,34] For an *unconstrained* island, the acting surface stress induces an equilibrium lattice spacing of the island that is lower than that of the corresponding bulk metal; the value of this equilibrium lattice spacing increases with increasing island size. Upon increasing (lateral) island size atomic rearrangements at the island/substrate interface become increasingly difficult. As a result, the increase of the *strived-for* equilibrium lattice spacing during island growth is associated with the development of a compressive stress component in the island parallel to the island/substrate interface.

As the deposition proceeds, the isolated islands grow and coalesce, thereby forming grain boundaries. The interatomic forces acting across the developing grain boundaries induce a tensile stress component in the film parallel to the film surface (e.g. see Figs. 2.1a and 2.3 b-d); the magnitude of this component of generated tensile stress is proportional with the amount of formed grain boundaries per unit area of film. The grain-boundary density is much larger for the growing Ag film on the Ge/Ox/Si substrate than on the Ox/Si substrate (see Secs. 2.3.2 and 2.3.3) and, consequently, the average tensile stress component emerging during film coalescence is considerably larger for the film on the Ge/Ox/Si substrate (as compared to the Ag film on the Ox/Si substrate): compare Figs. 2.1a and 2.1b. For both films, the end of the island-coalescence stage (i.e. the stage at which a closed Ag film has formed) corresponds well with the occurrence of the tensile stress maximum (compare Figs. 2.1a and 2.3d and Fig. 2.1b and 2.4b).

Although the Ag films developing on the Ox/Si and Ge/Ox/Si substrates exhibit strikingly different microstructures (see Secs. 2.3.2 and 2.3.3), continued deposition during the post-coalesence stage results in the (re)appearance of a compressive stress component as well as reversible stress relaxations during Ag film growth interruptions for the Ag films on *both* types of substrates.

The present experimental findings, that Ag films with largely different adatom surface diffusivities (see the discussion in Sec. 2.4.1) and strikingly different film microstructures exhibit, similarly, the emergence of a post-coalescence compressive stress component as well as reversible stress relaxations, allow a more sophisticated classification of stress-evolution behavior during polycrystalline film growth, which was so far simply based on the atomic mobility (i.e. the homologous temperature).[9,10] A high adatom surface diffusivity and the development of a textured, columnar microstructure (which do not occur for the Ag film growing on the Ge/Ox/Si substrate) are evidently not decisive factors for the post-coalescence compressive stress generating mechanism.

The emergence of a post-coalescence compressive stress component for both types of Ag films can be reduced to the same denominator by departing from a concept proposed in Ref. 4. Recognizing the non-equilibrium nature of film *growth,* the chemical potential of Ag adatoms at the film surface is significantly larger than that of Ag (ad)atoms in the film grain boundaries. Therefore a reduction of Gibbs energy of the system during the post-coalescence growth stage can be realized by the transport of the adatoms from the supersaturated film surface into the film grain boundaries, in association with, firstly, the relaxation of the tensile stress contribution (see above discussion) and, subsequently, the buildup of a compressive stress contribution. This stress contribution can be significant provided the grain-boundary diffusion rate is large with respect to the layer-growth rate.

Because for the Ag film growing on the Ge/Ox/Si substrate, (re)segregated Ge atoms are exclusively located at the growing Ag film surface (see Sec. 2.3.4), only the Ag adatom surface diffusivity is suppressed, whereas, due to the absence of Ge at the developing film grain boundaries, the grain-boundary diffusivity of Ag (ad)atoms is unaffected, thereby allowing operation of the same compressive stress generating mechanism as described above.

The above interpretation of the emerging post-coalescence compressive stress component as well as reversible stress relaxations during growth interruptions is moreover supported by the much larger value of the compressive stress contribution and the much larger value of relaxed stress observed for the fine-grained Ag film (i.e. the film on the Ge/Ox/Si substrate) as compared to the much coarser grained Ag film (i.e. the film on the Ox/Si substrate): -103 MPa versus -19 MPa and 50 MPa versus 13 MPa ; c.f. Figs. 2.1a, 2.1b and 2.2.

2.5 Conclusions

The adatom surface diffusivity has a dramatic impact on the microstructural development of polycrystalline Ag films during growth at a homologous temperature of $T_h \approx 0.3$:

The Ag film deposited on the SiO_2 substrate possesses a columnar, surface-energy minimizing {111} fiber textured microstructure, due to a relatively high Ag adatom surface diffusivity allowing incorporation of Ag adatoms in already existing grains during continued film growth.

The distinctly lower diffusivity of Ag adatoms on the a-Ge substrate (as compared to the a-SiO_2 substrate) enhances the initial nucleation of Ag islands and at the same time suppresses the growth of (initially) formed Ag islands on the parent substrate surface. The surface diffusivity of the Ag adatoms is also lowered *during thickening* of the laterally closed Ag film on the a-Ge substrate, due to the continuous and exclusive (re)segregation of Ge to the film surface. As a consequence of the thus maintained lower adatom surface diffusivity, continuous nucleation of new Ag grains takes place and a fine, equiaxed, texture-less, microstructure is formed.

The Ag films growing on both types of substrates, at similar conditions, both experience the development of compressive→tensile→compressive contributions of stress parallel to the film/substrate interface, albeit at different times and of different magnitudes.

Irrespective of the great differences in film microstructure, the various, successive stress-inducing mechanisms are identified as: (i) a positive surface stress in combination with a rigidity of the atomic structure at the island/substrate interface increasing with island size causes the initial compressive stress ; (ii) the coalescence of the islands and the interatomic forces acting across the resulting grain boundaries lead to a tensile stress component; (iii) the diffusion of adatoms into the grain boundaries of the growing film generate the final compressive stress contribution.

The much larger grain-boundary density of the Ag film growing on the a-Ge substrate corresponds with much larger stress contributions (ii) and (iii) as compared to those of the relatively coarse grained Ag film on the a-SiO_2 substrate.

The generally adopted classification of the stress and microstructure evolutions in a high and a low mobitity type of growth only on the basis of the homologous temperature is (much) too crude. This study demonstrates that the microstructural evolution of metallic thin films is predominantly governed by the adatom *surface* diffusivity and that the intrinsic stress evolution is largely controlled by both the developing microstructure and the grain-boundary diffusivity.

References

[1] L.B. Freund and S. Suresh, *Thin Film Materials* (Cambridge University Press, Cambridge, England, 2003).

[2] D. Sander, J. Phys.: Condens. Matter **16,** R603 (2004).

[3] R. Abermann and R. Koch, Thin Solid Films **129,** 71 (1985).

[4] E. Chason, B. W. Sheldon, L. B. Freund, J. A. Floro, and S. J. Hearne, Phys. Rev. Lett. **88,** 156103 (2002).

[5] J. A. Floro, S. J. Hearne, J. A. Hunter, P. Kotula, E. Chason, S. C. Seel, and C. V. Thompson, J. Appl. Phys. **89,** 4886 (2001).

[6] C. Friesen and C. V. Thompson, Phys. Rev. Lett. **89,** 126103 (2002).

[7] R. W. Hoffman, Thin Solid Films **34,** 185 (1976).

[8] R. Koch, J. Phys.: Condens. Matter **6,** 9519 (1994).

[9] R. Koch, Surf. Coat. Technol. **204,** 1973 (2010).

[10] R. Abermann, Vacuum **41,** 1279 (1990).

[11] A. L. Del Vecchio and F. Spaepen, J. Appl. Phys. **101,** 063518 (2007).

[12] C. Friesen, S. C. Seel, and C. V. Thompson, J. Appl. Phys. **95,** 1011 (2004).

[13] G. Thurner and R. Abermann, Thin Solid Films **192,** 277 (1990).

[14] H. T. G. H. C.R.M. Grovenor, D.A. Smith, Acta metall. **32,** 733 (1984).

[15] H. A. Atwater and A. Polman, Nature Mater **9,** 205 (2010).

[16] V. J. Logeeswaran, N. P. Kobayashi, M. S. Islam, W. Wu, P. Chaturvedi, N. X. Fang, S. Y. Wang, and R. S. Williams, Nano Lett. **9,** 178 (2008).

[17] E. G. Seebauer and C. E. Allen, Prog. Surf. Sci. **49,** 265 (1995).

[18] H. C. Kim, T. L. Alford, and D. R. Allee, Appl. Phys. Lett. **81,** 4287 (2002).

[19] E. Chason and B. W. Sheldon, Surf. Eng. **19,** 387 (2003).

[20] G. G. Stoney, Proc. R. Soc. A **82,** 172 (1909).

[21] E. J. Mittemeijer and U. Welzel, Z. Kristall. **223,** 552 (2008).

[22] T. H. Dekeijser, J. I. Langford, E. J. Mittemeijer, and A. B. P. Vogels, J. Appl. Crystallogr. **15,** 308 (1982).

[23] Y. T. Akitaka Yoshigoe, Jpn. J. Appl. Phys. **49,** 115704 (2010).

[24] A. D. Krawitz, *Introduction to diffraction in materials science and engineering* (Wiley, New York, 2001).

[25] R. Delhez and E. J. Mittemeijer, J. Appl. Crystallogr. **8,** 609 (1975).

[26] L. P. H. Jeurgens, W. G. Sloof, C. G. Borsboom, F. D. Tichelaar, and E. J. Mittemeijer, Appl. Surf. Sci. **161,** 139 (2000).

[27] C. V. Thompson, Annu. Rev. Mater. Sci. **30,** 159 (2000).

[28] Due to the possible presence of stacking faults and twins, the average grain size (as determined by the single line analysis) has to be considered as a lower limit.

[29] M. S. Vinodh and L. P. H. Jeurgens, Surf. Inter. Anal. **36,** 1629 (2004).

[30] C. S. Fadley, Prog. Surf. Sci. **16,** 275 (1984).

[31] R. Olesinski and G. Abbaschian, J. Phase Equilib. **9,** 58 (1988).

[32] R. Dannenberg, E. Stach, J. R. Groza, and B. J. Dresser, Thin Solid Films **379,** 133 (2000).

[33] R. C. Cammarata, Prog. Surf. Sci. **46,** 1 (1994).

[34] R. Abermann, R. Kramer, and J. Mäser, Thin Solid Films **52,** 215 (1978).

Chapter 3

Quantum confinement drives macroscopic stress oscillations at the initial stage of thin film growth

David Flötotto, Zumin Wang, Lars P. H. Jeurgens, and Eric J. Mittemeijer

Abstract

Functionalization of thin-film heterostructures on the basis of their electrical, optical and magnetic properties, requires precise control of the film stresses that develop during the growth process. By using real-time *in situ* stress measurements, the present study reveals strikingly that the in-plane film stress *oscillates* with increasing film thickness at the initial stage of epitaxial Al(111) film growth on a Si(111)-$\sqrt{3} \times \sqrt{3}$-Al surface, with a periodicity of two times the Fermi wavelength of bulk Al and a stress variation from maximum to minimum as large as 100 MPa. Such macroscopic stress oscillations are shown to be caused by quantum confinement of the free electrons in the ultrathin epitaxial metal film. The amplitude, period and phase of the observed stress oscillations are consistent with predictions based on the free electron model and continuum elasticity.

3.1 Introduction

Epitaxial growth enables the construction of heterostructures of different materials, such as metals, semiconductors and ceramics, with atomic precision [1,2]. Such heterostructures have been the origin of a number of fascinating discoveries in fundamental science (such as the quantum Hall effect in semiconductor heterostructures and the giant magnetoresistance effect in metal heterostructures), and are nowadays widely applied in human life [3,4]. It has long been recognized that a considerable strain/stress can build up during epitaxial growth of heterostructures, as induced by lattice mismatch [5]. The magnitude of the associated growth stress is determined by the difference in the equilibrium lattice spacings of the film and the substrate. Upon increasing the film thickness, the growth stress may partially relax by the formation of misfit dislocations at the heterointerface [6], or by morphological transitions [7,8]. A fundamental understanding of the mechanisms for the generation and relaxation of epitaxial stresses is of vital importance for the controlled reduction of stress-induced defects such as dislocations in heterostructure devices. Furthermore, on this basis a well-controllable strain/stress state can also be induced on purpose to tailor the electronic and optical properties of epitaxial heterostructures [9,10].

In this work it is shown that, surprisingly, the in-plane film stress at the initial stage of (epitaxial) metal film growth oscillates with increasing film thickness, with an amplitude as large as hundreds of MPa. Such macroscopic stress oscillations are shown to be driven by the quantum confinement of electrons in the (epitaxial) metal films. This quantum-confinement stress contribution, which has hitherto not been recognized, can play a crucial role in state-of-the-art quantum devices, which, in particular, rely on ultrathin heterostructures. The here discovered direct link between quantum confinement and a macroscopic mechanical property (residual stress) may in particular enable the design of novel-concept quantum sensors using mechanical responses.

3.2 Experimental

The experiments were carried out in a multi-chamber ultrahigh vacuum (UHV) system (base pressure < $1\text{x}10^{-8}$ Pa) for thin film deposition by thermal evaporation and in-vacuo scanning tunneling microscopy (STM). A Si(111)-$\sqrt{3} \times \sqrt{3}$-Al surface was prepared by thermal evaporation of 0.19 monolayer (ML) Al (in this study 1 ML refers to the atomic density of the Al(111) plane at room temperature, i.e. 1 ML = 2.338 Å) at a constant substrate temperature of 700°C onto a 100-μm thin Si(111) wafer. The Si substrate, which was loosely mounted in the sample holder, had been thoroughly cleaned by a programmed laser heat treatment up to a maximum temperature of 1100°C for 1 min in UHV. On the thus prepared surface subsequent Al deposition was performed at room temperature. Initially additional 3.7 MLs Al were deposited with a deposition rate of 0.29 ML/min before resuming the Al film growth with a deposition rate of 4.5 ± 0.1 ML/min until a film thickness of 70 nm. The deposition rates employed were calibrated from STM images and by application of a Veeco DekTak profilometer by determing the height of the deposited Al film for a number of deposition times. For a face-centered cubic film with (111) surface orientation the in-plane stress is rotationally symmetric [11]. Stoney´s equation [12] was applied to determine the evolution of the thickness-averaged in-plane film stress during deposition from the *in situ* measured substrate curvature as monitored in real time by a multi-optical stress sensor (MOS; k-space Associates) [13]. The error of the product of thickness-averaged in-plane stress and film thickness is ±0.017 GPa·nm. The evolution of the film morphology during Al film growth was investigated by STM as a function of Al film thickness. To this end a set of separate experiments were performed with the same thoroughly cleaned Si(111) wafers as used for the stress measurements but with the substrate fixed in the sample holder. The respective Al deposition steps were carried out with the same deposition rates as used during the wafer curvature measurement.

The texture and the orientation relationship with the Si(111) substrate of the epitaxially grown 70 nm thick Al film were investigated through *ex situ* XRD φ-scans and pole figure measurements. The measurements were carried out in a D8 Discover diffractometer in parallel acquisition mode using Cu $K\alpha$ radiation.

A Cross-section TEM foil of the Al(111)/Si(111) specimen was prepared by firstly pre-thinning the specimen by a tripod polisher to a thickness of about 10 μm and secondly by ion milling under liquid-nitrogen cooling in a Precision Ion Polisher 691 operating at an accelerating voltage of 2 keV. Subsequently, the atomic constitution at the interface was investigated by a JEOL 4000FX electron microscope operating at an acceleration voltage of 400 kV.

3.3 Results and discussion

Epitaxial Al film growth on the Si(111)-$\sqrt{3} \times \sqrt{3}$-Al surface takes place by the initial nucleation of monolayer thick Al(111) islands which grow laterally until they coalesce and eventually form a continuous, atomically smooth film (see Fig. 3.1 a-c; cf. Ref. [14,15]). Upon further Al deposition, flat terraces of single atomic layers are observed, demonstrating that epitaxial Al film growth proceeds in a step-flow mode (see Fig. 3.1 d-h; cf. Refs. [15,16]). The observed step-flow type of growth results in the formation of a single crystalline Al(111) film with an orientation relationship with the substrate described by Al(111)||Si(111) and Al[110]||Si[110] (see Fig. 3.2). The Al/Si interface is atomically sharp (see Fig. 3.3).

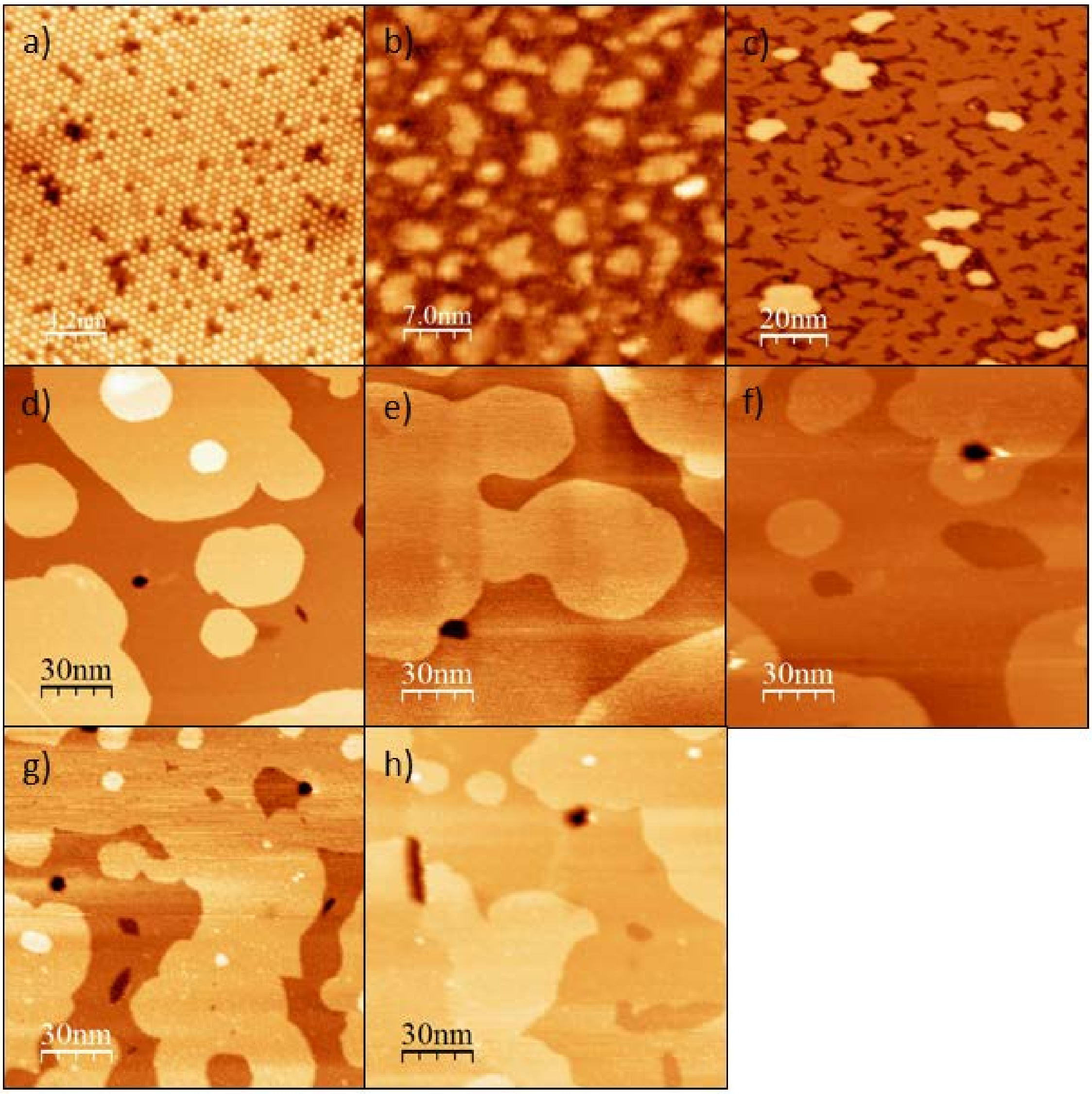

Fig. 3.1. STM images showing the morphological evolution upon Al growth on a Si(111)-$\sqrt{3} \times \sqrt{3}$-Al surface (specimen bias voltage V_t = 1.8 V, tunneling current I_t = 0.3 nA). **(a)** Initial Si(111)-$\sqrt{3} \times \sqrt{3}$-Al reconstructed surface formed by deposition of 0.19 monolayer (ML, 1 ML = 2.338 Å) onto a clean Si(111) surface at 700°C. **(b)** Upon deposition of 0.49 ML Al on the Si(111)-$\sqrt{3} \times \sqrt{3}$-Al surface, monolayer thick Al(111) islands nucleate. **(c)** Upon further Al deposition (cumulative thickness of 0.95 ML), the monolayer thick Al(111) islands grow two-dimensionally and consequently form an almost continuous film, on top of which a second monolayer starts to grow. [**(d)**-**(h)**] Al film growth proceeds in a step-flow type of growth as revealed from the images taken at nominal thicknesses of (d) 6 ML, (e) 7 ML, (f) 7.5 ML, (g) 9 ML and (h) 11 ML.

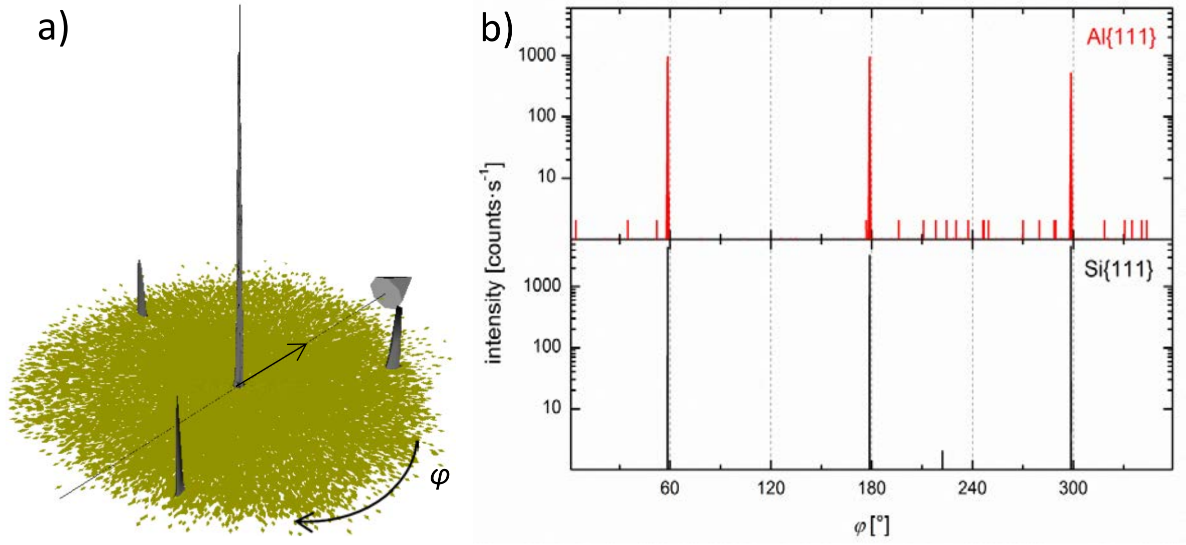

Fig. 3.2. (a) The XRD {111} pole figure of Al reveals that the deposition of Al on a Si(111)-$\sqrt{3} \times \sqrt{3}$-Al surface results in the formation of a single crystalline Al(111) film. **(b)** XRD φ-scans at 2Θ = 38.4° and ψ = 70.53° show that the Al film possesses an orientation relationship with the Si substrate according to Al(111)||Si(111) and Al[110]||Si[110].

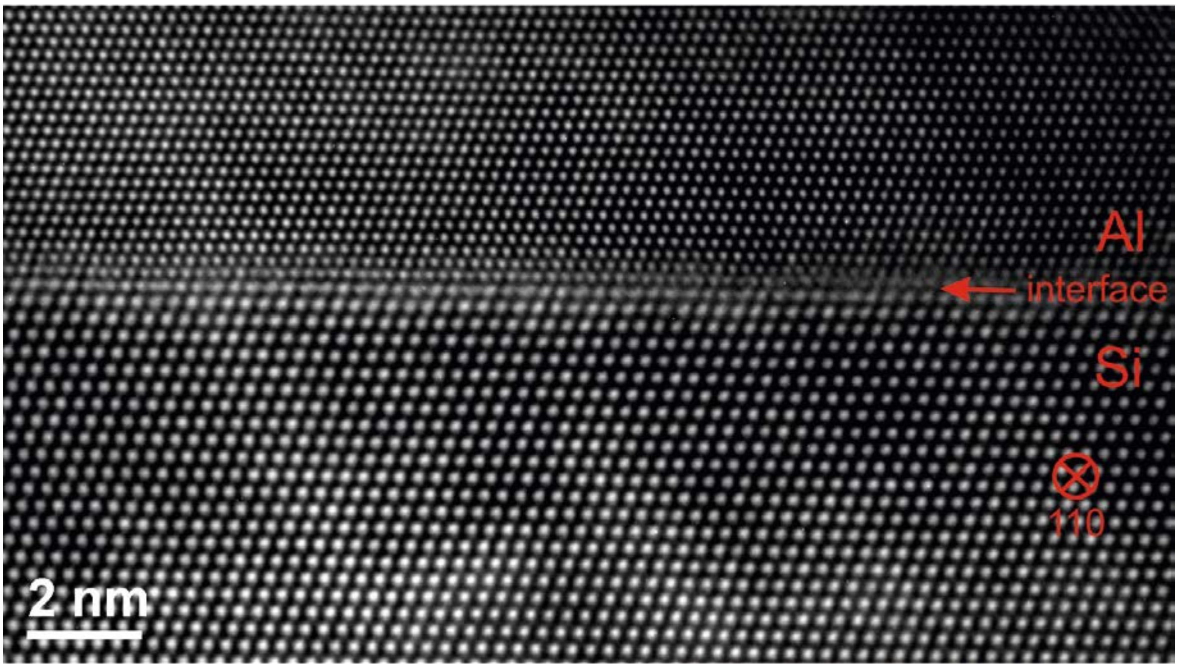

Fig. 3.3. HRTEM image of the Al/Si interface revealing that the interface is atomically sharp.

The measured evolution of the average in-plane film stress during epitaxial Al(111) film growth in a thickness range between 5 and 30 ML is shown in Fig. 3.4a. The observed average in-plane film stress is compressive and oscillates between -225 MPa and -125 MPa during continued epitaxial Al film growth. The amplitude of the stress oscillation becomes attenuated with increasing film thickness. The periodicity of the stress oscillation is about 7.2 Å (3.1 ML), i.e. rather accurately two times the bulk Fermi wavelength of Al (2x3.6 Å).

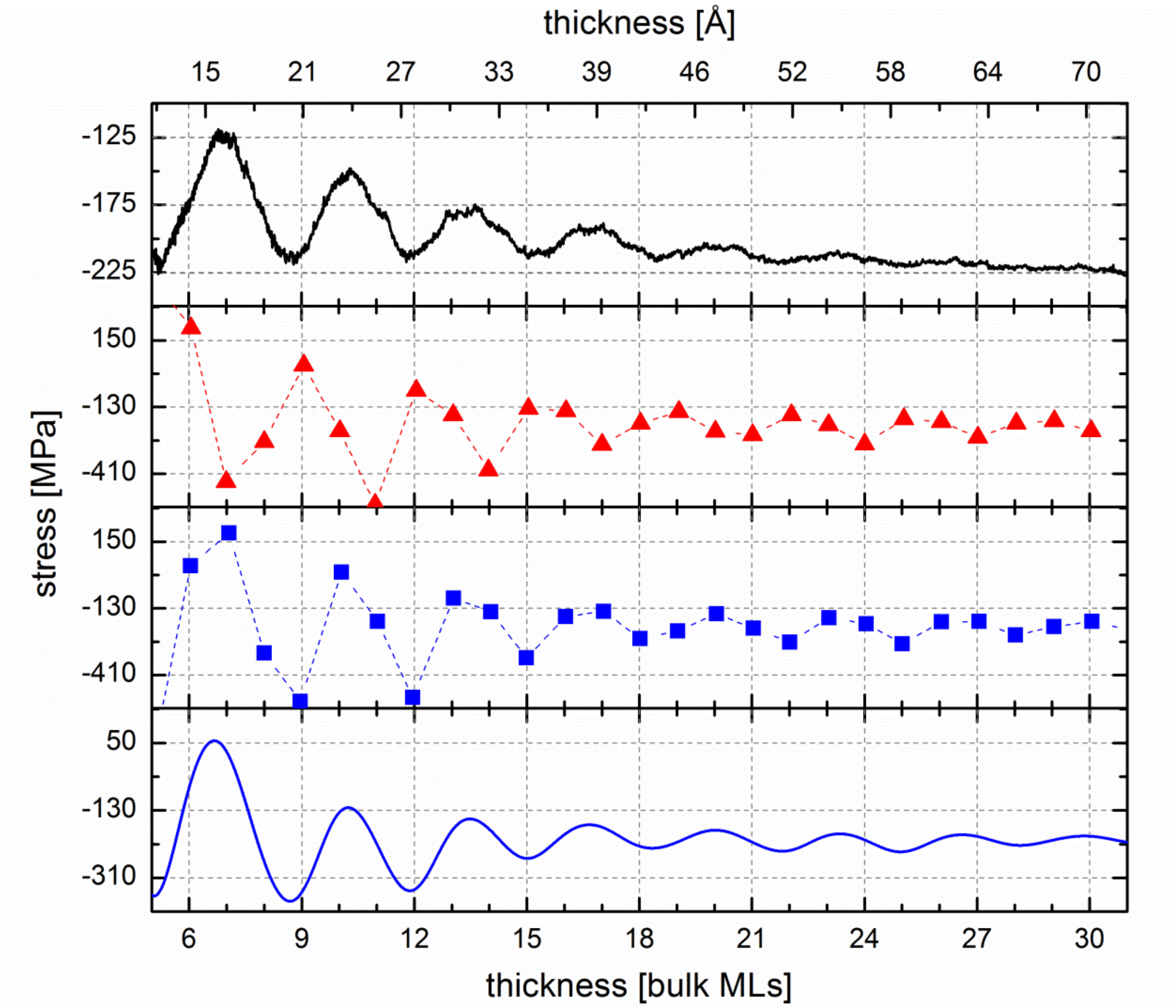

Fig. 3.4. (a) Measured evolution of the average in-plane film stress, as function of the film thickness, during epitaxial growth of an Al(111) film on a Si(111)-$\sqrt{3} \times \sqrt{3}$-Al surface. (b) Calculated (according to the recipe shown in Fig. 3.5 and discussed in the text) average in-plane stress for an Al(111) film of uniform thickness of an integer number of atomic layers, possessing (additionally, as compared to the case considered in Fig. 3.5b) an in-plane growth strain of $\epsilon_{//} = \epsilon_{11} = \epsilon_{22} = -0.0016$. (c) Calculated average in-plane stress, incorporating (additionally to the case considered in (b)) a "phase" (lateral) shift of -0.63 Å (0.27 ML) in $E_{\mathrm{QSE}}(h)$ for an Al(111) film of uniform thickness of an integer number of atomic layers. (d) Calculated average in-plane stress for an Al(111) film incorporating (additionally to the case considered in (c)) the thickness distribution.

The observed step-flow type of growth of the Al film (see above) excludes any morphology effect [17] as the origin of the observed pronounced stress oscillations. As demonstrated in the following, the observed in-plane stress oscillation can be caused by the periodic expansion/contraction of the film, upon overall increasing film thickness, in the direction perpendicular to the film surface, which effect is ascribed to the quantum size effect (QSE) [18,19] (see Fig. 3.5). The spatial confinement of electrons in thin metal films results in oscillations of the free electron energy as function of film thickness, with corresponding energy minima occurring at half Fermi wavelength (λ_F) intervals [20]. Therefore the electron energy favors films with thicknesses separated by an integer number of $\lambda_\mathrm{F}/2$ and forces thin films with thicknesses of different value to expand/contract perpendicular to the surface. This expansion/contraction is constrained because it is associated with the development of elastic strain energy. As a result of the minimization of the sum of electron energy and strain energy, for a free standing film a geometry emerges with a favored thickness and consequently also preferred lateral dimensions (elastic deformation in the in-plane directions). However, because the lateral dimensions of a thin film attached on a rigid substrate are constrained by the (rigid) substrate, in that case the preferred lateral dimensions cannot be realized and consequently stress components are induced in the plane of the film. The alternation of expansion and contraction of the film thickness upon film growth thus leads to oscillating stress components in the plane of the film.

The recipe to calculate the stress component induced by the quantum confinement of the electrons is introduced next.

For a given integer number n of atomic layers film thickness, the instantaneous occurring, equilibrium film thickness, $h_{\mathrm{eq},n}$, is determined by the minimum of the sum of the strain energy per unit film-surface area, $E_\mathrm{strain}(h)$, and the excess free electron energy per unit film-surface area due to quantum confinement of the free electrons, $E_\mathrm{QSE}(h)$.

$E_\mathrm{QSE}(h)$ as function of film thickness h can in principle be calculated using the free electron model for a *freestanding unstrained* Al(111) film with symmetric, finite energy barriers under the constraint of charge-neutrality requirement (i.e. the negative charge outside the geometrical surfaces equals the electronic charge

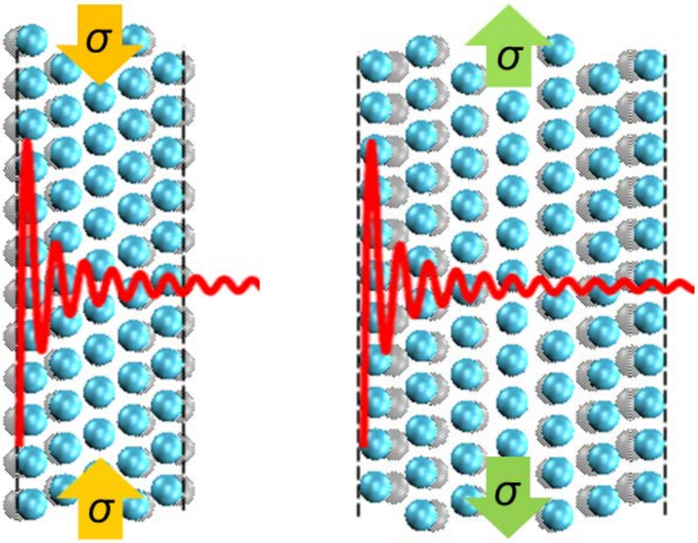

Fig. 3.5. Schematical sketch showing how the quantum size effect can induce a mechanical stress: Due to the osccillating excess free electron energy (red) and the attempt of thin film systems to minimize its energy, the Al-film is forced to contract/expand perpendicular to its surface. However, the lateral film dimensions are constrained by the rigid substrate and thus the contraction/expansion of the film thickness is accompanied with the development of a compressive or tensile in-plane film stress.

missing inside the geometrical surfaces; see Ref. 18 and references therein) according to:

$$E_{\mathrm{QSE}}(h) = E_{\mathrm{film}}(h) - E_{\mathrm{bulk}} \cdot h - 2\gamma^{s} \qquad (3.1)$$

where E_{film} is the film energy per unit area, E_{bulk} is the energy per unit volume of the corresponding bulk material and γ^{s} is the surface energy. The value of $2\gamma^{s}$ is given by $[E_{\mathrm{film}}(h) - E_{\mathrm{bulk}} \cdot h]_{h\to\infty}$ and thus $E_{\mathrm{QSE}}(h) = 0$ for $h \to \infty$. Using the methodology of Ref. [20], actually E_{QSE} is calculated as function of h, i.e. not for a fixed number of monolayers but for a continuously thickening film (by adding atoms/electrons). The result is shown by the green, dotted curve in Fig. 3.6a. Evidently, the calculated E_{QSE} as a function of thickness h resembles a damped sinus function with a periodicity of $\lambda_{\mathrm{F}}/2$. It is supposed that this curve *around the thickness values corresponding to integral numbers of monolayers* provides a realistic estimation for the variations of E_{QSE} as function of h for films composed of such integer numbers of monolayers (solid green curves in Fig. 3.6a).

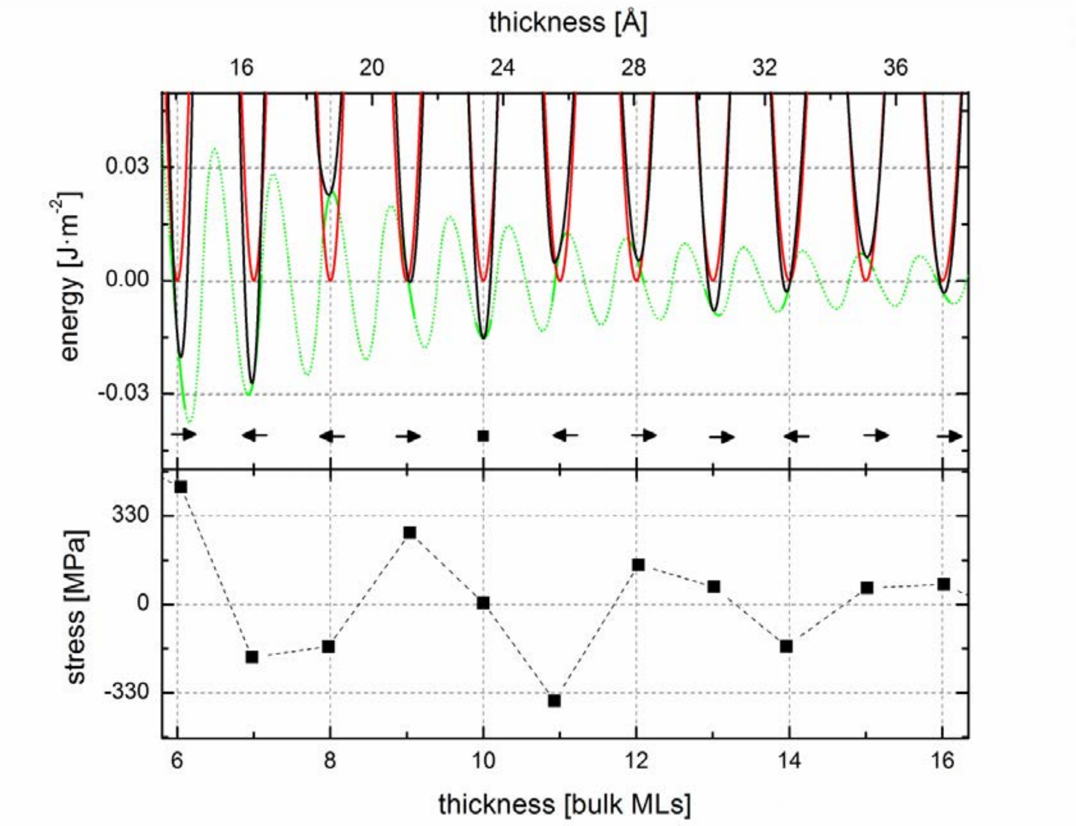

Fig. 3.6. **(a)** The excess electron energy per unit film-surface area due to the quantum confinement of electrons as a function of film thickness (green curve) and the strain energy per unit film-surface area for an uniform film of integer number of atomic layers as function of film thickness (red curves). The minima of the sum curves (black curves = green curve + red curves) determine the instantaneous occurring equilibrium film thickness values for films of integer numbers of atomic layers. The arrows schematically indicate the thickness changes of the films (of integer number of atomic layers) with respect to their h_0 values. **(b)** The calculated in-plane stress, $\sigma_{//}$, oscillates between tensile and compressive states with overall increasing film thickness.

In the absence of a state of stress, a uniform, thin Al(111) film has a thickness $h_0 = n \cdot d^{\infty}_{\mathrm{Al}(111)}$, where $d^{\infty}_{\mathrm{Al}(111)}$ represents the bulk Al(111) interlayer spacing. For the film strained in in-plane and out-of-plane directions (see above discussion), the associated strain energy is given by:

$$E_{\mathrm{strain}}(h) = C_{ijkl} \cdot \epsilon_{ij} \cdot \epsilon_{kl} \cdot n \cdot d^{\infty}_{\mathrm{Al}(111)} \qquad (3.2)$$

where C_{ijkl} is the fourth-rank stiffness tensor as defined in the specimen coordinate system and ϵ_{ij} is the strain tensor in the specimen coordinate system. The strain components in this equation are defined with respect to bulk material not subjected to quantum confinement and (lateral) constraints.

For an Al(111) film all shear components of the strain tensors, $\epsilon_{i\neq j}$, are zero and the out-of-plane strain component, ϵ_{33}, is determined by

$$\epsilon_{33} = \left(h - n \cdot d^{\infty}_{\mathrm{Al(111)}}\right) / \left(n \cdot d^{\infty}_{\mathrm{Al(111)}}\right). \tag{3.3}$$

In the absence of other source of stress/strain, $\epsilon_{11} = \epsilon_{22} = 0$. Using the values of ϵ_{ij} as indicated, E_{strain} can be calculated as function of h for a film of an integer number of atomic layers; see the red curves in Fig. 3.6a. The summations of the individual curves of $E_{\mathrm{QSE}}(h)$ and $E_{\mathrm{strain}}(h)$ are given by the black curves in Fig. 3.6a. The minima of these curves then predict the actual, equilibrium thicknesses, $h_{\mathrm{eq},n}$, for films of given integer numbers of atomic layers. The arrows in the figure schematically indicate the thickness changes of the films with respect to the h_0 (see above) values. Using the thus determined values of $h_{\mathrm{eq},n}$, $\epsilon_{33}(h_{\mathrm{eq},n})$ can be calculated from Equation (3). Next, the (rotationally symmetric) in-plane stress components ($\sigma_{//} = \sigma_{11} = \sigma_{22}$) can be determined from Hooke's law, $\sigma_{ij} = C_{ijkl} \cdot \epsilon_{kl}$, leading to

$$\sigma_{//} = \sigma_{11} = \sigma_{22} = C_{1133}\epsilon_{33} \tag{3.4}$$

The resulting values of $\sigma_{//}$ are shown in Fig. 3.6b for increasing film thickness by data points at $h_{\mathrm{eq},n}$. The calculation indeed predicts a damped stress oscillation pattern with overall increasing film thickness. The amplitude of the stress oscillations attenuates with increasing thickness as a consequence of the decrease of the quantum size effect with increasing film thickness. The resulting periodicity of the stress oscillation pattern is a consequence of the interaction of the $d^{\infty}_{\mathrm{Al(111)}}$ periodic minima in $E_{\mathrm{strain}}(h)$ and the $\lambda_{\mathrm{F}}/2$ periodic minima in $E_{\mathrm{QSE}}(h)$. For a Al(111) film the ratio of $\lambda_{\mathrm{F}}/2$ and $d^{\infty}_{\mathrm{Al(111)}}$ is ≈ 4:3, which results in a stress oscillation pattern with a periodicity of ≈ $2\lambda_{\mathrm{F}}$ = 7.2 Å (3.1 ML), as experimentally observed.

In order to allow comparison of such a prediction of $\sigma_{//}$ oscillation with experimental results, some practical complications have to be taken into account:

(i) At (large) thickness values, where the quantum size effect can be ignored, the observed in-plane strain is not equal to zero. For the epitaxial Al film in this study, this in-plane growth strain, $\epsilon_{//} = \epsilon_{11} = \epsilon_{22}$, equals -0.0016, as observed at film thicknesses beyond 30 ML (cf. Fig. 3.4a). Therefore, in the above sketched calculations, $\epsilon_{//} = 0$ has to be substituted by $\epsilon_{//} = \epsilon_{11} = \epsilon_{22} = -0.0016$. As a result of the accordingly repeated calculation (now using a corresponding modified Eq. 4: $\sigma_{//} = \sigma_{11} = \sigma_{22} = C_{1111}\epsilon_{11} + C_{1122}\epsilon_{22} + C_{1133}\epsilon_{33}$) the overall stress level in the film changes such that the in-plane stress component oscillates around a value of ≈ -220 MPa, instead of around $\sigma_{//} = 0$ (see Fig. 3.4b and compare with Fig. 3.6b).

(ii) The "phase" of the stress oscillation pattern strongly depends on the "phase" of $E_{\mathrm{QSE}}(h)$. Although the periodicity of the oscillation pattern of $E_{\mathrm{QSE}}(h)$ is independent of the used (free) electron model [20,21], the phase of the oscillation pattern of $E_{\mathrm{QSE}}(h)$ distinctly depends on the heights of energy barriers at the substrate/film and film/vacuum interfaces as well as on the lattice potential. Therefore, the present calculation, which is based on the free electron model for a free standing film with equal energy barriers at both film faces, cannot predict exactly the phase of the oscillation pattern of $E_{\mathrm{QSE}}(h)$ [21]. By incorporating a phase (lateral) shift of -0.63 Å (0.27 ML) in $E_{\mathrm{QSE}}(h)$ and then repeating the above sketched calculations, the maxima and minima of the calculated stress oscillation pattern become in perfect agreement with the experimental result (cf. Fig.3.4a and Fig 3.4c).

(iii) It is recognized that the epitaxially growing Al(111) film exhibits a thickness distribution (see Fig. 3.7). To consider the effect of the thickness distribution on the average in-plane stress, (a) the percentages of the total film-surface area covered by a film of n atomic layers, p_n, as determined from the STM image at a nominal film thickness of 10 nm, are described by a Gaussian distribution, and (b) it is assumed that the thickness distribution is independent of film thickness (i.e. at all mean film thicknesses the same Gaussian distribution prevails). Then the average in-plane stress $\langle\sigma_{//}\rangle$ at mean film thickness $\langle h\rangle = \sum_{n=1}^{\infty} p_n \cdot h_{\mathrm{eq},n}$ is given by

$$\langle\sigma_{//}\rangle = {}^{1}\!/_{\langle h\rangle} \cdot \sum_{n=1}^{\infty} p_n \cdot h_{\mathrm{eq},n} \cdot \sigma_{//,n} \qquad (3.5)$$

The thus calculated curve of average in-plane stress, $\langle\sigma_{//}\rangle$ (i.e. incorporating the effects discussed under (i), (ii) and (iii) above), as function of epitaxial Al(111) film thickness is shown in Fig. 3.4d (note that, because of the effect (iii), this curve now is continuous). The calculated curve agrees excellently with the measured curve for the average in-plane film stress in terms of the periodicity and the damping behavior (cf. Fig. 3.4a and Fig. 3.4d). The amplitude of the measured stress oscillation is smaller than that of the calculated stress oscillation. This difference can be caused by (1) a broader thickness distribution during film growth as compared to the thickness distribution measured after film growth by STM, and/or (2) elastic constants of ultrathin films which differ from their bulk counterparts [22,23].

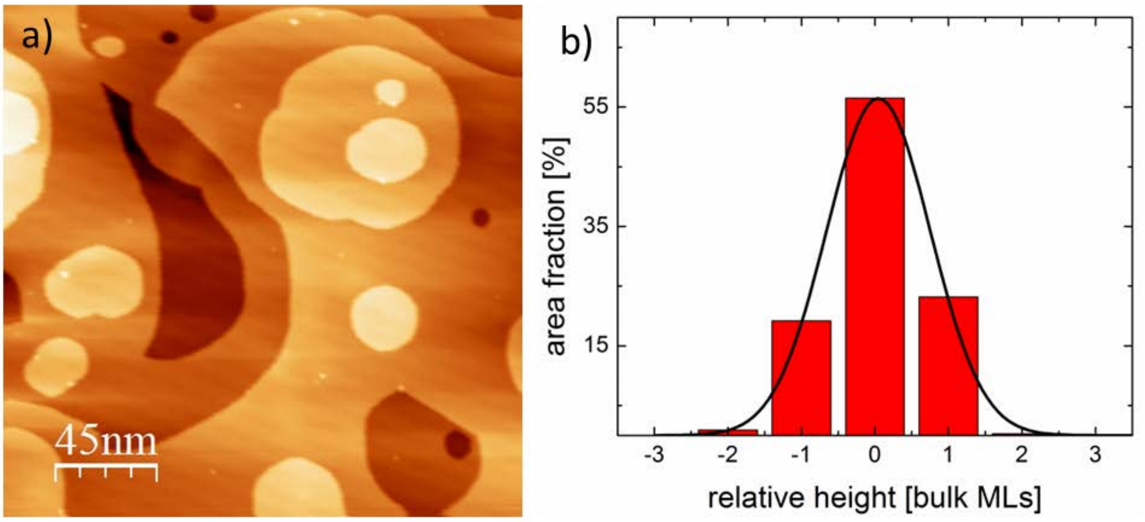

Fig. 3.7. (a) STM image (225 nm x 225nm, specimen bias voltage V_t = 1.4 V, tunneling current I_t = 0.2 nA) and **(b)** the corresponding height distribution, after deposition of a nominally 10 nm epitaxial Al film on a Si(111)-$\sqrt{3} \times \sqrt{3}$-Al surface.

3.4 Conclusion

In conclusion, macroscopic stress oscillations as large as 100 MPa are observed during the initial stage of epitaxial Al(111) film growth on a Si(111)-$\sqrt{3} \times \sqrt{3}$-Al surface. The stress oscillations are induced by the quantum confinement of electrons in the thin epitaxial metal film. The amplitude, period and phase of the observed macroscopic stress oscillations are consistent with predictions based on the free electron model and continuum elasticity. The here discovered direct link between quantum confinement and macroscopic film stress can play a crucial role for the design of novel-concept functional ultrathin heterostructures.

Acknowledgement

The authors are grateful to S. Haag for the invaluable discussions, to U. Salzberger for the preparation of the TEM foils, and to Dr. F. Phillipp and Prof. L. Gu for the HRTEM investigation.

References

[1] W. P. McCray, Nat. Nanotechnol. **2,** 259 (2007).

[2] J. Mannhart and D. G. Schlom, Science **327,** 1607 (2010).

[3] Z. I. Alferov, Rev. Mod. Phys. **73,** 767 (2001).

[4] H. Kroemer, Rev. Mod. Phys. **73,** 783 (2001).

[5] F. C. Frank and J. H. van der Merwe, Proc. R. Soc. A **198,** 216 (1949).

[6] E. A. Fitzgerald, Mater. Sci. Rep. **7,** 87 (1991).

[7] J. A. Floro, E. Chason, R. D. Twesten, R. Q. Hwang, and L. B. Freund, Phys. Rev. Lett. **79,** 3946 (1997).

[8] G. Medeiros-Ribeiro, A. M. Bratkovski, T. I. Kamins, D. A. A. Ohlberg, and R. S. Williams, Science **279,** 353 (1998).

[9] R. S. Jacobsen, K. N. Andersen, P. I. Borel, J. Fage-Pedersen, L. H. Frandsen, O. Hansen, M. Kristensen, A. V. Lavrinenko, G. Moulin, H. Ou, C. Peucheret, B. Zsigri, and A. Bjarklev, Nature **441,** 199 (2006).

[10] A. M. Smith, A. M. Mohs, and S. Nie, Nat. Nanotechnol. **4,** 56 (2009).

[11] L. B. Freund and S. Suresh, *Thin Film Materials: Stress, Defect Formation, and Surface Evolution* (Cambridge University Press, Cambridge, 2003).

[12] G. G. Stoney, Proc. R. Soc. A **82,** 172 (1909).

[13] E. Chason and B. W. Sheldon, Surf. Eng. **19,** 387 (2003).

[14] J. Teng, L. Zhang, Y. Jiang, J. Guo, Q. Guo, E. Wang, P. Ebert, T. Sakurai, and K. Wu, The Journal of Chemical Physics **133,** 014704 (2010).

[15] A. Uemura, A. Ohkita, H. Inaba, S. Hasegawa, and H. Nakashima, Surface Science **357-358,** 825 (1996).

[16] Y. Horio, Jpn. J. Appl. Phys. Part 1 - Regul. Pap. Short Notes Rev. Pap. **38,** 4881 (1999).

[17] D. Sander, S. Ouazi, V. S. Stepanyuk, D. I. Bazhanov, and J. Kirschner, Surface Science **512,** 281 (2002).

[18] Z. Zhang, Q. Niu, and C.-K. Shih, Phys. Rev. Lett. **80,** 5381 (1998).

[19] M. C. Tringides, M. Jałochowski, and E. Bauer, Phys. Today **60** (2007).

[20] Y. Han and D.-J. Liu, Phys. Rev. B **80,** 155404 (2009).

[21] B. Wu and Z. Zhang, Phys. Rev. B **77,** 035410 (2008).

[22] J.-G. Guo and Y.-P. Zhao, J. Appl. Phys. **98,** 074306 (2005).

[23] F. H. Streitz, R. C. Cammarata, and K. Sieradzki, Phys. Rev. B **49,** 10699 (1994).

Chapter 4

Evolution of surface stress during oxygen exposure of clean Si(111), Si(100) and amorphous Si surfaces

D. Flötotto, Z. M. Wang, L. P. H. Jeurgens and E. J. Mittemeijer

Abstract

The evolutions of the surface stress of Si(111)-7x7, Si(100)-2x1 and a-Si surfaces upon oxygen exposure at $p\mathrm{O}_2 = 1\times10^{-4}$ Pa and room temperature have been investigated in a comparative manner using a specimen-curvature based technique. To this end, a generally applicable, dedicated set of experiments has been devised and performed to deduce and correct for the surface stress change owing to oxygen reaction(s) at the (poorly-defined) back face of the specimen only. On this basis it could be demonstrated that exposure of clean Si(111)-7x7, Si(100)-2x1 and a-Si surfaces to pure oxygen gas results in compressive surface stress changes for all three surfaces due to the incorporation of oxygen into Si backbonds. The measured surface stress change decreases with decreasing atomic packing density at the clean Si surfaces, which complies well with the less-densily packed Si surface regions containing more free volume for the accommodation of adsorbed O atoms.

4.1 Introduction

The lack of bonding partners at a free solid surface results in a significant redistribution of the electronic charge density within the (sub)surface region, and correspondingly, a modification of the (strived for) equilibrium interatomic distances at the (sub)surface as compared to those in the bulk. As a consequence, the forces then experienced by the surface atoms to assure their registry with the bulk lattice give rise to a surface stress [1]. Evidently, surface stresses play a dominant role in many surface-related phenomena, such as surface reconstructions [2], surface diffusion and surface morphological transitions [3]. Surface stresses can even influence the development of “bulk” intrinsic stresses in thin films during growth [4,5].

Adsorption of foreign species on a solid surface modifies the local chemical environment at the surface, which typically results in a change of the surface stress [6]. Such adsorption-induced surface stress changes are nowadays employed in e.g. nano-mechanical sensing applications [7-9]. Most studies of adsorbate-induced surface stress change have been conducted by measuring the change in specimen curvature [10-14].

Consider a thin metal, semiconductor or alloy specimen which is mounted in a sample holder such that it is free to bend. Exposure of the clean specimen surfaces to oxygen gas gives rise to the simultaneous reaction of oxygen (i.e. physisorption, chemisorption and/or oxide formation) with the front face *and* the back face of the parent specimen. The *difference* of the resulting O-exposure-induced surface stress changes at the front face and the back face of the parent specimen leads to a measurable change of the specimen curvature as a function of the oxygen-exposure time. Evidently, the magnitude of the surface stress changes at one face (e.g. the front face) of the specimen can be determined from such experiments only if either (*i*) the O-exposure-induced stress change at the opposite face (e.g. the back face) of the specimen can either be totally neglected (i.e. the specimen back face is fully inert to the oxygen exposure treatment) or (*ii*) the measurement can be corrected for the “back face effect”.

The front face specimen surface should be well-defined and free of contaminants at the onset of the experiment, which can only be realized by careful preparation of the specimen surface under ultrahigh vacuum (UHV) conditions. Conventional sputter-cleaning of the specimen surface by noble gas ion bombardment is often applied but this method creates a high density of surface defects, which not only alters the surface stress [15], but also enhances the surface reactivity upon subsequent oxygen exposure. Hence, then a post-annealing treatment of the sputter-cleaned specimen under UHV conditions is generally required to restore the crystallinity of the ion-bombarded surface. However, such a post-annealing treatment may destroy the desired (see above) chemical inertness of the back face surface upon oxygen exposure e.g. by partial or complete removal of the (native) oxide layer on the non-sputtered back face specimen surface.

In this work, a general applicable, dedicated set of experiments has been designed and performed, which allows resolving the “back face effect”, i.e. the surface stress change due to the undesired but unavoidable (see above) oxygen reaction(s) at the unpolished rough (poorly-defined) back face of the specimen only. The thus obtained “back face effect” can be used to determine (by subtraction) precisely the surface stress change at the “front face” specimen surface. The developed experimental procedure has been utilized here for a direct determination and comparison of the surface stress evolutions during O-exposure of Si(111)-7x7, Si(100)-2x1 and a-Si surfaces at room temperature and $pO_2 = 1\times10^{-4}$ Pa.

4.2 Experimental

The experiments were carried out in a customized multi-chamber ultrahigh vacuum (UHV) system (base pressure $< 3\text{x}10^{-8}$ Pa) for thin film deposition by thermal evaporation, in-vacuo angle-resolved X-ray photoelectron spectroscopy (AR-XPS) and in-vacuo scanning tunneling microscopy (STM). Square-shaped (13.9x13.9 mm^2), one side polished, 100 µm thin Si(111) and Si(100) wafers were loosely mounted in the specimen holder, introduced into the UHV system and then thoroughly degassed and cleaned by a programmed laser heat treatment up to a maximum temperature of 1100°C for 1 min in UHV. After subsequent cooling to room temperature, STM and XPS measurements revealed contamination-free, well ordered Si(111)-7x7 and Si(100)-1x2 specimen surfaces, respectively. Next, the Si wafer specimens were exposed to pure oxygen gas at $pO_2 = 1\times10^{-4}$ Pa for $t = 1800$ s at room temperature. The adsorption-induced (net) change of surface stress, $\Delta\tau$, (i.e. due to physisorption, chemisorption and/or oxide formation) was determined from the *in situ* measured specimen-curvature change, $\Delta\kappa$, as monitored in real time by a multi-optical stress sensor (MOS; k-space Associates)[16], with a 3 x 3 array of parallel laser beams aligned at normal incidence to the specimen front face. According to Stoney´s equation [17]

$$\Delta\tau = \frac{M_s {h_s}^2}{6}\Delta\kappa \qquad (4.1)$$

where M_S and h_s denote the biaxial modulus and the thickness of the specimen, respectively. The measured (net) specimen-curvature change, $\Delta\kappa$, is given by the sum of the curvature change, $\Delta\kappa_{front\,face}$, resulting from a surface stress change due to the reaction of oxygen at the front face of the specimen and the curvature change, $\Delta\kappa_{back\,face}$, resulting from a surface stress change due to the reaction of oxygen at the back face of the specimen.

In order to determine the contribution to the measured specimen-curvature change owing to the reaction of oxygen with the unpolished (rougher) back face of the specimen only, a set of experiments was designed and performed, as described below.

Step 1 (see Fig. 4.1a): Firstly, a 15 nm thick, amorphous Si film (a-Si) was deposited by thermal evaporation of pure Si (99.999 at%) from a tungsten crucible at room temperature on the Si(111)-7x7 and Si(100)-1x2 reconstructed (front) surfaces of the Si(111) and Si(100) specimens (as obtained according to the preparation procedures described above).

Step 2 (see Fig. 4.1b): The specimens were then exposed to pure oxygen gas at $pO_2 = 1\times10^{-4}$ Pa for t = 1800 s at room temperature, while recording the (net) change of specimen curvature due to the simultaneous reaction of oxygen with both specimen surfaces (i.e. with the clean, a-Si front surface *and* with the clean, unpolished Si back surface).

Step 3 (see Fig. 4.1c): Next, a “fresh” 15 nm thick a-Si film was deposited on the front surfaces of the O-exposed specimens, employing the same growth conditions as in step 1. Noteworthy, for both specimens, the front surface exhibits the same RMS roughness of 2.4 Å after step 1 and after step 3 (as determined by in vacuo STM).

Step 4 (see Fig. 4.1d): Finally, the specimens as obtained after step 3 were exposed for a second time to pure oxygen gas at $pO_2 = 1\times10^{-4}$ Pa for t = 1800 s at room temperature. The back surfaces of the Si(111) and the Si(100) specimens had already been passivated (saturated) during the first O exposure (see step 2) [18]. Hence, the specimen curvature, as measured during step 4, is only due to the reaction of oxygen with the newly deposited a-Si film at the front face surfaces of the specimens.

The amount (coverage) of reacted oxygen on the O-exposed Si(111)-7x7, Si(100)-1x2 and a-Si surfaces (after t = 1800 s; see above) was determined by in-

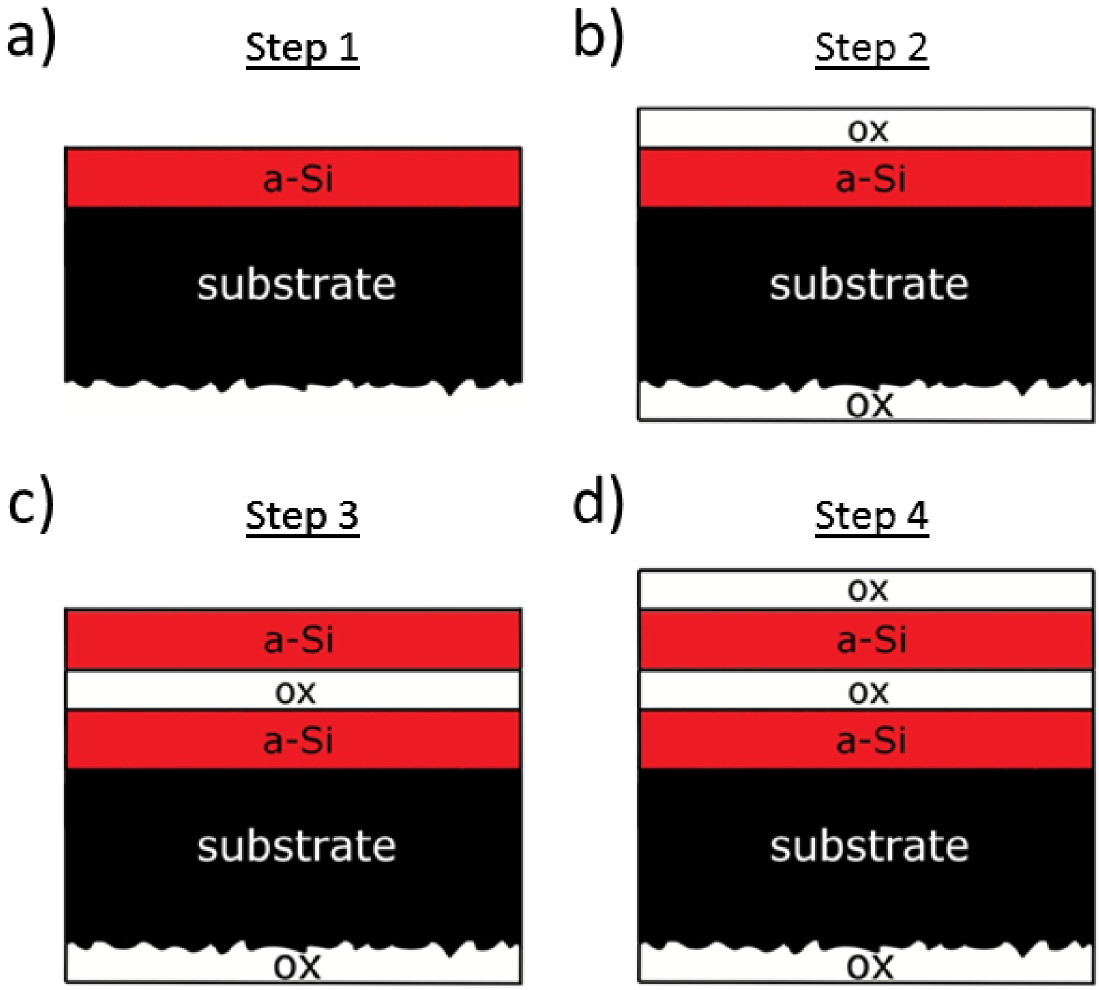

Fig. 4.1 Schematic illustration of the experimental steps for the in situ, accurate determination of the substrate-curvature changes due to adsorption on the rough (unpolished) Si(111) and Si(100) substrate back faces. **(a)** After the preparation (by thorough degassing and heating the specimen up to 1100°C) of a Si(111) or Si(100) substrate with contamination-free front face and back face, an a-Si film is deposited onto the surface front face. **(b)** During subsequent oxygen exposure, oxygen is adsorbed at both the a-Si surface and the rough Si specimen back face. **(c)** Deposition of a second a-Si film on top of the oxidized a-Si surfaces under exactly the same growth conditions as in step (a). **(d)** During a second oxygen exposure, oxygen is only adsorbed at the freshly grown a-Si layer at the specimen front face, whereas no oxygen is adsorbed at the inert, passivated specimen back face, already covered with an oxide layer.

vacuo AR-XPS analysis using a Thermo VG Thetaprobe system employing monochromatic Al-$K\alpha$ radiation. To this end the O 1s and Si 2p core level spectra before and after oxygen exposure were recorded in the so-called parallel data acquisition mode by simultaneously collecting the photoelectrons over the angle detection range α (with respect to the sample surface normal) of 23°-75° in seven ranges of 7.5° each with a step size of 0.1 eV and a constant pass energy of 50 eV [19]. The total O 1s and Si 2p primary zero loss (PZL; see Ref. [20]) intensities were obtained from the integrated area of the Shirley-background-corrected O 1s and Si 2p main peaks. The amount of adsorbed oxygen on the O-exposed Si surfaces was determined from the PZL intensity ratio $I_{\mathrm{O\,1s}}/I_{\mathrm{Si\,2p}}$ by adopting a model for non-attenuating adsorption layer systems which neglects any inelastic scattering in the oxygen overlayer [21]. The values for the inelastic mean free path of the detected Si 2p photoelectrons for crystalline and amorphous Si, as required for the calculation were determined according to Ref. [22] and equal 3.09 nm and 3.15 nm, respectively (taking into account that the density of an a-Si film is only 95% of that of a bulk Si crystal [23]). Furthermore, a constant ratio of the O 1s and Si 2p total photoionization cross-sections of $\sigma_{\mathrm{O\,1s}}/\sigma_{\mathrm{Si\,2p}}$ = 3.21 was used [24].

4.3 Results

4.3.1 Determination of the "back face effect"

The measured curvature changes of the Si(111) and Si(100) specimens during the oxygen exposure steps 2 and 4, as described in Sec. 2 (see also Figs. 4.1b and 4.1d), have been plotted as function of the oxygen exposure time in Fig. 4.2a and Fig. 4.2b, respectively. Oxygen exposure of the Si(111) and Si(100) specimens with clean (unpolished) back faces and freshly-deposited a-Si films at their (polished) front faces (see step 2 in Sec. 4.2 and Fig. 4.1b), resulted in abrupt changes in specimen curvature of 2.7 km^{-1} and 0.9 km^{-1}, respectively (see *black curves* in Fig. 4.2). After these instantaneous *positive* changes in specimen curvature, no further changes in curvature occurred, neither with increasing oxygen exposure, nor after closing the oxygen valve after *t* = 1800 s. Next "fresh" 15 nm thick a-Si films were deposited on the oxidized front surfaces of the Si(111) and Si(100) specimens (see step 3 in Sec. 4.2 and Fig. 4.1c). During subsequent O-exposure of the thus prepared specimens (see step 4 in Sec. 2 and Fig. 4.1d) the specimen-curvature change asymptotically approached *negative* values of -0.8 km^{-1} and -1.2 km^{-1} for the Si(111) and Si(100) specimens, respectively (see *red curves* in Fig. 4.2). These measured curvature changes during the second oxygen exposure correspond to an equivalent change in surface stress of -0.3 N/m for both specimens, which only result from the reaction of

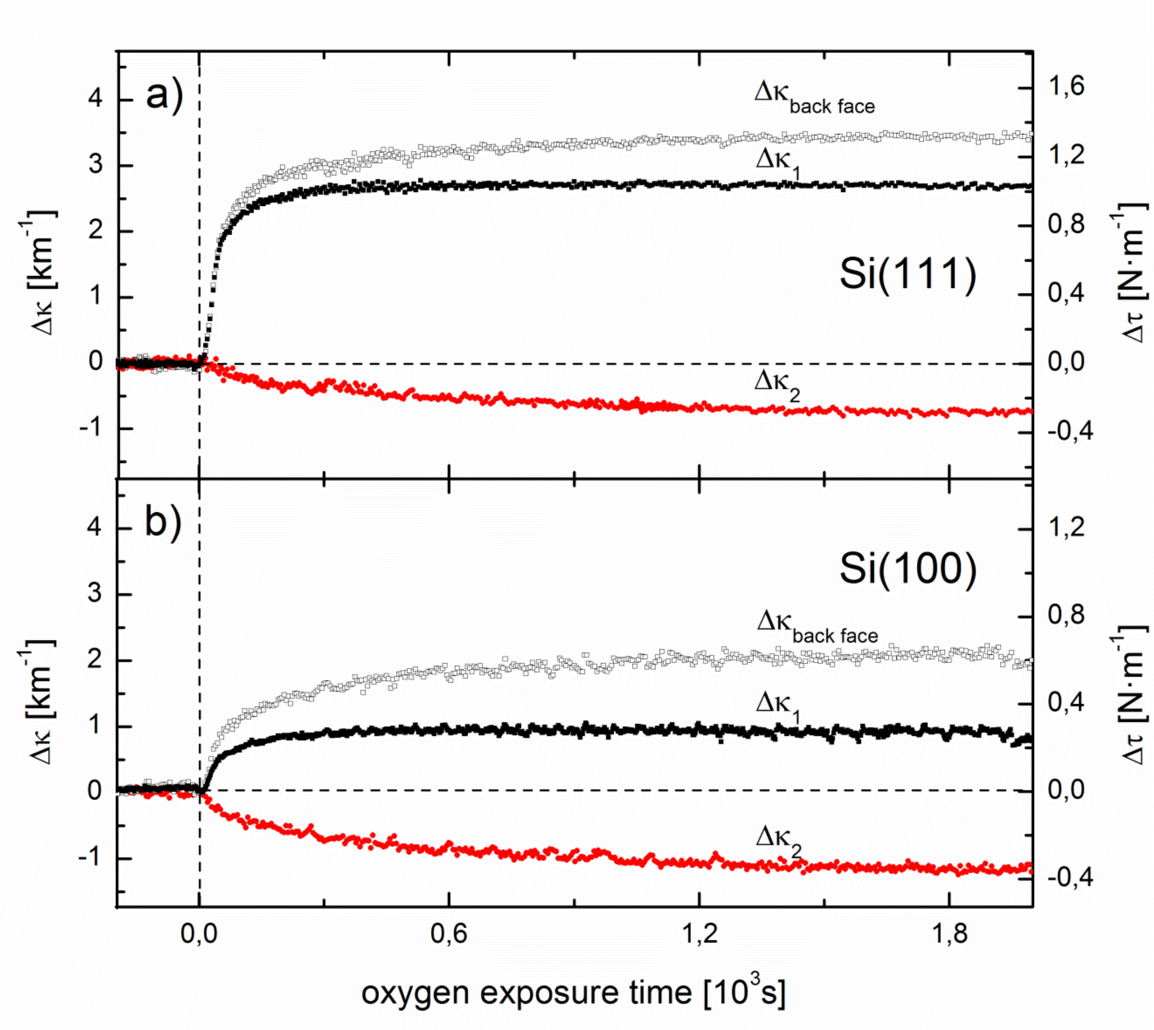

Fig. 4.2. The specimen-curvature changes, $\Delta\kappa$, measured during the, in Fig 4.1 sketched, successively performed oxygen exposure experiments at $p_{O_2} = 10^{-4}$Pa and 300 K **(a)** for Si(111) and **(b)** for Si(100) substrates, respectively. Black, filled squares represent the measured substrate-curvature change, $\Delta\kappa_1$, during the first exposure i.e. due to oxygen adsorption at an a-Si film surface and at the rough Si(111) and Si(100) specimen back faces ("step 2", Fig. 4.1b). Red dots represent the measured substrate-curvature change, $\Delta\kappa_2$, during the second exposure i.e. due to oxygen adsorption at only the a-Si film surface, since at this stage the back face is passivated by the oxide layer formed during the first oxygen exposure step ("step 4", Fig. 4.1d). Finally, subtraction of $\Delta\kappa_2$ from $\Delta\kappa_1$ yields the substrate-curvature change, $\Delta\kappa_{backface}$, due to oxygen adsorption at the rough Si(111)and Si(100) wafer back face only (open squares).

oxygen with the freshly-deposited a-Si film at the front surfaces of the Si(111) and Si(100) specimens, because the back surfaces of both specimens were already passivated with oxygen during the first oxygen exposure (see step 2 in Sec. 4.2 and Fig. 4.1b).

Subtraction of the measured curvature change, $\Delta\kappa_2$, as recorded during the second O exposure (see step 4 in Sec. 4.2 and Fig. 4.1d), from the corresponding curvature change, $\Delta\kappa_1$, as measured during the first O exposure (see step 2 in Sec. 4.2 and Fig. 4.1b) yields the curvature change, $\Delta\kappa_{back\ face}$, due to the reaction of oxygen at the clean (unpolished) back surfaces of the Si(111) and Si(100) specimens only. The thus obtained $\Delta\kappa_{backface}$ curves for the Si(111) and Si(100) specimens can be employed to resolve the surface stress evolutions induced by oxygen exposure of only the Si(111)-7x7, Si(100)-2x1 and a-Si surfaces at $p\mathrm{O}_2 = 1\times10^{-4}$ Pa and at room temperature (see Sec. 4.2), by subtraction of the specimen curvature due to the "back face effect" from the measured curvature change (see what follows).

4.3.2 Evolution of surface stress during oxygen exposure of Si(111)-7x7, Si(100)-2x1 and a-Si surfaces

The surface stress changes upon O exposure of the Si(111)-7x7, Si(100)-2x1 and a-Si surfaces (at T = 300 K and $p\mathrm{O}_2 = 1\times10^{-4}$ Pa), as obtained after correcting for (i.e. subtracting) the back face effect, have been plotted as function of oxygen-exposure time in Fig. 4.3. For the Si(111)-7x7, Si(100)-2x1 and a-Si surfaces oxygen exposure

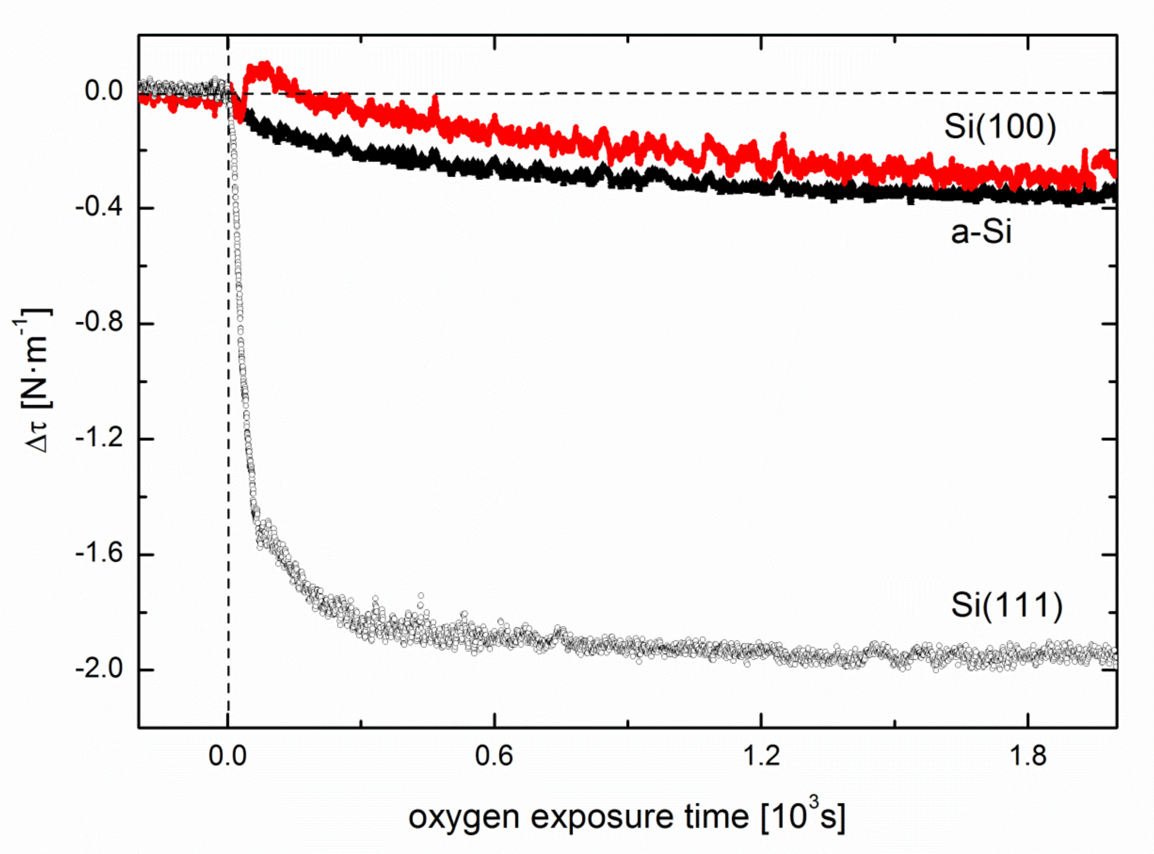

Fig. 4.3. The surface stress change due to oxygen adsorption at only the clean Si(111)-7x7, Si(100)-2x1 and a-Si surfaces at $p_{O_2} = 10^{-4}$Pa and 300 K, i.e. after correcting for the back face effect (cf. Fig. 4.2), as function of oxygen-exposure time.

results in the development of a compressive surface stress of -1.9 N/m, -0.3 N/m and -0.4 N/m after t = 1800 s, respectively. Strikingly, an instantaneous compressive surface stress change occurs at the onset of O exposure for the Si(111)-7x7 and the a-Si surfaces, whereas a relatively minor tensile surface stress change (up to 0.1 N/m after 80 s of oxygen exposure) arises at the onset of O exposure of the Si(100)-2x1 surface, which gradually becomes compressive with increasing O exposure. Due to the fast saturation of O-adsorption sites on the exposed Si surfaces (i.e. the fast passivation of the Si surfaces; see section 3.3 and Ref. [18]), no distinct changes of the developed surface stresses occur upon prolonged oxygen exposure for times t > 1800 s. Furthermore, also after closing the oxygen valve after t = 1800 s no changes of surface stress occur.

4.3.3 Fractional oxygen surface coverage

The surface stress changes of the Si(111)7x7, Si(100)2x1 and a-Si surfaces after O exposure of 1800 s can be related to the fractional oxygen coverage of the then O-passivated Si surfaces (i.e. the ratio of the atomic surface density of adsorbed oxygen and the atomic surface density of the *unreconstructed* Si(111), Si(100) and a-Si surfaces), as determined by XPS. The resolved PZL intensity ratio of the measured O 1s and Si 2p core-level peaks, $I_{\mathrm{O\,1s}}/I_{\mathrm{Si\,2p}}$, (after correction for the asymmetry factor; see Ref. [19]) is shown in Fig. 4.4 as function of the photoelectron detection angle α (with respect to the sample surface normal) for the O-exposed Si(111)-7x7, Si(100)-2x1 and a-Si surfaces (after 1800 s). For all three O-exposed Si surfaces, the resolved $I_{\mathrm{O\,1s}}/I_{\mathrm{Si\,2p}}$ intensity ratio is proportional to the inverse of cos(α) (see inset of Fig. 4.4), which complies with the behavior of a non-attenuating adsorption layer on an infinitely thick substrate [21]. In this case, the atomic surface density, s_o, of adsorbed oxygen on a Si substrate satisfies

$$\frac{I_{O\,1\mathrm{s}}(\alpha)}{I_{Si\,2\mathrm{p}}(\alpha)} = \frac{s_O}{\rho_{Si}} \frac{(d\sigma_O/d\Omega)}{(d\sigma_{Si}/d\Omega)\Lambda_{Si}\cos(\alpha)} \tag{4.2}$$

where ρ_{Si} is the atomic volume density of the Si substrate (either crystalline or amorphous), $(d\sigma_O/d\Omega)/(d\sigma_{\mathrm{Si}}/d\Omega)$ is the ratio of the photoionization cross sections of O 1s and Si 2p and Λ_{Si} denotes the inelastic mean free path of the Si 2p photoelectrons in the substrate. The thus calculated atomic surface densities of oxygen on the O-exposed Si(111), Si(100) and a-Si surfaces after t = 1800 s equal $1.3\cdot10^{15}$ atoms·cm^{-2}, $1.5\cdot10^{15}$ atoms·cm^{-2} and $6.46\cdot10^{14}$ atoms·cm^{-2}, respectively. The atomic surface densities of the clean, non-reconstructed Si(111) and Si(100) surfaces can be given as $7.83\cdot10^{14}$ atoms·cm^{-2} and $6.78\cdot10^{14}$ atoms·cm^{-2}, respectively, and the atomic surface density of the clean a-Si surface is estimated (on the basis of the macroscopic atom approach [25]) at $7.38\cdot10^{14}$ atoms·cm^{-2}. This results in estimates of 1.7, 2.2 and 0.9 for the fractional O coverage of the O-exposed Si(111)-7x7, Si(100)-2x1 and a-Si surfaces after t = 1800 s, respectively.

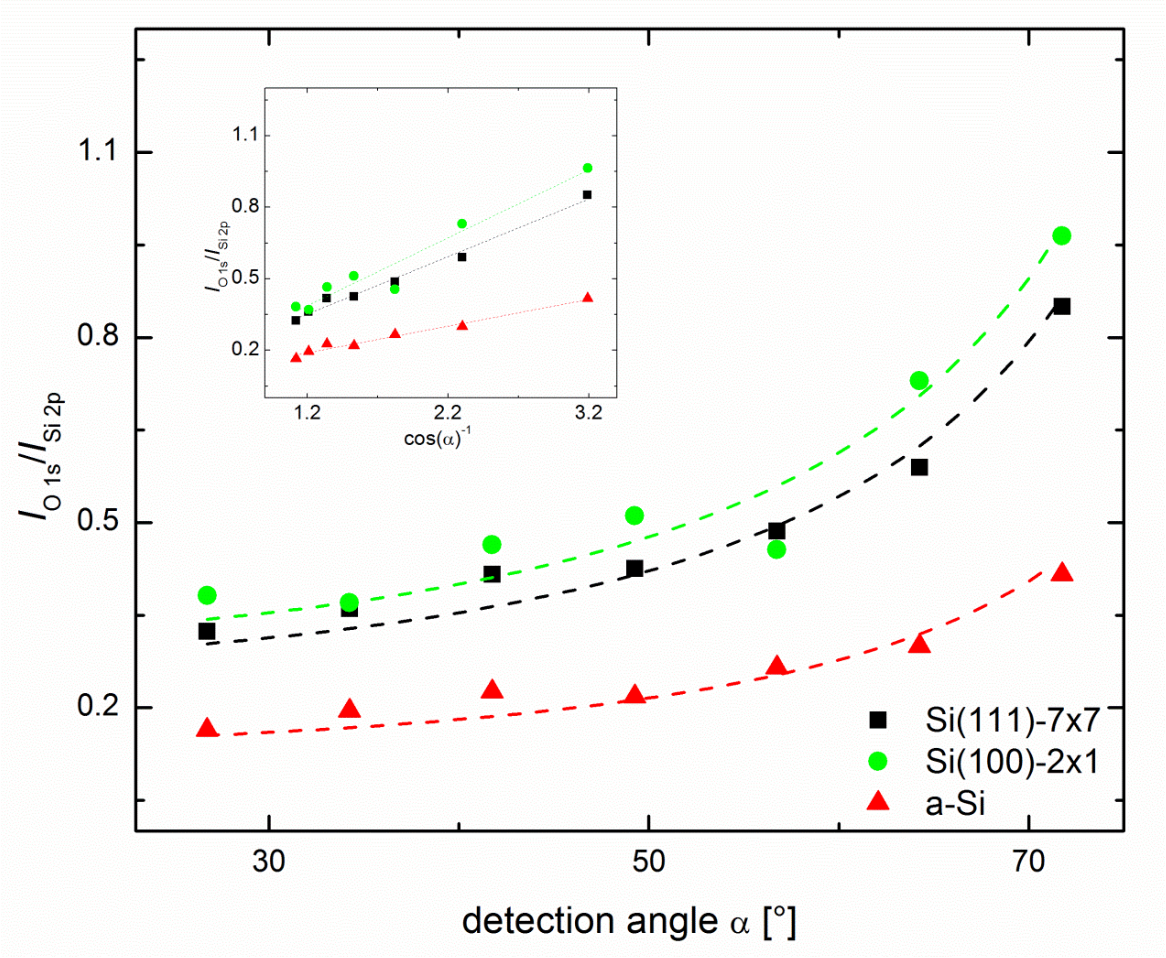

Fig. 4.4: The ratio of the asymmetry-factor-corrected intensities of the O 1s and Si 2p photoelectron peaks, $I_{\mathrm{O\ 1s}}/I_{\mathrm{Si\ 2p}}$, as function of the detection angle α after oxygen exposure of Si(111)-7x7, Si(100)-2x1 and a-Si surfaces at $p_{O_2} = 10^{-4}$Pa and 300 K for 1800 s. For all three surfaces the ratio increases proportionally to 1/cos(α) (see the dashed lines and the inset).

4.4 Discussion

The results shown in Figs. 4.2 and 4.3 indicate that the surface stress changes (i.e. curvature changes) due to O reaction with the front and the back surfaces are of the same order of magnitude; i.e. the back face effect cannot be neglected! This implies that the O-exposure-induced surface stress changes of only the well-prepared Si surfaces can only be extracted from specimen-curvature measurements if the back face effects can be determined accurately.

The clean, reconstructed Si(111)-7x7 surface has an intrinsic (tensile) surface stress of $\tau_{\mathrm{Si(111)-7x7}} \approx$ 2.3 N/m [26,27]. Combining, for the Si(111)-7x7 surface, the determined fractional O-coverage of 1.7 after 1800 s (section 3.3; Fig. 4.4) with the measured (compressive) change in surface stress of -1.9 N/m (Fig. 4.3), it follows that O exposure induces a decrease of the (initial, tensile) surface stress of -1.1 N/m per unit fractional coverage of O. This result complies well with the previously reported (partial) relaxation of the intrinsic tensile surface stress of clean Si(111)-7x7 surfaces upon O exposure at room temperature due to the incorporation of O atoms between a first-layer Si atom and a second-layer Si atom of the reconstructed surface; i.e. into Si backbonds [28], associated with a tendency to lateral volume expansion of the surface [10,12]. The value of -1.1 N/m for the surface stress change per unit coverage of O, as determined in the present study, is comparable to that reported in Ref. [12] (-0.82±0.25 N/m), but is inconsistent with that reported in Ref. [10] (-7.2 N/m), but this last result is flawed because the back face effect was neglected.

The clean, reconstructed Si(100)-2x1 surface has an intrinsic tensile surface stress along the Si dimer-bonds and an intrinsic compressive surface stress along the Si dimer-rows [29,30]. Combining, for the Si(100)-2x1 surface with orthogonal equivalent (2x1) domains, the determined fractional O-coverage of 2.2 after 1800 s (section 3.3; Fig. 4.4) with the measured (compressive) change in surface stress of -0.3 N/m (Fig. 4.3), it follows that O exposure induces a decrease of the surface stress of about -0.1 N/m per unit coverage of O. The adsorbed O species are incorporated into Si backbonds of the Si(100)-2x1 surface [31,32], which also (i.e. as for the Si(111)-7x7 surface) induces a compressive surface stress contribution due to the tendency to (lateral) volume expansion of the surface. Such O-adsorption-induced compressive surface stress can even lead to “push-out” (emittance) of Si atoms from the surface, forming isolated Si dimer bonds at the O-exposed Si(100)-2x1 surface [33,34].

For the Si(100)-2x1 surface, the initially small tensile and then gradually becoming compressive surface stress change can represent a transition of preferred oxygen adsorption site [35,36]: from O occupying the bridging sites in between adjacent Si dimer bonds to O insertion into Si backbonds. The formation of an oxygen-bridged structure leads to a distinct contraction of the Si(100)-2x1 surface parallel to the Si dimer-bonds [14], and thus induces a tensile surface stress contribution at the very initial stage of oxygen exposure of the Si(100)-2x1 surface.

The observation of an exclusively tensile surface stress change of 0.2 N/m per unit coverage of O, as reported in Ref. [10], is in sharp contrast with the tensile-compressive surface stress evolution as measured in the present study, which can be the consequence of different oxygen exposures or, likely, the consequence of the unjustified neglect of a back face effect correction in Ref. [10].

The clean a-Si surface has an intrinsic (tensile) surface stress of $\tau_{\mathrm{a-Si}} \approx$ 1.5±1.2 N/m [37]. Combining, for the a-Si surface, the determined fractional O-coverage of 0.9 (section 3.3; Fig. 4.4) after 1800 s with the measured (compressive) change in surface stress of -0.4 N/m (Fig. 4.3), it follows that O exposure induces a decrease of the (initial, tensile) surface stress by 0.5 N/m per unit coverage of O. The reduction of the tensile surface stress upon O exposure is again attributed to the (partial) incorporation of adsorbed O atoms into Si backbonds (i.e. subsurface sites) of the a-Si surface [38], which induces a compressive surface stress contribution due to the tendency to (lateral) volume expansion of the surface adjacant layer(s).

The value for the surface stress change (per unit coverage of O) for the 1800 s O-exposed a-Si surface is in-between the corresponding values for the 1800 s O-exposed Si(100)-2x1 and Si(111)-7x7 surfaces. It can therefore be concluded that the surface stress change upon O exposure decreases with decreasing atomic packing density of the clean Si surfaces (i.e. it decreases from Si(111), over a-Si to Si(100)). This result reflects that the less-densily packed Si surface regions contain more free volume for the accommodation (incorporation) of adsorbed O atoms and suggests that the detailed Si-O subsurface bonding geometry (bonding length and bonding angles) is of minor importance for the compressive surface stress change occurring upon oxygen exposure of Si surfaces.

4.5 Conclusion

Specimen-curvature based measurements of adsorption induced surface stress changes are largely affected by the undesired but unavoidable reaction(s) of the gaseous species at the back face of the specimen.

As demonstrated by a generally applicable, dedicated set of experiments, the oxygen-adsorption induced specimen curvature change at the (well-defined) atomically smooth front surfaces and the (poorly-defined) unpolished rough back surfaces of a Si specimen are of the same order of magnitude, and thus such “back face effect” cannot simply be neglected.

After subtraction of the “back face effect”, using the developed procedure, it is revealed that exposure of clean Si(111)-7x7, Si(100)-2x1 and a-Si surfaces to pure oxygen gas at $pO_2 = 1\times10^{-4}$ Pa and room temperature results in compressive surface stress changes for all three surfaces due to the incorporation of O atoms between a first-layer Si atom and a second-layer Si atom, i.e. into Si backbonds.

The measured surface stress change decreases with decreasing atomic packing density of the clean Si surfaces (i.e. from Si(111), a-Si to Si(100)), in correspondence with the less-densily packed Si surface regions containing more free volume for the accommodation of adsorbed O atoms.

References

[1] W. Haiss, Rep. Prog. Phys. **64,** 591 (2001).

[2] H. Ibach, Surf. Sci. Rep. **29,** 195 (1997).

[3] A. J. Schell-Sorokin and R. M. Tromp, Phys. Rev. Lett. **64,** 1039 (1990).

[4] R. C. Cammarata, Prog. Surf. Sci. **46,** 1 (1994).

[5] J. A. Floro, P. G. Kotula, S. C. Seel, and D. J. Srolovitz, Phys. Rev. Lett. **91,** 096101 (2003).

[6] R. D. Meade and D. Vanderbilt, Phys. Rev. Lett. **63,** 1404 (1989).

[7] A. M. Moulin, S. J. O'Shea, and M. E. Welland, Ultramicroscopy **82,** 23 (2000).

[8] R. Berger, E. Delamarche, H. P. Lang, C. Gerber, J. K. Gimzewski, E. Meyer, and H.-J. Güntherodt, Science **276,** 2021 (1997).

[9] J. Fritz, M. K. Baller, H. P. Lang, H. Rothuizen, P. Vettiger, E. Meyer, H. -J. Güntherodt, C. Gerber, and J. K. Gimzewski, Science **288,** 316 (2000).

[10] D. Sander and H. Ibach, Phys. Rev. B **43,** 4263 (1991).

[11] D. Sander, H. Ibach, *Adsorbate-induced changes of substrate properties* (SpringerMaterials - The Landolt-Börnstein Database).

[12] N. T. Kinahan, D. E. Meehan, T. Narushima, S. Sachert, J. J. Boland, and K. Miki, Phys. Rev. Lett. **104,** 146101 (2010).

[13] D. Flötotto, Z.M. Wang, L. P. H. Jeurgens, and E. J. Mittemeijer, submitted to Phys. Rew. Lett.

[14] M. Kitajima, T. Narushima, T. kurashima, A. Itakura, S. Takami, A. Yamada, K. Teraishi, and A. Miyamoto, J. Phys.: Condens. Matter **25,** 355007 (2013).

[15] T. Narushima, A. N. Itakura, T. Kurashina, T. Kawabe, and M. Kitajima, Appl. Surf. Sci. **159–160,** 25 (2000)..

[16] E. Chason and B. W. Sheldon, Surf. Eng **19,** 387 (2003).

[17] G. G. Stoney, Proc. R. Soc. A, **82,** 172 (1909).

[18] G. Hollinger and F. J. Himpsel, J. Vac. Sci. Technol. A **1,** 640 (1983).

[19] M. S. Vinodh and L. P. H. Jeurgens, Surf. Inter. Anal. **36,** 1629 (2004).

[20] L. P. H. Jeurgens, W. G. Sloof, C. G. Borsboom, F. D. Tichelaar, and E. J. Mittemeijer, Appl. Surf. Sci. **161,** 139 (2000).

[21] C. S. Fadley, Prog. Surf. Sci. **16,** 275 (1984).

[22] A. Jablonski and C. J. Powell, Surf. Sci. Rep. **47,** 33 (2002).

[23] O. Renner and J. Zemek, Czech. J. Phys. **23,** 1273 (1973).

[24] M. B. Trzhaskovskaya, V. I. Nefedov, and V. G. Yarzhemsky, Atomic Data and Nuclear Data Tables **77,** 97 (2001).

[25] F.R. de Boer, R. Boom, W.C.M. Mattens, A.R. Miedema, *Cohesion in Metalls: Transition Metals Alloyes* (Elsever Science, Amsterdam, North Holland, 1989).

[26] R. D. Meade and D. Vanderbilt, Phys. Rev. B **40,** 3905 (1989).

[27] D. Vanderbilt, Phys. Rev. Lett. **59,** 1456 (1987).

[28] Y. T. Akitaka Yoshigoe, Jpn. J. Appl. Phys. **49,** 115704 (2010).

[29] M. C. Payne, N. Roberts, R. J. Needs, M. Needels, and J. D. Joannopoulos, Surf. Sci. **211–212,** 1 (1989).

[30] Y. Miyamoto, Phys. Rev. B **49,** 1947 (1994).

[31] T. Uchiyama and M. Tsukada, Phys. Rev. B **53,** 7917 (1996).

[32] M. Wasekura, M. Higashi, H. Ikeda, A. Sakai, S. Zaima, and Y. Yasuda, Appl. Surf. Sci. **159–160,** 35 (2000).

[33] H. Kageshima and K. Shiraishi, Phys. Rev. Lett. **81,** 5936 (1998).

[34] D. G. Cahill and P. Avouris, Appl. Phys. Lett. **60,** 326 (1992).

[35] M. N. Yoshinao Harada, Takaharu Nagatomi, Ryuichi Shimizu, Jpn. J. Appl. Phys. **39,** 560 (2000).

[36] Y. Miyamoto and A. Oshiyama, Phys. Rev. B **41,** 12680 (1990).

[37] S. Hara, S. Izumi, T. Kumagai, and S. Sakai, Surf. Sci. **585,** 17 (2005).

[38] T. Nagatomi, Y. Harada, M. Niwa, Y. Takai, and R. Shimizu, Surf. Inter. Anal. **27,** 776 (1999).

Chapter 5

Intrinsic stress evolution during amorphous oxide film growth on Al surfaces

D. Flötotto, Z. M. Wang, L. P. H. Jeurgens and E. J. Mittemeijer

Abstract

The intrinsic stress evolution during formation of ultrathin amorphous oxide films on *bare* Al(111) and Al(100) surfaces by thermal oxidation at room temperature in pure oxygen gas was investigated in real-time by *in-situ* substrate curvature measurements in combination with detailed atomic-scale microstructural analyses. It was found that during the thickening of the developing oxide a considerable amount of growth stresses is generated in, remarkably even amorphous, ultrathin Al_2O_3 films. The surface orientation-dependent stress evolutions during the onset of O adsorption on the bare Al surfaces and during subsequent oxide-film growth can be interpreted as a result of (i) adsorption-induced changes of surface stress and (ii) competing processes of free volume generation and structural relaxation during continued oxide film growth, respectively.

5.1 Introduction

Thin (native) oxide films are formed spontaneously on most metallic surfaces under ambient conditions. Although the thickness of such a surficial oxide film is typically less than 10 nm, it governs many important properties of the oxidized material system, such as the electronic conductivity, adhesion, wetting, friction, wear and corrosion resistance [1-3].

The formation of a thin oxide film on a metal surface upon exposure to an oxidizing atmosphere involves a series of competing and overlapping steps, including physisorption of O molecules, dissociative O chemisorption, oxide nucleation and oxide-film growth. As soon as the entire substrate surface is covered by a laterally closed oxide film, further oxide-film growth is limited by the transport of the reactant species through the oxide film. At low temperatures (say, $T < 600$ K), this transport is driven by a surface-charge field due to the so-called kinetic potential, which builds up between the metal substrate and (charged) chemisorbed oxygen species on the oxide surface [4-7]. The surface-charge field strength linearly decreases with increasing oxide-film thickness and as a result, at the low temperatures considered, the formed oxide films exhibit near-limiting thicknesses (< 10 nm).

For many metals, such as Al, Si and Zr, the initial formation of an *amorphous* instead of a *crystalline* oxide film is (thermodynamically) preferred [8,9]. Such amorphous oxide films are generally considered to be stress free [10,11], since by definition no intrinsic stresses due to lattice mismatch can arise between a crystalline substrate and an amorphous thin film. Moreover, amorphous oxides are characterized by a large amount of free volume [12] and a high bond flexibility, which facilitate relaxation of (applied) stresses at relatively low temperatures [11].

Surprisingly, this study reveals that a significant intrinsic stress can arise in the amorphous oxide film formed on a *bare* Al metal surface during oxidation at room temperature. Such intrinsic growth stresses in (amorphous) oxide films can strongly affect the mechanical, chemical, electronic and/or optical properties of the material, and can thus play a crucial role in technologies such as microelectronics and functional metal surfaces in catalysis, coating and biomedical applications. Up to date, no experimental investigations on the development of stress in ultrathin *amorphous* oxide films forming on metal surfaces have been reported. Only the intrinsic stress evolutions of much *thicker* (in the micrometer range), *crystalline* oxide films on metals and alloys have been studied for thermal oxidation at elevated temperatures [13-15].

5.2 Experimental

All experiments were carried out in a custom-designed ultrahigh vacuum (UHV) system for specimen processing and in-situ analyses, which consists of interconnected UHV chambers for thin-film deposition by thermal evaporation (base pressure < 1×10^{-8} Pa), in-situ Angle-Resolved X-ray Photoelectron Spectroscopy (AR-XPS) (base pressure < 6×10^{-8} Pa) and thermal oxidation (base pressure < 1×10^{-8} Pa).

5.2.1 Preparation of Single-crystalline Al thin films

For the epitaxial growth of single-crystalline Al(111) and Al(100) thin films (with thicknesses > 60 nm), square-shaped (13.9x13.9 mm^2), one side polished, 100 µm thin Si(111) and Si(100) wafers (miscut < 0.1°) were loosely mounted in a Mo sample holder, introduced into the ultrahigh vacuum (UHV) system and thoroughly degassed and cleaned by a programmed laser heat treatment up to a maximum temperature of 1100°C for 1 min in UHV. After subsequent cooling to room temperature, scanning tunneling microscopy (STM) and angle-resolved X-ray spectroscopy (AR-XPS) measurements reveal contamination-free, well ordered Si(111)-7x7 and Si(100)-1x2 surfaces, respectively.

For the preparation of clean Al(111) surfaces, 60 nm thick Al films were grown epitaxially on the Si(111)-7x7 surface by thermal evaporation of pure Al (> 99.9999 at%) from PBN crucible with a deposition rate of 1.37 nm/min at room temperature. Next, the as grown Al films were annealed at 160°C for 1 hour. As verified by ex-situ X-ray diffraction (XRD)-pole figure measurements recorded at $2\theta = 38.4°$ (Cu-$K\alpha$ radiation), the thus prepared Al films are single crystalline with an orientation relationship with the substrate described by Al(111)||Si(111) and Al[$1\bar{1}0$]||Si[$1\bar{1}0$] [16,17]. Furthermore, as revealed by ex-situ atomic force microscopy (AFM) the root mean square roughness (RMS) of the Al(111) film surface is as low as 1.0 nm (see Fig. 5.1a).

Since epitaxial growth of Al(100) films cannot be archived by direct deposition of Al on Si(100) surfaces, for the preparation of Al(100) surfaces initially 160 nm thick Ag(100) buffer layers were grown epitaxially on the Si(100)-1x2 substrate surfaces by thermal evaporation of Ag (> 99.995 at%) from a Al_2O_3 crucible with a deposition rate of 28.3 nm/min at a constant substrate temperature of 160°C [17]. After annealing the as grown Ag films for 2 h at 160°C and subsequent cooling of the specimen to room temperature, 120 nm thick Al films were grown epitaxially on top of the Ag film with a deposition rate of 3.9 nm/min. As evidenced by ex-situ XRD {111}-pole figure measurements, the Al/Ag layer exhibits practically an orientation relationship with the substrate described by Al(100)||Ag(100)||Si(100) with Al[$1\bar{1}0$]||Ag[$1\bar{1}0$]||Si[$1\bar{1}0$] (note that due to the (small) lattice-parameter difference of Al and Ag, the {111}-pole figure recorded at $2\theta = 38.4°$ (Cu-$K\alpha$ radiation) also includes non-discernible intensity from Ag texture

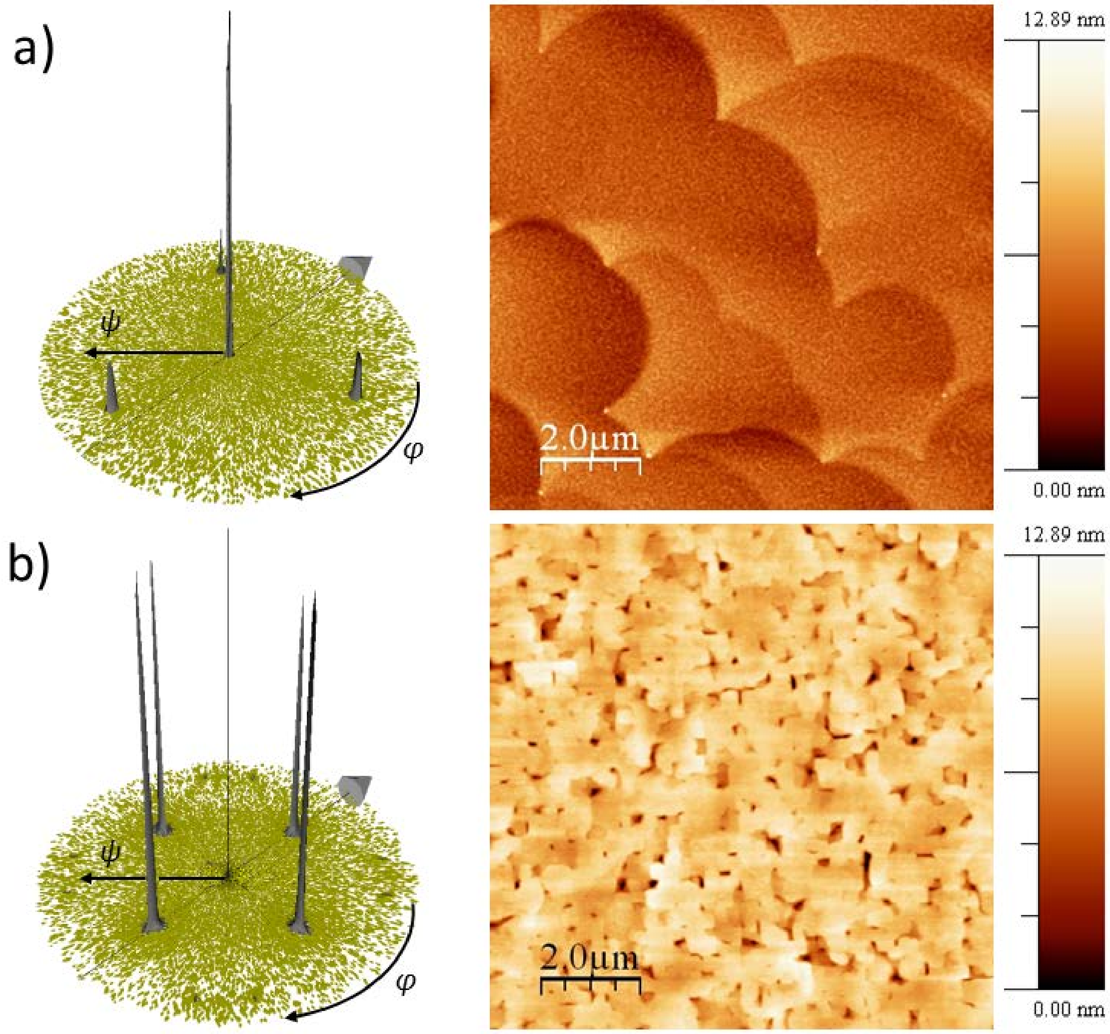

Fig. 5.1. XRD {111}-pole figures (recorded at $2\theta = 38.4°$; Cu-$K\alpha$ radiation) reveal that the growth of Al films on **(a)** a Si(111) substrate and **(b)** a Ag(100)/Si(100) substrate resulted in the formation of epitaxial, practically single-crystalline Al films with an orientation relationship with the substrate described by Al(111)||Si(100) with Al[$1\bar{1}0$]||Si[$1\bar{1}0$] and by Al(100)||Ag(100)||Si(100) with Al[$1\bar{1}0$]||Ag[$1\bar{1}0$]||Si[$1\bar{1}0$], respectively. As verified by ex-situ AFM analysis, the root mean square roughness of the Al(111) and Al(100) surfaces are as low as 1.0 nm and 1.4 nm, respectively.

components). Only a very small amount of grains with {111} planes parallel to the specimen surface were detected (< 0.5 vol%; as calculated from the ratios of the maximum peak intensities of the Al(111)/Ag(111) and Al(100)/Ag(100) components taking into account the respective structure factors); twinning on (111) planes, inclined to the surface, led to a negligibly small fraction of a texture component with (151) planes parallel to the surface. The RMS of the Al film surface, as deduced from the AFM measurements, is 1.4 nm (see Fig. 5.1b).

5.2.2 Oxidation and real-time in-situ analysis

For the oxidation experiments, two identical specimens, positioned on different manipulators in the UHV system, were *simultaneously* oxidized at 300 K by admitting pure oxygen gas (purity 99.997 vol.%) to the chamber for a given time at a constant partial pressure, p_{O_2}, of successively 1 x 10^{-4} Pa, 1 x 10^{-2} Pa and 1.0 Pa. After each successive oxygen exposure step (at constant p_{O_2}), the oxygen valve was closed for at least 10 min to reestablish UHV conditions. For one specimen, the kinetics of oxide-film growth during each successive oxidation step were traced by real-time in-situ spectroscopic ellipsometry (RISE) (see Ref. [6] and Appendix 5.A). For the other (identical) specimen, real-time in-situ substrate-curvature measurements were performed with a multi-optical stress sensor [18,19] to monitor the film-force evolution during oxidation, while correcting for the (predetermined) substrate back-side effects (i.e. substrate curvature changes induced by the reaction of oxygen with the wafer back side; see Chapter 4, and Appendix 5.B). The error of the film force is ± 0.03 N/m.

The film force change, $\Delta\tau$, due to oxygen chemisorption, oxide nucleation and oxide-film growth on the clean Al surfaces is given by

$$\Delta\tau = \Delta\{\langle\sigma_{\mathrm{Al}}\rangle h_{\mathrm{Al}} + \langle\sigma_{\mathrm{ox}}\rangle h_{\mathrm{ox}} + f\} \tag{5.1}$$

where the first and second term denote the change of the product of the (thickness-averaged) in-plane film stress, $\langle\sigma_i\rangle$, and the film thicknesses, h_i, for the Al film (i = Al) and the Al-oxide film (i = ox), respectively, and the third term represents the change/appearance of the surface stress, f, at the Al and the oxide film surfaces [20]. After the oxidation, the chemical constitutions and the thicknesses of the oxide films were investigated in-situ by AR-XPS using a Thermo VG Thetaprobe system [21].

5.2.3 High resolution transmission electron microscopy

After oxidation of the Al(111) and Al(100) surfaces and subsequent XPS analysis the microstructure and morphology of the oxide films was studied ex-situ by cross-sectional high-resolution transmission electron microscopy (HRTEM). To this end the formed Al_2O_3 films were sealed in-situ by deposition of a 120 nm thick Al capping layer at a substrate temperature of ≈ 170 K. Next, the capped specimens were removed from UHV and thin cross-section TEM foils were prepared by firstly pre-thinning the specimen by a tripod polisher to a thickness of about 10 µm and secondly by ion milling under liquid-nitrogen cooling in a Precision Ion Polisher 691 operating at an accelerating voltage of 2 keV. Note that during the whole preparation procedure the specimens were not heated above 300 K. The HRTEM analysis was performed applying a JEOL ARM1250 microscope with an acceleration voltage of 1250 kV. To ensure that the observed oxide film microstructures are not affected by prolonged electron irradiation of a single position of the specimen, all HRTEM micrographs, as presented in the present study, were recorded within irradiation times of less than two minutes during which no microstructural changes could be observed.

5.3 Results and discussion

Typical evolutions of the ellipsometric parameters, $\delta\Delta$ and $\delta\Psi$, at a central wavelength of λ = 589 nm, as measured by RISE, for the step wise, cumulative oxidations of the Al(111) and Al(100) surfaces (at various p_{O_2}), are shown in Figs. 5.2(a) and 5.2(a), respectively. For thin dielectric films, such as Al_2O_3, the decrease of the phase shift, $\delta\Delta$, scales practically linearly with the film thickness, whereas the change of the amplitude ratio, $\delta\Psi$, is only sensitive to changes in the dipole interactions at the concerned surface (and not to the presence of a non-absorbing thin Al_2O_3 film) [22]. At the initial stage of interaction of oxygen gas with Al(111) and Al(100) surfaces, the rate of incorporation of O into the Al surfaces exceeds the rate of on-top chemisorption of O, resulting in the observed, initial drop of $\delta\Psi$ (see Figs. 5.2a and 5.3a and Refs. [6,23-26]). Subsequently, for the densely-packed Al(111) surface, on-top chemisorption becomes dominant leading to the formation of an ordered (1×1) chemisorbed oxygen layer [24,27,28], which is associated with an increase of $\delta\Psi$ (Fig. 5.2a) [6,24]. Then, as soon as the ordered (1×1) adlayer on Al(111) has transformed into a three-dimensional closed oxide layer covering the metal surface, the value of $\delta\Psi$ remains practically constant (Fig. 5.2a). For the less close-packed Al(100) surface, O incorporation remains promoted over O chemisorption and, consequently, the formation of an ordered O chemisorption phase is hindered [24,26,29]; indeed, only the initial drop of $\delta\Psi$ is observed, after which $\delta\Psi$ remains constant. Hence, the measured courses of $\delta\Psi$ during oxidation indicate distinct differences in the mechanism of nucleation of a 3-dimensional oxide phase on the Al(111) and Al(100) surfaces: oxide nucleation on Al(111) proceeds from an ordered (1×1) chemisorbed oxygen layer, whereas for the more open Al(100) surface oxide nucleation proceeds directly from randomly incorporated O in the Al film surface.

The oxide-film growth curves (at 300 K), as determined by a combined approach of RISE and AR-XPS measurements [6], are given in Figs. 5.2b and 5.(b. For every oxidation step of the Al(111) and Al(100) surfaces, each at constant p_{O_2}, the oxide-film growth exhibits an initial fast growth regime, followed by a second stage with a much slower, gradually decreasing growth rate. Such passivation behavior is typical for the oxidation of Al surfaces at relatively low temperatures, as discussed above. After fast formation of a closed oxide film during the initial fast growth regime, continued oxide-film growth is rate limited by the outward transport of cations under influence of the surface charge field due to the kinetic potential [5-7]. As a result of an increasing number of absorbed oxygen species with increasing p_{O_2}, and thus an increasing density of electron acceptor levels for the built-up of the surface-charge field, the absolute value of the kinetic potential (and thereby the surface-charge field strength) increases with increasing p_{O_2}, which implies step-wise increase of the near-limiting oxide film thickness with step-wise increase of p_{O_2}. The limiting thicknesses approached during the slow oxidation stages at a p_{O_2} of 1 x 10^{-4} Pa, 1 x 10^{-2} Pa and 1.0 Pa equal 0.76 ± 0.09 nm, 1.07 ± 0.08 nm and 1.35 ± 0.13 nm, respectively, for the Al(111) surface and 0.58 ± 0.12 nm, 0.78 ± 0.13 nm and 1.21 ± 0.14 nm, respectively, for the Al(100) surface (see Figs. 5.2b and 5.3b). As revealed by AR-XPS, the increase of the near-limiting thickness is accompanied by an increase of the overall O/Al ratio in the oxide film from 1.5 ± 0.1 to 1.7 ± 0.1; performing quantitative AR-XPS analyses similar to that described in Ref. [21], it follows that with increasing p_{O_2}non-stoichiometric, cation deficient oxide films develop. All of the above results for the room-temperature oxidation of Al(111) and Al(100) film surfaces are in excellent agreement with previous studies on the thermal oxidation of Al(111) and Al(100) bulk single crystals [6,7,21].

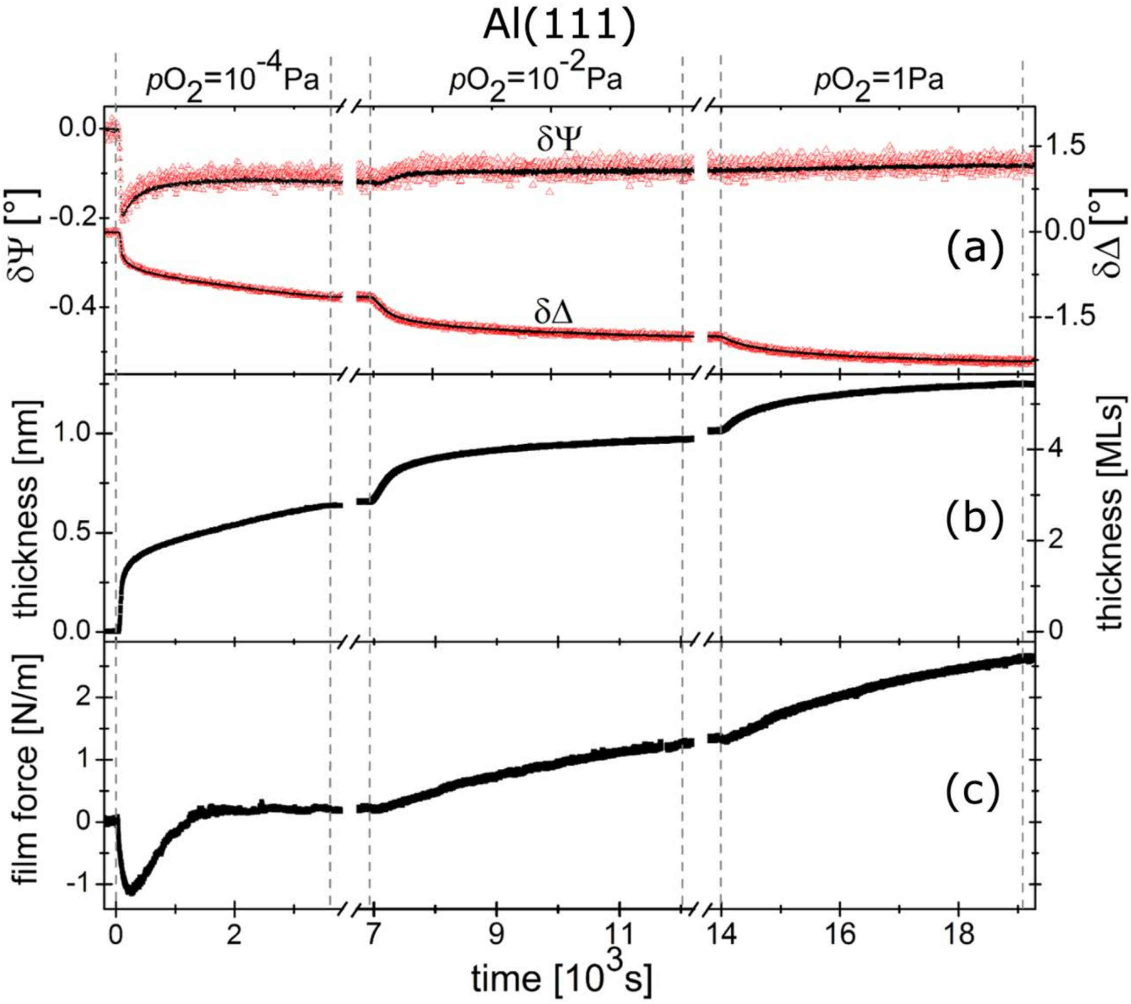

Fig. 5.2. Oxidation of the bare Al(111) surface as function of time at 300 K and at p_{O_2} of 1 x 10^{-4} Pa, 1 x 10^{-2} Pa and 1 Pa, successively. Representative evolutions of the measured ellipsometric parameters δΨ and δΔ at λ = 589 nm, as well as the result of fitting of δΨ and δΔ **(a)**; the oxide film-growth curves **(b)**; the backside-effect-corrected evolution of the change of film force **(c)**.

The time evolutions of the film force (at 300 K) are shown in Figs. 5.2c and 5.3c. The film-force evolutions, $\Delta\tau$, also (i.e. as for the course of $\delta\Psi$; see above) strongly depend on the Al surface orientation. Oxidation of the Al(111) surface commences, at p_{O_2} = 1x10^{-4} Pa, with an instantaneous *compressive* film-force change to a minimum value of -1.2 N/m at $t \approx 230$ s (Fig. 5.2c). The film force subsequently increases to +0.2 N/m, thus becoming *tensile*. Continued oxide-film growth during the following oxygen exposure steps leads to an increase of the (tensile) film force to 1.3 N/m at p_{O_2} = 1x10^{-2} Pa (thickness = 1.0 nm) and 2.6 N/m at p_{O_2} = 1.0 Pa (thickness = 1.3 nm). As for the Al(111) surface, oxidation of the Al(100) surface at

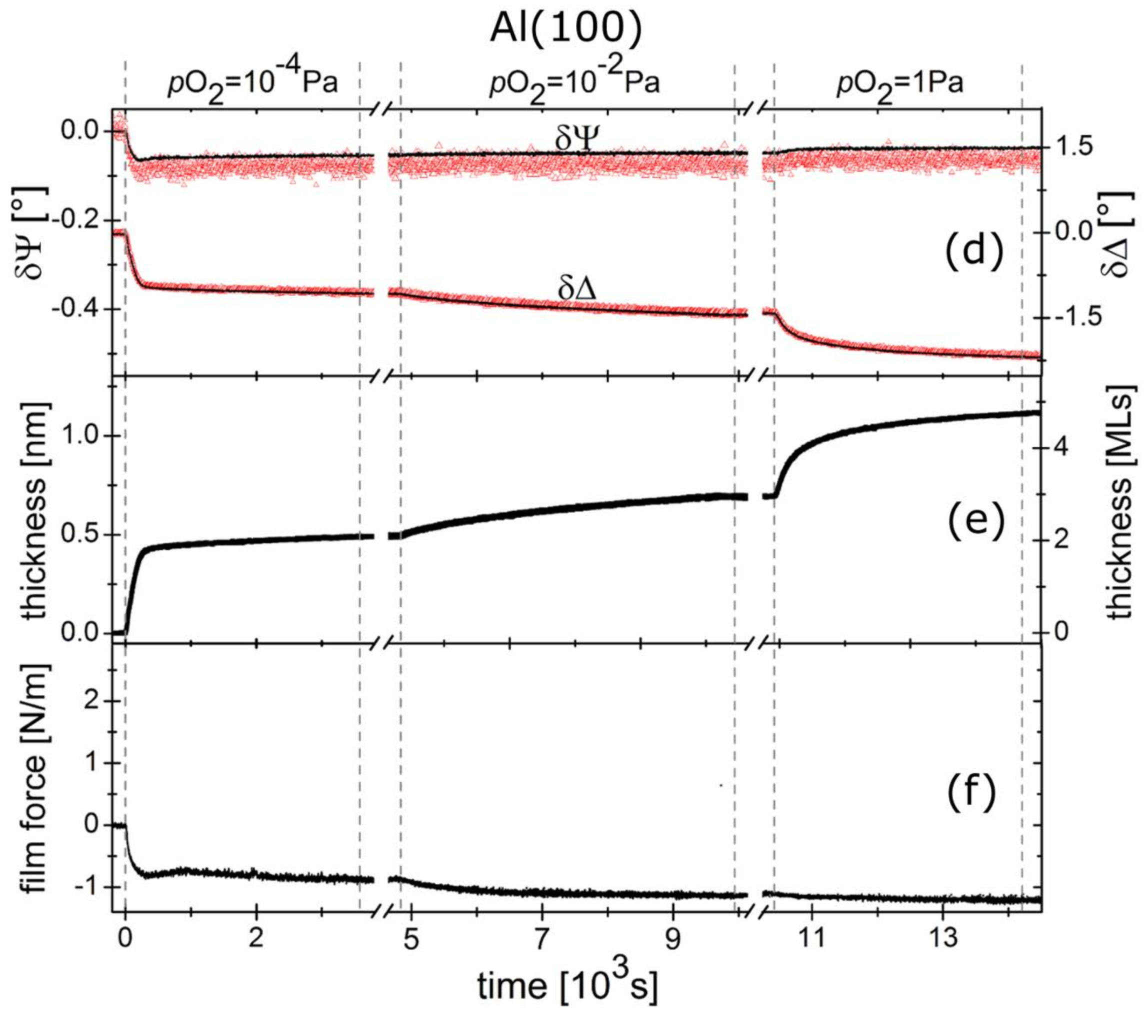

Fig. 5.3. Oxidation of the bare Al(111) and Al(100) surfaces as function of time at 300 K and at p_{O_2} of 1×10^{-4} Pa, 1×10^{-2} Pa and 1 Pa, successively. Representative evolutions of the measured ellipsometric parameters δΨ and δΔ at λ = 589 nm, as well as the result of fitting of δΨ and δΔ **(a)**; the oxide film-growth curves **(b)**; the backside-effect-corrected evolution of the change of film force **(c)**.

p_{O_2} = 1x10^{-4} Pa results in an instantaneous *compressive* film-force change; in this case the film force equals -0.8 N/m after $t \approx 350$ s (Fig. 5.3c). However, in contrast with the Al(111) surface, during the following oxygen exposure steps at p_{O_2} = 1x10^{-2} Pa and p_{O_2} = 1.0 Pa the film force remains almost constant with a final (compressive) value of -1.1 N/m. Noteworthy, for both Al surfaces, no changes of the film force are observed upon interruption of the oxygen exposure at any stage of oxidation (see Figs. 5.2c and 5.3c as well as Appendix 5.C).

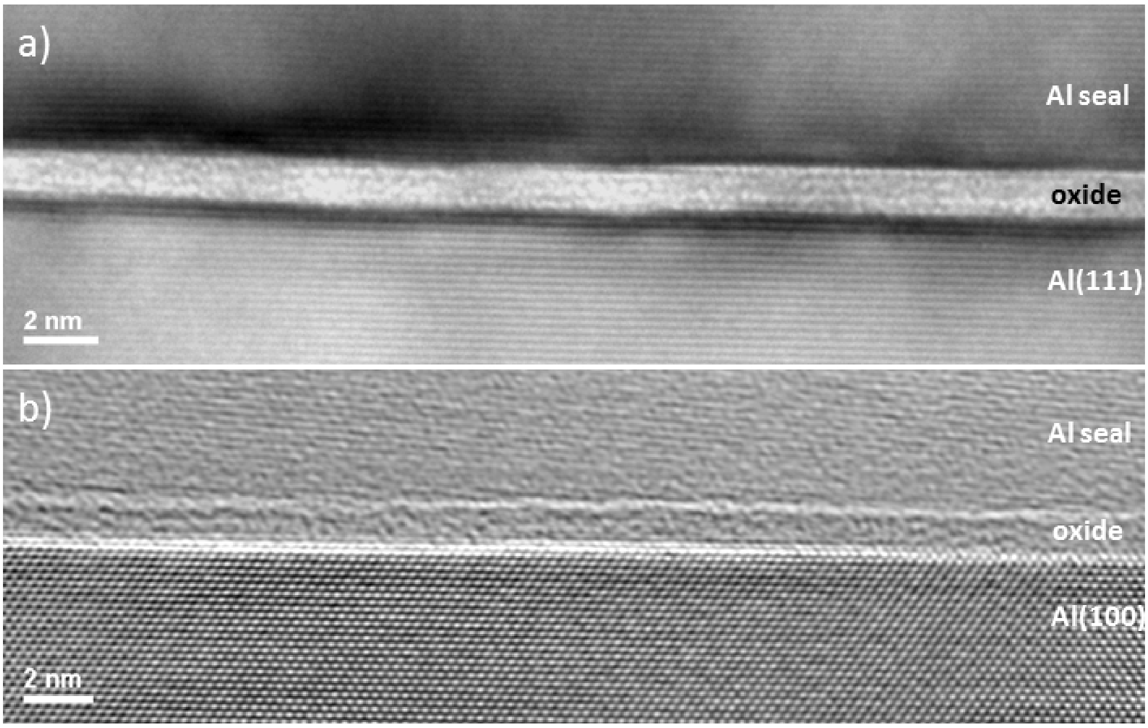

Fig. 5.4. Cross-sectional HRTEM micrographs of the amorphous Al2O3 oxide film formed on **(a)** the Al(111) film surface and **(b)** the Al(100) film surface, after successive oxygen gas exposures at $p_{O_2} = 1 \text{ x } 10^{-4}$ Pa, $p_{O_2} = 1 \text{ x } 10^{-2}$ Pa and $p_{O_2} = 1$ Pa at 300 K (see Figs. 5.2 and 5.3).

Cross-sectional HRTEM micrographs of the oxide films, as formed on the Al surfaces after the successive oxygen exposure steps up to 1.0 Pa, are shown in Fig. 5.4. Evidently, the developing oxide films on Al(111) and Al(100) surfaces are both amorphous, and have uniform thicknesses of 1.3 ± 0.1 nm and 1.2 ± 0.1 nm, respectively, in accordance with the thickness values determined by AR-XPS.

The HRTEM analyses indicate that the amorphous oxide films on Al(111), as nucleated and grown from an ordered (1×1) chemisorbed oxygen layer (see above), have a higher degree of medium-range order (i.e. a more restrict alignment of neighboring 'building blocks' of [AlO4] and [AlO6] polyhedral; see what follows) as compared to those on Al(100): compare Figs. 5.4 a and 5.4 b.

The contrasting film-force evolutions of the developing oxide films on Al(111) and Al(100) can be rationalized, considering the differences in the microstructural evolutions of both amorphous oxide films, as follows. The bare Al(111) and Al(100) surfaces intrinsically exhibit a tensile surface stress as a consequence of the spilling-out of electrons from the surface into the vacuum [30,31]. The initial incorporation of O into the Al subsurface (see above) reduces the spilling-out of electrons from the metal surfaces [32] and causes a volume expansion of the subsurface region. Consequently, compressive stress components parallel to the surface are induced in the Al surface regions at the onset of oxygen exposure (Figs. 5.2c and 5.3c). A significantly higher instantaneous compressive surface stress component is generated upon oxygen incorporation into the bare Al(111) surface, which is a direct consequence of the higher atomic density of the Al(111) surface as compared to the more open Al(100) surface. The stress induced in the subsurface region by a surface-area fraction incorporated O into each Al surface can be estimated from the measured (linear) decrease of the film force and the experimental linear oxidation rate regime[1] at the onset of oxidation (i.e. for equivalent oxide thicknesses < 2.3 Å). The thus estimated surface stress contribution by incorporated O atoms equals -1.5 ± 0.6 N/m for Al(111) and -0.4 ± 0.1 N/m for Al(100) (each result is the average of three measurements, employing atomic densities of 1.41×10^{19} m^{-2} and 1.22×10^{19} m^{-2} for the Al(111) and Al(100) surfaces [24] and taking the average number of O atoms per unit volume equal to the value of amorphous Al_2O_3 (i.e. 5.62×10^{28} m^{-3} [33])).

After the instantaneous development of a compressive stress component in the subsurface region during the onset of O interaction with the bare Al(100) surface, no further significant changes in the film force are observed during continued growth of the amorphous oxide film on Al(100) (Figs. 5.3 a-c): The successive increments of p_{O_2}, led to a step-wise thickening of the oxide film, but no growth stress evolved in the amorphous oxide films formed on Al(100).

In case of the Al(111) surface, after the development of instantaneous compressive surface stress at the very beginning of O interaction (as discussed above), on-top O adsorption becomes dominant over oxygen incorporation and an ordered (1x1) chemisorbed oxygen overlayer is formed (which does not develop on the Al(100) and is associated with an increase of the ellipsometric parameter Ψ; see above discussion). As a result of the predominant on top surface adsorption of electronegative oxygen atoms at this stage of oxygen exposure, the electron

---

[1] At the initial stage of oxygen interaction with the Al surfaces the fraction incorporated oxygen increases linearly with time, since the number of absorbed oxygen atoms at the parent Al surfaces is only determined by the amount of oxygen atoms supplied from the gas phase and the sticking coefficients of the concerned surfaces.

depletion of the Al(111) surface is enhanced and thus a distinct tensile stress component is induced into the Al subsurface region (see Figs. 5.2a and 5.3c) [32].

Contrary to the Al(100) oxidation, with increasing thickness of the amorphous oxide film on the Al(111) surface a significant tensile stress development takes place, exclusively during thickening of the oxide film (no changes of the film force are observed upon interruption of the oxygen exposure; see Fig. 5.2c and supplementary material). Independent of the Al surface orientation, thickening of the oxide films is realized by the outward transport of Al cations through the oxide film under influence of the surface-charge field (see above), which results in the formation of vacancies in the Al substrate at the metal/oxide interface [6]. Since self-diffusion of Al at 300 K is too slow [34] to enable significant diffusion of the oxidation-induced vacancies into the bulk of the Al films, it is likely that these oxidation-induced vacancies are annihilated at the metal/oxide interface. This would result in a reduction of the nominal Al film thickness of up to about 0.9 nm (as estimated on the basis of the near-limiting oxide-film thickness attained at 1.0 Pa; see Figs. 5.2b and 5.3b). The resulting (relatively small) negative film-force contribution (due to the reduction of the Al film thickness, while the thickness-averaged film stress remains constant) would be of similar magnitude for both Al surfaces and therefore cannot explain the strikingly different stress evolutions for the Al(111) and Al(100) oxidations. Hence, the occurrence of tensile stresses during oxide-film thickening on Al(111) and the stress-free oxide-film growth on Al(100) must be associated with differences of the microstructural evolutions of the amorphous oxide films.

The amorphous oxide films formed on Al(111) and Al(100) can be described as constituted of neighboring 'building blocks' of edge- and corner-sharing [AlO_4] and [AlO_6] polyhedra (with the Al cations in, respectively, tetrahedral and octahedral interstices of the distorted, densely-packed oxygen sublattice) [35] where the free volume is associated with vacancy-type defects [36]. As evidenced by the increasing overall O/Al-ratio of the cation deficient oxide film during continued oxide-film growth (i.e. with increasing p_{O_2}; see above) additional free volume (cation vacancies) is continuously added to the thickening oxide. In the absence of structural relaxation during continued oxide-film growth, the continuous increase of free volume associated with a tendency for shrinkage of the lateral film dimensions would lead to the buildup of a tensile stress component *in* the amorphous oxide film. However, if structural relaxation processes (i.e. rearrangement and/or a fractional change of the amount of [AlO_4] and [AlO_6] building blocks) can occur during oxide growth, the additional free volume can be annihilated and thus the generated tensile stress will be reduced or even fully relaxed. As indicated by HRTEM (Fig. 5.4), the developing oxide films on Al(111) exhibit a more restrict alignment of neighboring 'building blocks' of edge- and corner-sharing [AlO4] and [AlO6] polyhedral than those on Al(100). This more restrict alignment of neighboring 'building blocks' in the amorphous oxide film on Al(111) is most likely inherited from the ordered (1×1) [24,27] oxygen adlayer as formed during the initial stage of O interaction with the bare Al(111) surface [37]. No such ordered O adlayer occurs upon oxidation of Al(100) [24,26]. This suggests that structural relaxation during oxide-film growth on Al(100) is more pronounced than on Al(111). As a result, the tensile oxide-film stress due to generated free volume can be largely relaxed during growth of the oxide film on Al(100), in contrast with the evolving oxide film on Al(111). This is consistent with XPS chemical state analysis showing that the rearrangement of the [AlO_4] and [AlO_6] building blocks starts already at lower temperatures for oxide films formed on Al(100), as compared to the oxide films grown on Al(111) [12].

5.4 Conclusion

In conclusion, the present study demonstrates that pronounced intrinsic stresses can be generated in ultrathin *amorphous* Al_2O_3 films formed by thermal oxidation of bare Al surfaces at low temperatures. The magnitude of the stress strongly depends on the Al surface orientation: Oxide films formed on Al(100) are stress free, whereas oxide films formed on Al(111) exhibit a thickness averaged in-plane tensile film stress as large as 1.9 GPa. The striking dependence of stress evolution on the Al surface orientation is the result of adsorption induced changes of surface stress at the very beginning of oxygen exposure, and competing processes of free volume generation and structural relaxation during continued oxide-film growth. The here disclosed significant intrinsic stress formation in, even amorphous, ultrathin (native) oxide films has to be accounted for in the tailoring of functional properties of ultra-thin (native) oxide films on metal and metallic alloy surfaces.

Acknowledgement

The authors are grateful to U. Salzberger for the preparation of the TEM foils, P. Kopold and Dr. F. Phillipp for the HRTEM investigation and to Dr. P. A. van Aken for TEM support and advice.

Appendix 5.A. Real time in-situ spectroscopic ellipsometry (RISE) analysis and data evaluation

The RISE analysis was performed with a J.A. Woollam M-2000L spectroscopic ellipsometer equipped with a Xe light source. The ellipsometric phase shift and the amplitude-ratio parameters, $\Delta(\lambda)$ and $\Psi(\lambda)$, were recorded in the wavelength (λ) range between 350 nm and 800 nm as function of time at equal incident and reflection angles of 70° relative to the sample surface normal. In order to deduce the oxide-film growth curves from the measured changes in the spectra of $\Delta(\lambda)$ and $\Psi(\lambda)$ as a function of oxidation time, the model from Ref. [6] was adopted, which considers the overgrowth of an Al_2O_3 film on the bare substrate surfaces of uniform thickness L^{ox} in combination with a very thin non-stoichiometric Al_2O_3 interface layer of thickness L^{int}. The optical constants of the bare Al substrates were determined prior to oxygen exposure, whereas the optical constants of the Al_2O_3 film (expressed by a Cauchy-type function) and the fraction of the non-stoichiometric Al_2O_3 interface layer (estimated using an effective medium approach (EMA)) were deduced by optimizing the Cauchy parameter A and the EMA fraction β (see Ref. [6]) while fixing the *total* oxide film thickness at the end of each oxidation experiment to the value deduced from XPS analysis. Independent of the Al film-surface orientation the optimized values of the Cauchy parameter A was 1.65, which is in very good agreement with the values obtained from Al single crystals (see Ref. [6] and references therein). The EMA fraction β was found to be equal to 0.87 and 0.39 for the oxide-film growth on Al(111) and Al(100) substrates, respectively. Afterwards the oxide growth curves were obtained by fitting the calculated data of $\Delta(\lambda)$ and $\Psi(\lambda)$ as a function of oxidation time to the corresponding measured data with the thicknesses L^{ox} and L^{int} as fit parameters and adopting the above values of A and β.

Appendix 5.B. Substrate backside-effect corrections

Since the reaction of oxygen with both the specimen front-side (i.e. the Al surfaces) *and* the specimen rough Si wafer back-side can result in a measurable change of film force, it is essential in the present investigation of the film-force change during oxidation of the Al surface to accurately determine and correct for the backside effect. To this end a similar set of experiments as described in Chapter 4 was conducted: (i) Firstly, a 15 nm thick a-Si layer was deposited on the surfaces of thoroughly degassed one side polished Si(111) and Si(100) wafers. (ii) Next, the specimens were exposed to pure oxygen gas at partial pressures of, successively, 1 x 10^{-4} Pa, 1 x 10^{-2} Pa and 1 Pa for t = 1800 s each, while recording the change of substrate curvature. (iii) Subsequently, again "fresh" 15 nm thick a-Si films were deposited on the polished front-side surfaces of the O-exposed substrates. (iv) Finally, the specimens as obtained after step (iii) were again exposed to pure oxygen gas at partial pressures of, successively, 1 x 10^{-4} Pa, 1 x 10^{-2} Pa and 1 Pa for t = 1800 s each. Since the backside surfaces of the Si(111) and the Si(100) substrates were already passivated during the first O exposures in step (ii), the difference between the measured substrate-curvature changes in step (ii) and step (iv) equals the substrate-backside effect.

Appendix 5.C. Oxygen exposure interruptions

In order to demonstrate that the measured film-force change is exclusively associated with the growth of the oxide film, oxygen exposure interruptions were performed not only after the oxide film attained its near-limiting thickness but also at the initial stage of oxide film growth at $\mathrm{p_{O_2}} = 10^{-4}\mathrm{Pa}$ (i.e. directly after the ellipsometric parameter $\delta\Psi$ reached a constant value). As shown in Fig. A5.1 practically no film-force change can be observed during an oxygen exposure interruption of 20 min, and directly after restarting the oxygen exposure the film-force evolution continuous as if no oxygen exposure interruption had occurred.

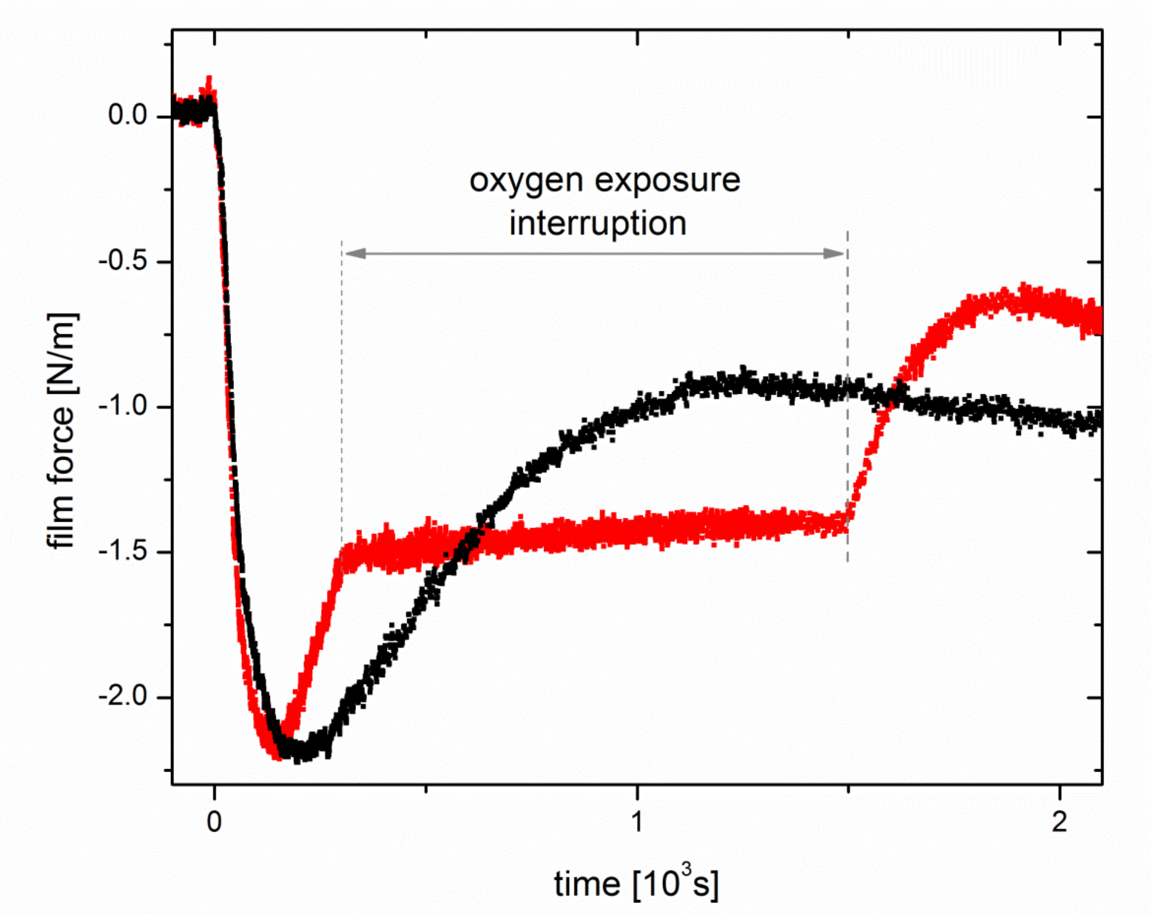

Fig. A5.1. Change of the film force during oxidation of two Al(111) films at $p_{O_2} = 10^{-4}$Pa with (red) and without (black) an oxygen exposure interruption. During the oxygen exposure interruption of 20 min no film-force change is observed, and directly after restarting the oxygen exposure the film-force evolution continuous as if no oxygen exposure interruption had occurred.

References

[1] V. V. Afanas'ev and A. Stesmans, J. Appl. Phys. **102,** 081301 (2007).

[2] U. Diebold, S.-C. Li, and M. Schmid, Annu. Rev. Phys. Chem **61,** 129 (2010).

[3] J. Ma, Y. He, D. Wang, and W. Gao, Mater. Lett. **58,** 807 (2004).

[4] N. Cabrera and N. F. Mott, Rep. Prog. Phys. **12,** 163 (1949).

[5] A. T. Fromhold, Jr. and E. L. Cook, Phys. Rev. **158,** 600 (1967).

[6] F. Reichel, L. P. H. Jeurgens, and E. J. Mittemeijer, Acta Mater. **56,** 2897 (2008).

[7] N. Cai, G. Zhou, K. Müller, and D. E. Starr, Phys. Rev. Lett. **107,** 035502 (2011).

[8] F. Reichel, L. P. H. Jeurgens, and E. J. Mittemeijer, Acta Mater. **56,** 659 (2008).

[9] Z. W. Lars P. H. Jeurgens, Eric J. Mittemeijer, Inter. J. Mater. Res. **100,** 1281 (2009).

[10] N. Cai, G. Zhou, K. Müller, and D. E. Starr, J. Phys. Chem. C **117,** 172 (2012).

[11] F. P. F. A.G. Revesz, Oxid. Metals **15,** 297 (1981).

[12] L. P. H. Jeurgens, F. Reichel, S. Frank, G. Richter, and E. J. Mittemeijer, Surf. Inter. Anal. **40,** 259 (2008).

[13] F. N. W. Rhines, J.S., Metall. Trans. **1,** 1701 (1970).

[14] D. R. Clarke, Acta Mater. **51,** 1393 (2003).

[15] X. Dong, X. Feng, and K.-C. Hwang, J. Appl. Phys. **112,** 023502 (2012).

[16] A. W. Fortuin, P. F. A. Alkemade, A. H. Verbruggen, A. J. Steinfort, H. Zandbergen, and S. Radelaar, Surf. Sci. **366,** 285 (1996).

[17] K. H. Westmacott, S. Hinderberger, and U. Dahmen, Phil. Mag. A **81,** 1547 (2001).

[18] E. Chason and B. W. Sheldon, Surf. Eng. **19,** 387 (2003).

[19] D. Flototto, Z. M. Wang, L. P. H. Jeurgens, E. Bischoff, and E. J. Mittemeijer, J. Appl. Phys. **112,** 043503 (2012).

[20] S. Suresh, L.B. Freund, *Thin Film Materials* (Cambridge University Press, Cambridge, England, 2003).

[21] F. Reichel, L. P. H. Jeurgens, G. Richter, and E. J. Mittemeijer, J. Appl. Phys. **103,** 093515 (2008).

[22] R. M. Azzam, *Ellipsometry and polarized light* (Amsterdam, North-Holland, 1979).

[23] P. Hofmann, W. Wyrobisch, and A. M. Bradshaw, Surf. Sci. **80,** 344 (1979).

[24] I. P. Batra and L. Kleinman, J. Elec. Spec. Rel. Phenom. **33,** 175 (1984).

[25] J. Grimblot and J. M. Eldridge, J. Electrochem. Soc. **129,** 2366 (1982).

[26] L. L. Lauderback and S. A. Larson, Surf. Sci. **234,** 135 (1990).

[27] H. Brune, J. Wintterlin, J. Trost, G. Ertl, J. Wiechers, and R. J. Behm, J. Chem. Phys. **99,** 2128 (1993).

[28] F. Soria, V. Martínez, M. C. Muñoz, and J. L. Sacedón, Phys. Rev. B **24,** 6926 (1981).

[29] M. L. den Boer, T. L. Einstein, W. T. Elam, R. L. Park, L. D. Roelofs, and G. E. Laramore, Phys. Rev. Lett. **44,** 496 (1980).

[30] W. Jun, Y. L. Fan, D. W. Gong, S. G. Shen, and X. Q. Fan, Modell. Simu. Mater. Sci. Eng. **7,** 189 (1999).

[31] R. J. Needs, Phys. Rev. Lett. **58,** 53 (1987).

[32] P. J. Feibelman, Phys. Rev. B **56,** 2175 (1997).

[33] W. J. Bernard and J. W. Cook, J. Electrochem. Soc. **106,** 643 (1959).

[34] J. Burke and Ramachan.Tr, Metall. Trans. **3,** 147 (1972).

[35] G. Gutiérrez and B. Johansson, Phys. Rev. B **65,** 104202 (2002).

[36] K. G. Lynn, Phys. Rev. Lett. **44,** 1330 (1980).

[37] C. Lanthony, J. M. Ducere, M. D. Rouhani, A. Hemeryck, A. Esteve, and C. Rossi, J. Chem. Phys. **137,** 094707 (2012).

Chapter 6

Summary

Functionalization of thin-film systems on the basis of their mechanical, electrical, optical and magnetic properties requires precise control of the intrinsic film stresses that develop during the growth process. Although the intrinsic stress evolution during thin film growth has been extensively studied for a huge diversity of different materials, deposition techniques and deposition conditions, the technological potential to optimize and control the properties of thin film systems by tailoring their stress state *and* their microstructure is still limited due to the lack of fundamental and comprehensive understanding of the stress-inducing mechanisms and their complex correlation with atomic scale processes during thin film growth.

The present PhD thesis addresses the correlation of intrinsic stress generation with the developing microstructure and atomic scale processes, such as diffusion (Chapter 2), adsorption (Chapter 4) and reactions (Chapter 5) during growth of (ultra)thin films. Furthermore, a hitherto unrecognised intrinsic stress generating mechanism, induced by quantum confinement of free electrons in ultrathin metal films, has been discovered (Chapter 3). To this end, the intrinsic stress evolutions and microstructural developments during the growth of metal-, semiconductor- and oxide-based thin films have been studied by a combinatorial experimental approach using real time in-situ substrate curvature measurements and a broad range of microstructure and surface-analytical techniques (Chapter 1.5).

In Chapter 2 of this PhD thesis the effect of the adatom surface diffusivity on the evolution of the microstructure and the intrinsic stress of thin metal films was investigated for the case of growth of polycrystalline Ag films on amorphous SiO_2 (a-SiO_2) and amorphous Ge (a-Ge) substrates, with high and low Ag adatom surface diffusivity, respectively. As evidenced by angle-resolved X-ray photoelectron spectroscopy (AR-XPS), Ge continuously segregates at the surface of the growing film and thus suppresses the surface diffusivity of the deposited Ag adatoms on the a-Ge substrate also *after* coalescence of Ag islands and subsequent thickening of the laterally closed Ag film. The abatement of the Ag adatoms surface diffusivity by (segregated) Ge leads to the development of a fine, equiaxed, texture less microstructure for Ag film growth on a-Ge substrates, which is in striking contrast to the development of a columnar, surface energy minimizing {111} fiber textured microstructure for Ag film growth on a-SiO_2 substrates. Nevertheless, the real-time in-situ stress measurements revealed a compressive→tensile→ compressive stress evolution for the developing Ag films on both types of substrates, however on different time scales and with stress-component values of largely different magnitudes. On the basis of ex-situ transmission electron microscopy (TEM), ex-situ X-ray diffraction (XRD) and real-time in-situ stress measurements an assessment could be made of the role of adatom surface diffusivity on the microstructural development and the intrinsic stress evolution during film growth: The microstructural development of polycrystalline metallic thin films is predominated by the *surface* diffusivity of the adatoms, and the intrinsic stress evolution is largely controlled by the developing microstructure and the grain-boundary diffusivity of atoms.

In Chapter 3 it is revealed that the in-plane film stress *oscillates* with increasing film thickness at the initial stage of epitaxial single-crystalline Al(111) film growth on a Si(111)-$\sqrt{3} \times \sqrt{3}$-Al surface, with a periodicity of two times the Fermi wavelength of bulk Al and a stress amplitude as large as 100 MPa (see Fig. 6.1). Such macroscopic stress oscillations are shown to be caused by a hitherto unrecognised stress generating mechanism resulting from the quantum confinement of free electrons in the ultrathin metal film: A freestanding film would energetically prefer specific thicknesses and lateral dimensions as a result of the optimal, net effect of quantum confinement of the electrons and the associated elastic deformation (straining). Because the film is attached to the (rigid) substrate, the (oscillating) preferred lateral dimensions cannot be realized and consequently an oscillating component of stress is induced in the plane of the film. The amplitude, period and phase of the observed stress oscillations are consistent with predictions based on the free electron model and continuum elasticity. The here disclosed direct link between quantum confinement and macroscopic film stress is also applicable to other metal thin films and thus can play a crucial role for the design of novel-concept functional devices which, in particular, rely on ultrathin heterostructures.

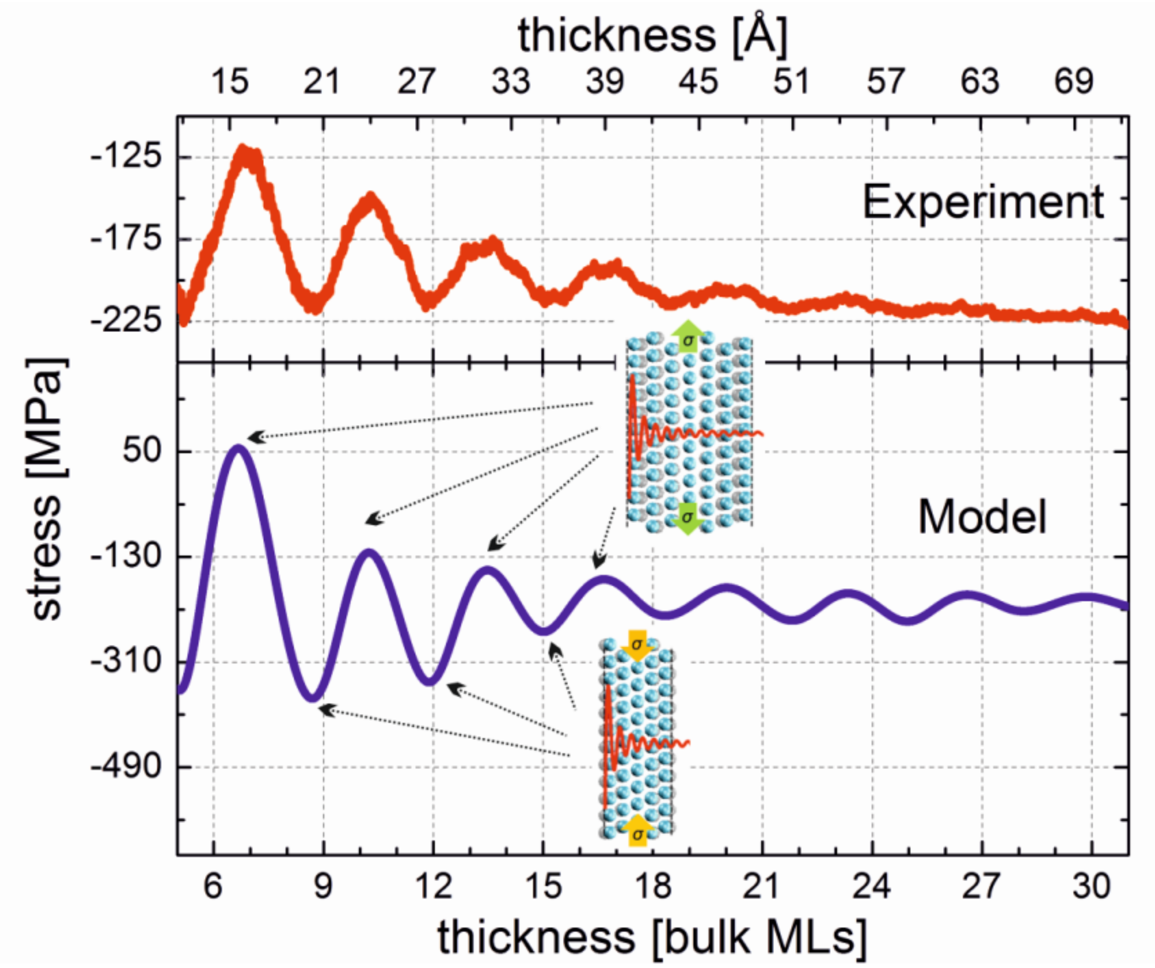

Fig. 6.1. The experimentally observed oscillating in-plane film stress (red) and the model predictions based on free-electron model and continuum elasticity (blue). Due to the oscillating excess free electron energy and the attempt of thin film systems to minimize its energy, the Al-film is forced to contract/expand perpendicular to its surface (see insets). However, the lateral film dimensions are constrained by the rigid substrate and thus the contraction/expansion of the film thickness is accompanied with the development of a compressive or tensile in-plane film stress.

In Chapter 4 of this work, it is revealed that oxygen exposure of clean Si(111)-7x7, Si(100)-2x1 and a-Si surfaces results in compressive adsorption-induced surface stress changes for all three surfaces due to the incorporation of O atoms into Si backbonds. The measured surface-stress change decreases with decreasing atomic packing density of the clean Si surfaces (i.e. from Si(111), a-Si to Si(100)), in correspondence with the less-densily packed Si surface regions containing more free volume for the accomodation of adsorbed O atoms. Indispensable for the success of this work (see also Chapter 5) was the setup of a generally applicable, dedicated set of experiments to deduce and correct the surface stress change owing to oxygen reaction(s) at the (poorly-defined) rough back face of the specimen only. The oxygen-adsorption induced surface-stress change at the rough back face surfaces of a Si specimen is of the same order of magnitude as that at the (well-defined) front side surfaces and thus the back face effect cannot simply be neglected.

In Chapter 5 it is demonstrated for the first time that pronounced intrinsic stresses can be generated in ultrathin *amorphous* Al_2O_3 films formed by thermal oxidation of bare Al surfaces at low temperatures (see Fig. 6.2). The magnitude of the growth stress strongly depends on the Al surface orientation: Oxide films formed on Al(100) are stress free, whereas oxide films formed on Al(111) exhibit a thickness averaged in-plane tensile film stress as large as 1.9 GPa. The striking dependence of the stress evolution on the Al surface orientation at the very beginning of oxygen exposure is a direct consequence of the different initial oxygen-adsorbate structures at the Al surfaces inducing distinctly different adsorption in-

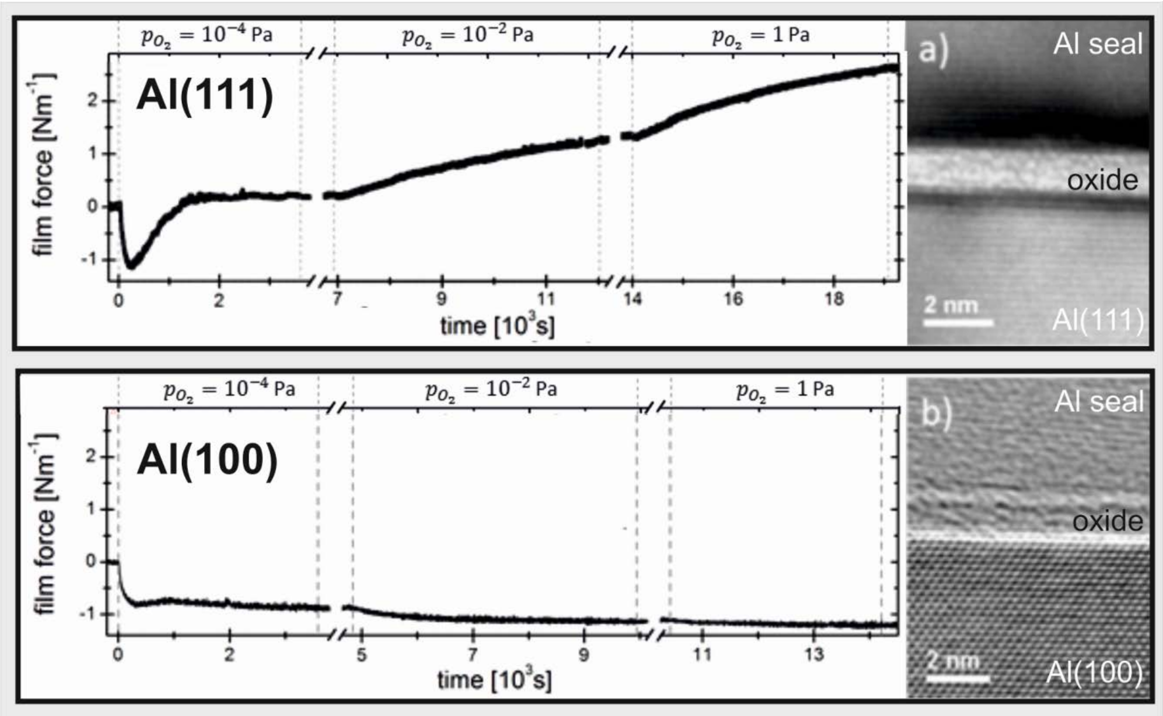

Fig. 6.2. The evolution of film force upon growth of ultrathin *amorphous* Al_2O_3 films on Al(111) and Al(100) film surfaces during successive oxygen gas exposures at $p_{O_2} = 1 \text{ x } 10^{-4}$ Pa, $p_{O_2} = 1 \text{ x } 10^{-2}$ Pa and $p_{O_2} = 1$ Pa at 300 K. Cross-sectional HRTEM micrographs of the amorphous Al_2O_3 oxide film formed on Al(111) and the Al(100) film surface.

duced changes of surface stress. In contrast, the observed striking dependence of the stress evolution on the Al surface orientation during continued oxide-film growth is the result of competing processes of free volume generation and structural relaxation originating from the different microstructural developments for amorphous oxide film growth on Al(111) and Al(100). The here disclosed intrinsic growth stresses in even amorphous, ultrathin (native) oxide films can strongly affect the functional (mechanical, chemical, electronic and optical) properties of ultra-thin (native) oxide films on metal and metallic alloy surfaces.

On the basis of the experimental findings of the present PhD thesis, as obtained by combining real-time in-situ stress measurements with AR-XPS, XRD, STM, HRTEM and RISE, it can be concluded that, in particular for the growth of ultrathin films, the consideration of atomic scale processes, such as diffusion, adsorption and reactions, is of essential importance for a fundamental and comprehensive understanding of the acting intrinsic stress generating mechanisms. Even the quantum size effect, resulting from the special confinement of free electrons in ultrathin films, can induce a significant amount of growth stresses and thus might open up new possibilities for a controlled tailoring of the functional properties of thin film systems on the basis of their intrinsic stress state.

Chapter 7

Zusammenfassung

Die Funktionalisierung von Dünnschichtsystemen auf Basis ihrer mechanischen, elektrischen, optischen und magnetischen Eigenschaften erfordert eine präzise Kontrolle der intrinsischen Spannungen, die während des Filmwachstums entstehen. Obwohl die intrinsische Spannungsentwicklung für eine große Vielfalt an Materialien, Abscheidetechniken und Wachstumsbedingungen intensiv untersucht wurde, ist das technologische Potenzial, die Eigenschaften von Dünnschichtsystemen durch exaktes Einstellen ihres Spannungszustandes und ihrer Mikrostruktur zu optimieren, noch immer aufgrund eines fehlenden grundlegenden Verständnisses der spannungsinduzierenden Mechanismen und ihrer komplexen Wechselbeziehung mit atomaren Prozessen während des Filmwachstums begrenzt.

Die vorliegende Doktorarbeit befasst sich mit dem Zusammenhang zwischen intrinsischen Spannungen und der sich entwickelnden Mikrostruktur sowie den atomaren Prozessen während des Wachstums von (ultra)dünnen Schichten wie Diffusion (Kapitel 2), Absorption (Kapitel 4) und Reaktionen (Kapitel 5). Des Weiteren wurde ein bisher noch unbekannter direkter Zusammenhang zwischen dem Quanten Confinement freier Elektronen in ultradünnen Metallschichten und makroskopischen mechanischen Spannungen entdeckt (Kapitel 3). Zu diesem Zweck wurde die Entwicklung der intrinsischen Spannung und der Mikrostruktur während des Wachstums von Metall-, Halbleiter- und oxidbasierenden Dünnschichten durch eine Kombination von unterschiedlichen experimentellen Techniken, wie Echtzeit in-situ Substratkrümmungs-Messungen und einer großen Bandbreite von mikrostruktur- und oberflächenanalytischen Techniken, untersucht (Kapitel 1.5).

In Kapitel 2 der vorliegenden Doktorarbeit wurde der Einfluss der Adatom-Oberflächendiffusivität auf die Entwicklung der Mikrostruktur und der intrinsischen Spannung von dünnen Metallschichten am Beispiel des polykristallinen Ag Filmwachstums auf amorphen SiO_2 (a-SiO_2) und amorphen Ge (a-Ge) Substraten, mit hoher bzw. niedriger Ag Adatom-Oberflächendiffusivität, untersucht. Wie mittels winkel-aufgelöster Photoelektronen-Spektroskopie (AR-XPS) nachgewiesen werden konnte, segregiert kontinuierlich Ge zur Oberfläche des wachsenden Films. Dies reduziert die Oberflächendiffusivität der abgeschiedenen Ag Adatome, im Fall der Filmabscheidung auf dem a-Ge Substrat, auch nach dem Zusammenwachsen der Ag Inseln und dem sich anschließenden Wachstum des lateral geschlossenen Ag Films. Die Verringerung der Ag Oberflächendiffusion durch (segregierendes) Ge führt zur Ausbildung einer feinen, gleichachsigen, untexturierten Mikrostruktur für das Ag Filmwachstum auf dem a-Ge Substrat, welche im starken Gegensatz zur Bildung einer kolumnaren, oberflächenenergieminimierenden {111}-faser texturierten Mikrostruktur für das Ag Filmwachstum auf dem a-SiO_2 Substrat steht. Trotz dieser ausgeprägten mikrostrukturellen Unterschiede wurde während des Ag Schichtwachstums auf beiden Substraten mittels Echtzeit in-situ Spannungsmessungen eine Druck→Zug→Druck Spannungsentwicklung gemessen. Die Spezifischen Spannungen traten jedoch in deutlich unterschiedlicher Ausprägung und in verschiedenen Zeitabschnitten des Filmwachstums auf. Auf Basis der ex-situ Transmissions-Elektronenmikroskopie- (TEM), der ex-situ Röntgendiffraktometrie (XRD) und der Echtzeit in-situ Spannungsmessungen konnte eine Aussage über den Einfluss der Adatom-Oberflächendiffusivität auf die Bildung der Mikrostruktur und die Entwicklung der intrinsischen Spannung während des Filmwachstums getroffen werden: Die Mikrostrukturbildung von polykristallinen metallischen Dünnschichten wird maßgeblich durch die Oberflächendiffusivität bestimmt, und die intrinsische Spannungsentwicklung wird weitestgehend von der Mikrostrukturbildung und der Korngrenzendiffusivität der Atome kontrolliert.

In Kapitel 3 wurde gezeigt, dass während des Anfangsstadiums des epitaktischen einkristallinen Al(111) Schichtwachstums auf einer Si(111)-$\sqrt{3} \times \sqrt{3}$-Al Oberfläche die Spannung in der Ebene des Films mit zunehmender Schichtdicke mit einer Periodizität der doppelten Al Bulk-Fermi-Wellenlänge und einer Spannungsamplitude von bis zu 100 MPa oszilliert (siehe Fig. 6.1). Es wurde gezeigt, dass diese makroskopischen Spannungsoszillationen von einem bisher unbekannten spannungsgenerierenden Mechanismus hervorgerufen werden, der vom Quanten Confinement freier Elektronen in dem ultradünnen Metallfilm rührt: Ein freistehender Film würde aufgrund der optimalen Energiebilanz, resultierend aus

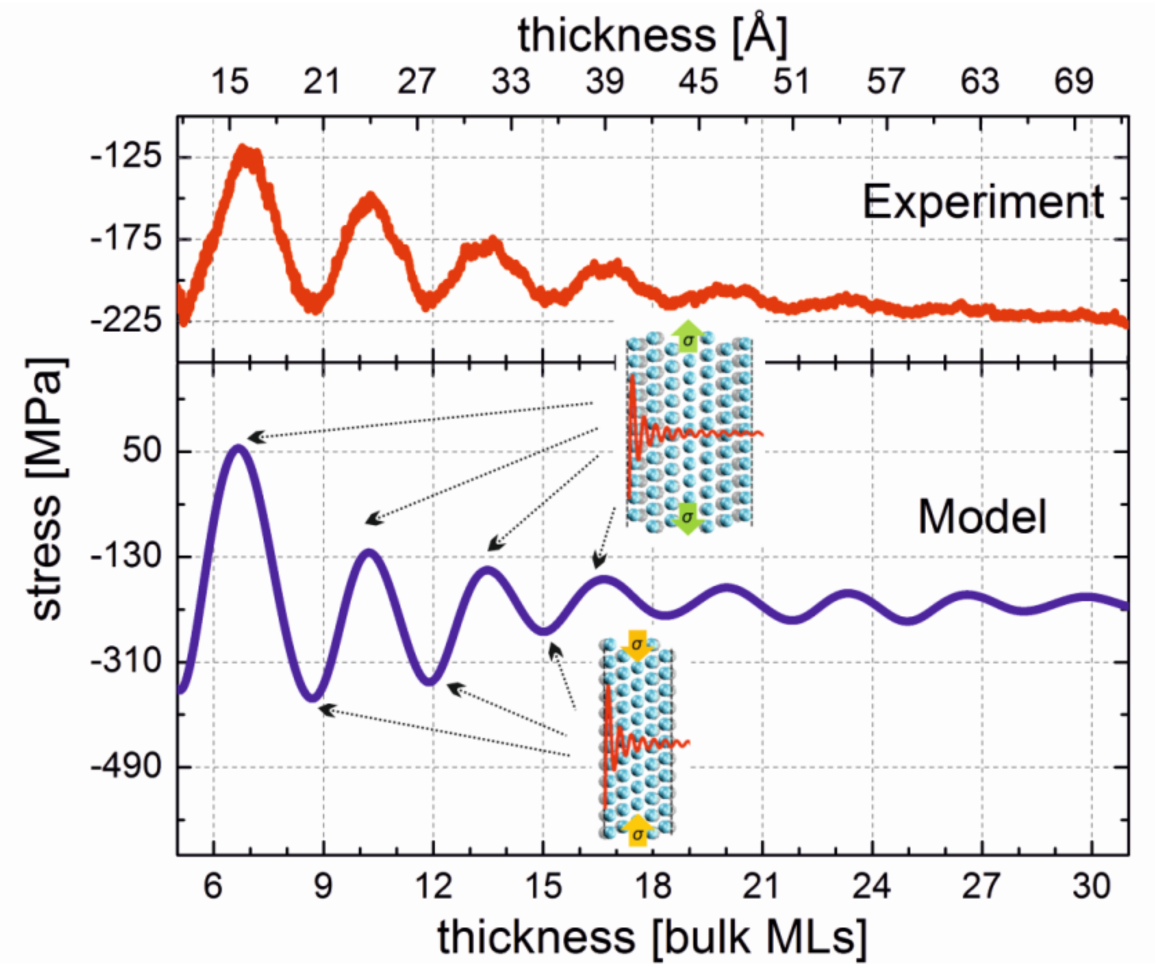

Fig. 6.1. Die experimentell beobachtete oszillierende Spannung in der Ebene der dünnen Al Schicht (rot) und die Modellvorhersage, basierend auf Kontinuumsmechanik dem Freien-Elektronen-Modell und (blau). Aufgrund der oszillierenden Exzess Freien Elektronen Energie (rote Kurve in der Skizze) und dem Bestreben des Dünnschichtsystems, seine Energie zu minimieren, ist der Al Film gezwungen, sich senkrecht zu seiner Oberfläche zusammenzuziehen/auszudehnen. Da jedoch die lateralen Schichtdimensionen durch das starre Substrat eingeschränkt sind, ist das periodische Zusammenziehen/Ausdehnen der Schichtdicke mit der Entwicklung einer Druck-/Zugspannung in der Filmebene verbunden.

Quanten Confinement Effekt und der damit verbundenen elastischen Verformung (Dehnung), sowohl spezifische Dicken als auch spezifische laterale Dimensionen annehmen. Da jedoch der Film fest mit dem (steifen) Substrat verbunden ist, können die (oszillierenden) bevorzugten lateralen Dimensionen nicht realisiert werden und in Folge dessen wird eine oszillierende Spannungskomponente in der Schicht, parallel zu dessen Oberfläche, induziert. Die Amplitude, Periode und Phase der beobachteten Spannungsoszillationen stimmen mit Vorhersagen, basierend auf Kontinuumsmechanik und dem Freien-Elektronen-Modell, überein. Der hier offengelegte direkte Zusammenhang von Quanten Confinement und makroskopischer Filmspannung kann auch auf andere dünne Metallschichtensysteme übertragen werden und spielt somit eine bedeutende Rolle bei der Entwicklung neuartiger funktionaler Bauelemente, welche im Besonderen auf ultradünnen Heterostrukturen basieren.

In Kapitel 4 dieser Arbeit wurde der Effekt der Sauerstoff Adsorption auf die Oberflächenspannung von reinen Si(111)-7x7, Si(100)-2x1 und amorphen Si (a-Si) Oberflächen bei Raumtemperatur und einem Sauerstoffpartialdruck von $p_{O_2} = 1 \text{ x } 10^{-4}$ Pa mittels Echtzeit in-situ Substratkrümmungs- und AR-XPS Messungen untersucht. Für alle drei Si Oberflächen führt der Einbau von O Atomen in die Si Oberflächen (d.h. zwischen Si Atomen direkt an der Oberfläche und den Si Atomen in der darunterliegenden zweiten Schicht) zu einer adsorptions-induzierten Druck-Oberflächenspannungsänderung. Die gemessene Oberflächenspannungsänderung nimmt mit geringer werdender atomarer Packungsdichte der reinen Si Oberflächen ab (d.h. von Si(111) über a-Si zu Si(100)). Dieses stimmt mit der Tatsache überein, dass eine weniger dichtgepackte Si Oberfläche mehr freies Volumen zur Anpassung von adsorbierten O Atomen aufweist. Unverzichtbar für den Erfolg dieser Studie (siehe auch Kapitel 5) war das Entwerfen eines generell anwendbaren, adäquaten Experimentes, um ausschließlich die Oberflächenspannungsänderung aufgrund der Reaktion von Sauerstoff mit der rauen (wenig definierten) Probenrückseite zu bestimmen und nachfolgende Messungen um diesen Effekt korrigieren zu können. Es konnte gezeigt werden, dass die adsorptions-induzierte Oberflächenspannungsänderungen aufgrund der Reaktion von Sauerstoff mit der rauen Si Probenrückseite und der polierten (wohl-definierten) Si Probenvorderseite von gleicher Größenordnung ist und somit der Rückseiten-Effekt nicht einfach vernachlässigt werden kann.

Im Kapitel 5 wird zum ersten Mal gezeigt, dass während des thermischen Oxidierens von reinen Al Oberflächen bei niedrigen Temperaturen ausgeprägte intrinsische Spannungen in den sich bildenden ultradünnen *amorphen* Al_2O_3 Schichten entstehen können (siehe Fig. 6.2). Das Ausmaß der Wachstumsspannungen hängt hierbei entscheidend von der Al Oberflächenorientierung ab: Die auf Al(100) Oberfläche gebildeten Oxidschichten sind spannungsfrei, während die auf der Al(111) Oberfläche gebildeten

Oxidschichten eine dickengemittelte Zugspannung von bis zu 1.9 GPa parallel zur Oberfläche aufweisen. Die bemerkenswerte Abhängigkeit der Spannungsentwicklung von der Al Oberflächenorientierung während des Anfangsstadiums der Sauerstoff Exposition ist eine unmittelbare Konsequenz der von verschiedener Sauerstoffadsorbat-Strukturen auf den jeweiligen Al Oberflächen hervorgerufenen, stark unterschiedlichen Oberflächenspannungsänderungen. Während des anschließenden Oxidschichtwachstums konkurriert die Bildung von Freiem Volumen mit strukturellen Relaxationsprozessen. Deren unterschiedlich starke Ausprägung, hervorgerufen von verschiedenen Mikrostrukturentwicklungen in den amorphen Oxidschicht auf Al(111) und der Al(100) Oberflächen, führt zu der beobachteten Abhängigkeit der Spannungsentwicklung von der Oberflächenorientierung im späteren Stadium der Oxidation. Die hier aufgedeckten intrinsischen Wachstumsspannungen in sogar *amorphen* ultradünnen (natürlichen)

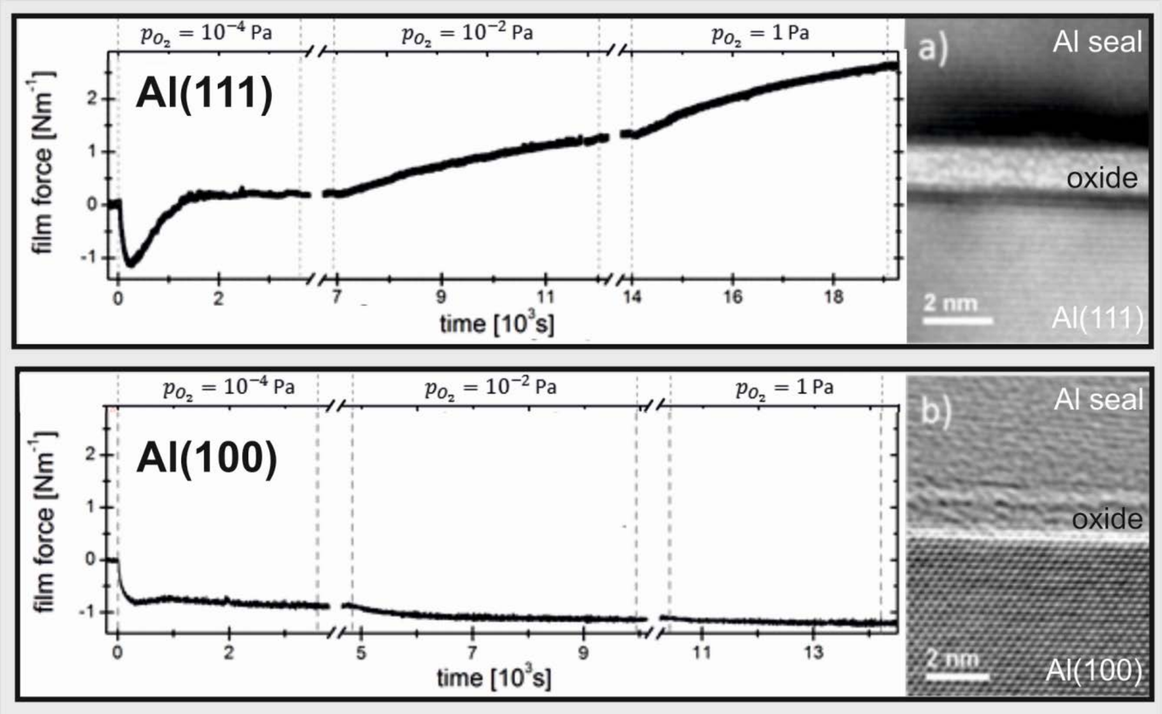

Fig. 6.2. Die Entwicklung der Filmkraft während des Wachstums von ultradünnen Al_2O_3 Schichten auf Al(111) und Al(100) Filmoberflächen bei Raumtemperatur und aufeinander folgenden reinem Sauerstoff Expositionen bei $p_{O_2} = 1 \times 10^{-4}$ Pa, $p_{O_2} = 1 \times 10^{-2}$ Pa und $p_{O_2} = 1$ Pa sowie Querschnitts HRTEM Aufnahmen der auf Al(111) und Al(100) gebildeten amorphen Aluminiumoxid Schichten.

Oxidschichten können stark die funktionalen (mechanischen, chemischen, elektrischen und optischen) Eigenschaften von ultradünnen Oxidschichten auf Metall- sowie Metalllegierungs-Oberflächen beeinflussen.

Zusammenfassend kann auf der Grundlage der Kombination der experimentellen Ergebnisse von Echtzeit in-situ Spannungsmessungen, AR-XPS, XRD, STM, HRTEM und RISE ausgesagt werden, dass für ein grundlegendes Verständnis der Wachstumsspannungen in ultradünnen Schichten atomare Prozesse wie Diffusion, Adsorption und Reaktionen von herausragender Bedeutung sind. Sogar Quanten Confinement Effekte, resultierend aus der räumlichen Einschränkung der freien Elektronen in ultradünnen Schichten, können signifikante Wachstumsspannung erzeugen und somit neue Möglichkeiten eröffnen, die funktionalen Eigenschaften von Dünnschichtsystemen auf Grundlage ihres Spannungszustands maßzuschneidern.

Symbols and abbreviations

MOS	Multi optical stress sensor
AR-XPS	angle-resolved X-ray photoelectron spectroscopy
STM	scanning tunneling microscopy
RISE	real-time in-situ spectroscopic ellipsometry
UHV	ultra-high vacuum
HRTEM	high-resolution transmission electron microscopy
XRD	X-ray diffraction
EAL	effective attenuation length
ML	monolayer
a	amorphous
GB	grain boundary
PLZ	primary zero loss
$\gamma_{s/i}$	surface/interface energy
κ	substrate curvature
τ	film force
M	biaxial modulus
$h_{s/f}$	substrate/film thickness
$\langle\sigma\rangle$	thickness averaged in-plane film stress
f	surface stress
g	interface stress
λ_{eff}	effective attenuation length
Φ	work function
$\Delta(\lambda)$	ellipsometric phase-shift dependent parameter
$\Psi(\lambda)$	ellipsometric amplitude-ratio dependent parameter
T_h	homologous temperature
T_s	substrate temperature
T_m	melting temperature
E .	energy
C_{ijkl}	fourth-rank stiffness tensor
ϵ_{ij}	strain tensor

List of publications

1. D. Flötotto, Z. Wang, L. P. H. Jeurgens, E. Bischoff, and E. J. Mittemeijer, *Effect of adatom surface diffusivity on microstructure and intrinsic stress evolutions during Ag film growth*, J. Appl. Phys. **112**, 043503 (2012) (Chapter 2 of this thesis)
2. D. Flötotto, Z. Wang, L. P. H. Jeurgens, and E. J. Mittemeijer, *Quantum confinement drives macroscopic stress oscillations at the initial stage of thin film growth*, Phys. Rev. Lett. **109**, 045501 (2012) (Chapter 3 of this thesis)
3. D. Flötotto, Z. Wang, L. P. H. Jeurgens, and E. J. Mittemeijer, *Evolution of surface stress during oxygen exposure of clean Si(111), Si(100) and amorphous Si surfaces*, **submitted** to J. Appl. Phys. (Chapter 4 of this thesis)
4. D. Flötotto, Z. Wang, L. P. H. Jeurgens, and E. J. Mittemeijer*, Intrinsic stress evolution during amorphous oxide film growth on Al surfaces*, **submitted** to Phys. Rev. Lett. (Chapter 5 of this thesis)

Danksagung

Die vorliegende Arbeit wurde am Institut für Materialwissenschaft der Universität Stuttgart und am Max-Planck-Institut für Intelligente Systeme (früher Max-Planck-Institut für Metallforschung), Stuttgart, angefertigt. An dieser Stelle möchte ich allen danken, die zum Gelingen dieser Arbeit beigetragen haben.

An erster Stelle möchte ich mich bei Herrn Prof. Dr. Ir. E. J. Mittemeijer, meinem Doktorvater, für die Aufnahme in seine Abteilung, die Möglichkeit zur Durchführung der spannenden Forschungsarbeit und das in mich gesetzte Vertrauen bedanken. Sein außergewöhnliches Engagement und die zahlreichen, intensiven Diskussionen waren von großer Bedeutung für den Erfolg dieser Arbeit. Ich bin sehr dankbar für die Möglichkeiten und die Freiheit in der Forschung die er mir, im Besonderen während der letzten beiden Jahre, geboten hat.

Herr Prof. Dr. S. Schmauder danke ich für die freundliche Übernahme des Mitberichts sowie Prof. Dr. T. Schleid für die Zusage, den Prüfungsvorsitz zu übernehmen.

It is all but impossible to express how grateful I am to my daily supervisors Dr. Zumin Wang and Dr. Lars Jeurgens, who shared their knowledge with me in numerous helpful and inspiring scientific discussions. Their inexhaustible enthusiasm and encouragement have incited me every day and strengthened my eagerness for science.

Herzlich danken möchte ich auch allen Mitarbeitern des Max-Planck-Institutes für Intelligente Systeme, insbesondere den Kollegen der Abteilung Mittemeijer, die mich täglich unterstützt haben und für eine angenehme Arbeitsatmosphäre sorgten. Ganz besonders möchte ich mich hier bei Michaela Wieland, Bernd Siegle und Peter Schützendübe für den experimentellen Beistand und ihre Unterstützung bedanken.

Ich habe keine Worte um meine tiefe Dankbarkeit gegenüber meinen Eltern und meiner Familie auszudrücken, die mich immer unterstützt und so oft aufgemuntert hat. Unendlich vielen Dank Dorothee, Hannes und Charlotte!

Curriculum Vitae

Persönliche Daten

Name	David Flötotto (geb. Regniet)
geboren am	03.10.1983 in Münster
Staatsangehörigkeit	deutsch

Schulbildung

1990 – 1994	Grundschule, Arnsberg
1994 – 2003	Mariengymnasium Arnsberg, mit dem Abschluss der allgemeinen Hochschulreife

Hochschulbildung

2004 – 2009	Studium der Werkstoffwissenschaft an der Universität Stuttgart
2009	Diplomarbeit am Institut für Materialwissenschaft der Universität Stuttgart mit dem Thema „Microstructural and residual stress development in thin fims” bei Prof. Dr. Ir. E. J. Mittemeijer

Promotion

2010 - 2013	Max-Planck-Institut für Intelligente Systeme (ehemals Max-Plank-Institut für Metallforschung), Stuttgart und Institut für Materialwissenschaften der Universität Stuttgart Thema: „Mechanisms of intrinsic stress formation in thin film systems“ bei Prof. Dr. Ir. E. J. Mittemeijer

Erklärung

Ich versichere, dass ich die vorliegende Arbeit mit dem Titel „Mechanisms of intrinsic stress formation in thin film systems“ selbständig verfasst und keine anderen als die angegebenen Quellen und Hilfsmittel benutzt habe; aus fremden Quellen entnommene Passagen und Gedanken sind als solche kenntlich gemacht.

(David Flötotto)